

Spectro-polarimetric diagnostics of magneto-convection simulations of the solar photosphere

Dissertation
zur Erlangung des Doktorgrades
der Mathematisch-Naturwissenschaftlichen Fakultäten
der Georg-August-Universität zu Göttingen

vorgelegt von
Sergiy Shelyag
aus Karachevka / die Ukraine

Göttingen 2004

Bibliografische Information Der Deutschen Bibliothek

Die Deutsche Bibliothek verzeichnet diese Publikation in der Deutschen Nationalbibliografie; detaillierte bibliografische Daten sind im Internet über <http://dnb.ddb.de> abrufbar.

D7

Referent: Prof. Dr. F. Kneer

Korreferent: Prof. Dr. S.K. Solanki

Tag der mündlichen Prüfung: 14.7.2004

Copyright © Copernicus GmbH 2004

ISBN 3-936586-28-4

Copernicus GmbH, Katlenburg-Lindau

Druck: Schaltungsdienst Lange, Berlin

Printed in Germany

Contents

Summary	5
1 Introduction	7
2 MHD model	11
2.1 MHD equations	11
2.2 Equation of state	13
2.3 The MURaM code	16
2.4 Radiative transport in the MURaM code	20
2.5 The results of radiative MHD simulations	21
3 Radiative transfer and line synthesis	27
3.1 Zeeman effect	27
3.2 Stokes parameters	28
3.3 Basics of radiative transfer and line synthesis	29
3.4 Atomic lines	32
3.5 Molecular lines	33
3.6 Spectral line calculations	34
4 Fe I lines diagnostics	39
4.1 Selected lines of Fe I	39
4.2 Diagnostics of simulation results	40
4.2.1 General properties of the simulation results	40
4.2.2 Two-dimensional cuts through the magnetic features	45
4.2.3 Statistical comparison of the simulated profiles with the atmospheric parameters	51
4.3 Comparison with observational data	57
4.4 Conclusions	59
5 G Band simulations	69
5.1 G Band simulations	69
5.2 Why are magnetic bright points bright?	71
5.3 Polarimetry in G Band	74
5.4 Comparison with observational data	76
5.5 Conclusions	78

A The G-Band lines table	85
A.1 CH lines of G Band	85
A.2 General atomic parameters of the elements involved in the G-Band calculations	91
A.3 Atomic lines of G Band	92
Outlook	95
Bibliography	95
Acknowledgements	103
Lebenslauf	105

Summary

In this thesis, spectro-polarimetric diagnostics of three-dimensional MHD simulations has been carried out in order to study the interaction between convective flows and magnetic fields in the solar photosphere by comparing the simulation results with observational data. The projects carried out and the most important results are:

- A realistic equation of state, which includes partial ionization effects, has been incorporated into the MuRAM¹ MHD code for realistic treatment of the convective energy transport in the upper convection zone of the Sun.
- A parallelized computer code for the spectro-polarimetric diagnostics of the simulations (full Stokes vector) has been developed. The code uses the STOPRO² line synthesis program.
- Simulation snapshots representing a “quiet” solar region with 10 G average magnetic field and an active (“plage”) region with 200 G average magnetic field have been analyzed in detail by radiative diagnostics of two pairs of visible and infrared Fe I lines as well as in the “G Band” dominated by lines from the CH molecule.
- The connection between the magnetic and thermodynamic quantities in the simulations and the results of the diagnostics using Fe I lines has been shown. The analysis of the simulated polarimetric data contributes to improving the observational diagnostics of the magnetic and velocity fields. The origin of the area and amplitude asymmetries of the Stokes-*V* profiles in regions with velocity and magnetic field gradients has been clarified. Some comparison of the simulated profiles with observations is presented. The average profiles emerging from the simulated atmosphere are shown to be well agree with the spectral atlas data.
- The physical origin of the so-called “G-band bright points” is revealed. It is shown that the G-band brightenings of small magnetic flux concentrations in the solar photosphere are caused by the lateral heating and partial evacuation of the magnetic structures. The simulated G-band images are statistically compared with observations. The values of observed G-band contrast and the G-band brightness distribution functions are quantitatively reproduced by the simulations after taking into account the degradation of the observed images by the Earth’s atmosphere and finite telescope resolution.

¹Max-Planck-Institut für Aeronomie and University of Chicago Radiative MHD code (Vögler et al. 2003)

²STOkes PROfiles routine (Solanki 1987)

1 Introduction

All astronomical objects except those in our planetary system are much too far away to be studied in situ. In any case, the physical conditions of the Sun and other stars exclude such an approach. Therefore, radiation is by far the most important source of physical information about astronomical objects.

Solar physics takes a special place in stellar astrophysics. Owing to the proximity of the Sun (150 millions km) to the Earth we can resolve various surface phenomena on a wide range of scales, from meridional circulation, differential rotation, limb darkening, which scales are comparable with the size of the Sun, down to small-scale magnetic flux concentrations, which have the size of ~ 100 km. The magnetic flux concentrations are the smallest surface features which can be resolved by the observational instruments, available at the present time.

The radiation coming from the Sun provides only indirect evidence for the physical processes in the solar interior, because the solar plasma becomes opaque for optical wavelengths at temperature above ~ 6500 K.

Nevertheless, many observational effects in the photosphere originate from deeper layers of the Sun, from its convection zone. The convection zone of the Sun is situated above the radiative zone and covers the range of 0.7-1 solar radii, according to helioseismological measurements (Basu and Antia 1997). The granulation, which was discovered by Herschel (1801) and can be observed even by small (≈ 20 cm) telescopes, shows the convective cells near the solar surface. Continuous observations of the granulation show the overshoot of the convection motions into the stably stratified photosphere. Convection motions transfer the energy from the hot bottom to the cooler top of the convection zone.

The Sun is a magnetically active star. This became clear through the observations of sunspots made by George Ellery Hale (1908), who measured the magnetic splitting of spectral lines. The interaction between convective motion and magnetic field in the upper layers of the convection zone and the photosphere, so-called solar magneto-convection, results in the formation of small-scale concentrations of magnetic flux, which plays an important role in the heating of the upper layers of the solar atmosphere and for the variability of total and spectral irradiance.

In the studies of small-scale magnetic fields on the Sun one can distinguish two different approaches. One approach is based on high resolution spectro-polarimetric observations.

The existence of the small-scale magnetic fields was proven by high-resolution polarimetric observations of Sheeley (1967). These magnetic fields were discovered by the analysis of strongly weakened and broadened spectral lines. The magnetic field strengths are shown to be of the kilogauss order by Stenflo (1973), Wiehr (1978).

The observations, which were carried out with a number of FeI lines, showed their

usefulness for studies of active regions on the Sun, spatial correspondence of the observed magnetic fields to the active regions and the dynamical structure of the magnetic fields on the Sun (Kneer and Stolpe (1996), Kneer et al. (1996), Solanki (1993)).

The observations of Rüedi et al. (1992) have shown that the Fe I infrared lines (1564.8 nm) can be used as a good diagnostic tool for magnetic field observations owing to their high magnetic sensitivity.

The high resolution (0.4-0.5 arcsec) observations of small-scale magnetic elements in quiet regions and in active regions with pores and abnormal granulation, carried out by Koschinsky et al. (2001) using the Fabry-Perot Interferometer in the Vacuum Tower Telescope (Tenerife, Spain), showed that the magnetic flux occurs in both bright intergranular bright points and in dark intergranular lanes.

Using the technique of two-dimensional spectroscopy, the granular dynamics of the Sun was studied by Hirzberger and Kneer (2000). The images with the resolution of $0''.4-0''.5$, obtained by speckle reconstruction methods, were used to study the correlation between velocity field and intensity for individual granules.

The recent observations of Sánchez Almeida et al. (2003), which are the first simultaneous observations in both infrared and visible FeI lines (630.15 nm, 630.25 nm, 1564.8 nm and 1565.2 nm), were carried out using highly sensitive polarimeters operated in two different telescopes (Vacuum Tower Telescope and THEMIS at the Observatorio del Teide, Tenerife, Spain). The observations have shown the presence of kilogauss magnetic fields, traced by visible lines, coexisting with sub-kilogauss magnetic fields, traced by infrared lines. Moreover, a significant amount of measured visible and infrared profiles showed opposite polarities at the same pixels, corresponding to opposite polarities of magnetic field.

Turbulence in the terrestrial atmosphere affects the observations by variation of the index of refraction due to density fluctuations, and thus degrades the observed images. In order to decrease the image degradation, the adaptive optics are used. The images obtained by the latest ground-based telescopes with adaptive optics show very high quality of images. Another way to decrease the influence of the atmosphere is to bring the telescope out of the atmosphere.

While the magnetic field on the larger scales, for example, in sunspots and pores, is relatively easy to observe due to the high negative contrast, long lifetimes and easy resolvability by current telescopes, smaller magnetic features, such as “micropores”, which have a size of $1''-2''$, or subarcsecond-sized magnetic concentrations in the downflow lanes of the photospheric granulation are much more difficult to observe due to their small size and rapid evolution (Berger and Title 2001). Thus, indirect methods are often used to study the dynamics of small-scale magnetic elements of the Sun. The indirect methods use various solar phenomena, which are easier to observe, as “proxies” for magnetic structures on the Sun. For example, the correlation of the solar filigree structure to the magnetic fields was studied by Dunn and Zirker (1973) (and the references therein). It was shown that there is spatial correlation between the presence of magnetic field and filigree, however the magnetic field was found to be much more diffuse.

One of the most promising techniques involves the imaging through broadband filters in molecular bands of the solar spectrum. This technique was pioneered by Sheeley (1971), who used the CN band filter centered at 388.3 nm.

More recently, observations in Fraunhofer’s G Band (a spectral region located in the

wavelength range 429.5-431.5 nm, populated by many spectral lines of the CH molecule), giving high contrast images, were used to trace the small-scale magnetic elements, while the nature and physical underground of small-scale magnetic elements brightening in the G Band was not so clear (Berger and Title 2001). Thus, the observational approach can lead to a variety of different and even contradictory physical interpretations of the observational phenomena.

Another approach is based on the numerical modelling of magneto-convection. The term “magneto-convection” is used to describe the interaction of convective flows with a magnetic field in an electrically-conducting fluid.

The simulations of magneto-convection can be divided into two different branches. One uses simplified physics in order to understand the basic processes of magneto-convection. The first time-dependent numerical simulation of magneto-convection was carried out by Weiss (1966). This purely kinematic model showed concentrating of the magnetic field in the up- and downflow regions on the edges of prescribed convective cells.

Realistic simulations of magneto-convection under solar conditions are used to reveal the physical processes in the solar convection zone and photosphere and to correlate them with the information from observations. These simulations required to include various inputs from basic physics like partial ionization, non-grey radiative transfer and open boundary conditions in order to realistically approximate the Sun and to cover the whole branch of physical processes, which have an influence on the radiation coming out of the Sun. The simulation results can be compared with observations through radiative diagnostics and line synthesis. The comparison of the results of simulations with the observations can provide constraints about the realism of the simulations and thus to understand the nature of magnetoconvective processes in the Sun.

The first realistic 3D magneto-convection simulations were carried out by Nordlund (1984). The code, which was used for this simulation, included non-grey radiative transfer and partial ionization, the anelastic approximation and rather low horizontal resolution of 190 km. The simulations illustrated the strong tendency for the magnetic field to be swept to and concentrated in the intergranular lanes.

The simulations of Stein et al. (2002) are fully compressible 3D simulations of magneto-convection with horizontal resolution of 100 km and include partial ionization equilibrium and non-grey radiative transfer. The results of the simulations are compared with observations from the point of view of granular properties and Stokes profiles of the lines of heavy elements like iron.

The intensive radiative diagnostics of the 2D radiative MHD model was carried out by Grossmann-Doerth et al. (1994) based on 8 atomic lines of iron and carbon. The results of the simulations are compared with the observations in order to get the proper values for the width and initial evacuation of the simulated magnetic flux tube.

Steiner et al. (1998), using the 2D radiative MHD simulations with the resolution better than 100 km, analyzed the observational consequences of shock propagation along the magnetic flux tubes.

The two-dimensional code of Gadun et al. (2001) was used to carry out simulations of magnetic flux sheets with the initial magnetic field of mixed polarities and showed transformation of weak horizontal field into strong vertical field and vice versa. Radiative diagnostics of the model was carried out. Even though a quantitative agreement of the

simulations with observations was not expected, the simulations showed that the averaged Stokes parameters correspond rather well to the ones observed in quiet solar areas (Sheminova 2003).

The computing power available nowadays allows to make 3D radiative MHD simulations, which meet the realism requirements and use a well-resolved grid with the resolution of about 20 km. This work is dedicated to spectro-polarimetric diagnostics of such a realistic 3D radiative magneto-convection simulations of the uppermost layers of the solar convection zone and the photosphere. The main goal of this PhD project was to analyze the results of the simulations produced by a compressible 3D MHD code which includes non-grey radiative transfer and the effects of partial ionization for the 11 most abundant chemical elements. The MuRAM code (Vögler and Schüssler (2003), Vögler (2003), Vögler et al. (2003)), which has been developed by the MHD simulation groups at the Max-Planck Institut für Aeronomie (Katlenburg-Lindau, A. Vögler, S. Shelyag, M. Schüssler) and at the University of Chicago (F. Cattaneo, Th. Emonet, T. Linde), was used to produce simulations. The spectro-polarimetric diagnostics technique, based on the STOPRO code (Berdyugina and Solanki (2002), Berdyugina et al. (2003)), was applied to the simulated atmospheres in order to produce the images which can be directly compared with the observations. The observations which were used for this comparison were produced at Swedish Solar Telescope and Dutch Open Telescope (Tenerife, Spain).

In 2nd Chapter the realistic MHD simulations are described. The technique of radiative diagnostics of MHD models is described in 3rd Chapter. 4th Chapter is dedicated to FeI line diagnostics and comparison with the observations, 5th - to G-band diagnostics and comparison with the observations.

2 MHD model

Under the conditions of the convection zone layers and of the photosphere the plasma (up to the temperature minimum) is well described by the magnetohydrodynamic equations. In first section of this chapter, the system of viscous compressible radiative MHD equations is presented. The equation of state, describing the thermodynamical parameters of partially ionized plasma, is discussed in second section. The MURaM MHD code is described in third section. The frequency-dependent radiative transfer in the model is briefly treated in fourth section. Fifth section presents the results of the MHD simulations which are used for radiative diagnostics.

2.1 MHD equations

The MHD equations are written in Gaussian cgs units. The continuity equation represents mass conservation:

$$\frac{\partial \rho}{\partial t} + \nabla \cdot (\rho \mathbf{v}) = 0. \quad (2.1)$$

Here $\rho = \rho(\mathbf{r}, t)$ is the plasma density, $\mathbf{v} = \mathbf{v}(\mathbf{r}, t)$ is the plasma velocity at the point with coordinates (\mathbf{r}, t) .

The equation of motion is given by

$$\frac{\partial \rho \mathbf{v}}{\partial t} + \nabla \cdot \left[\rho \mathbf{v} \mathbf{v} + \left(p + \frac{|\mathbf{B}|^2}{8\pi} \right) \mathbf{1} - \frac{\mathbf{B}\mathbf{B}}{4\pi} \right] = \rho \mathbf{g} + \nabla \cdot \underline{\underline{\tau}}, \quad (2.2)$$

where p is the gas pressure, \mathbf{g} is the gravitational acceleration, $\mathbf{v}\mathbf{v}$ and $\mathbf{B}\mathbf{B}$ are dyadic products, and $\mathbf{1}$ is the 3×3 unit matrix. The magnetic force is split into the gradient of the magnetic pressure

$$p_{\text{mag}} = \frac{|\mathbf{B}|^2}{8\pi}, \quad (2.3)$$

and the term $-\nabla \cdot (\mathbf{B}\mathbf{B}/4\pi)$ representing a tension force. The last term of Eq. (2.2) is the viscous force. For a compressible gas, the components of the viscous stress tensor $\underline{\underline{\tau}}$ are given by

$$\tau_{ij} = \mu \left(\frac{\partial v_i}{\partial x_j} + \frac{\partial v_j}{\partial x_i} - \frac{2}{3} \delta_{ij} (\nabla \cdot \mathbf{v}) \right), \quad i, j = 1, 2, 3, \quad (2.4)$$

where μ is the dynamic viscosity. The Reynolds number

$$Re = \frac{\rho V^2 / L}{\mu V / L^2} = \frac{VL}{\nu}, \quad (2.5)$$

where V is the typical velocity, L is the typical lengthscale, and

$$\nu = \mu/\rho \quad (2.6)$$

is the kinematical viscosity, represents the order-of-magnitude ratio of the advective to viscous terms in Eq. (2.2).

The induction equation,

$$\frac{\partial \mathbf{B}}{\partial t} = \nabla \times (\mathbf{v} \times \mathbf{B}) - \nabla \times (\eta \times \mathbf{B}), \quad (2.7)$$

describes the time evolution of the magnetic field, \mathbf{B} , for a given velocity field, \mathbf{v} . Here η is the magnetic diffusivity, $\eta = c^2/4\pi\sigma$, where σ is the electrical conductivity. The order-of-magnitude ratio of the first and second terms in the right-hand side of the induction equation

$$\frac{|\nabla \times (\mathbf{v} \times \mathbf{B})|}{|\nabla \times (\eta \times \mathbf{B})|} \approx \frac{VB/L}{\eta B/L^2} = vL/\eta = R_m, \quad (2.8)$$

called magnetic Reynolds number, shows the importance of the inductive effect of the velocity field, described by the first term of the induction equation, in comparison to the diffusion of the magnetic field due to finite conductivity of the plasma, described by the second term.

The energy equation

$$\begin{aligned} \frac{\partial e}{\partial t} + \nabla \cdot \left[\mathbf{v} \left(e + p + \frac{|B|^2}{8\pi} \right) - \frac{1}{4\pi} \mathbf{B}(\mathbf{v} \cdot \mathbf{B}) \right] = \\ = \frac{1}{4\pi} \nabla \cdot (\mathbf{B} \times \eta \nabla \mathbf{B}) + \nabla \cdot (\mathbf{v} \cdot \underline{\underline{T}}) + \nabla \cdot (K \nabla T) + \\ + \rho(\mathbf{g} \cdot \mathbf{v}) + Q_{rad} \end{aligned} \quad (2.9)$$

describes the energy balance for the total energy per unit volume, e , which is the sum of internal, kinetic and magnetic energy densities. Here T is the temperature, and K is the thermal conductivity. Q_{rad} is the radiative source term.

$$Q_{rad} = - \int_{\nu} (\nabla \cdot \mathbf{F}_{\nu}) d\nu, \quad (2.10)$$

where \mathbf{F}_{ν} is the radiative energy flux with $dE_{rad} = i_{\nu}(\boldsymbol{\mu} \cdot d\mathbf{S})d\omega d\nu dt$

$$\mathbf{F}_{\nu} = \int I_{\nu}(\boldsymbol{\mu}) \boldsymbol{\mu} d\omega. \quad (2.11)$$

Here I_{ν} is the specific intensity at frequency ν along the direction $\boldsymbol{\mu}$, vector which results from the solution of the time-independent radiative transfer equation:

$$\boldsymbol{\mu} \cdot \nabla I_{\nu} = \kappa_{\nu} \rho (S_{\nu} - I_{\nu}). \quad (2.12)$$

In this equation, S_{ν} is the source function, which we take to be equal to the Planck function B_{ν} since Local Thermodynamic Equilibrium (LTE) is assumed, and κ_{ν} is the frequency-dependent opacity of the material.

2.2 Equation of state

The simulation domain of the MURaM MHD model covers the uppermost layers of the convection zone and the photosphere. These regions contain the partial ionization region of hydrogen, where it is neither completely neutral nor fully ionized. The internal energy, e_{int} , of an ionized fluid can be represented as a sum of two contributions. The first one is the thermal energy of the gas particles. It increases both with increasing temperature and with increasing ionized fraction of the gas because of the growth of the number of particles per unit volume. The second contribution, the so-called ‘‘latent heat’’, includes all energy associated with ionization and excitation of the atomic components of the gas. Its value in the solar convection zone is dominated by the ionization state of hydrogen. In the ionization zone, it contributes to the total internal energy ~ 5 times as much as the thermal energy (Rast et al. 1993). Thus, the simple thermodynamical relations for an ideal gas do not apply. It has to be taken into account in the models of the solar convection zone in order to realistically describe the energy transport.

To close the system of MHD equations one has to specify the equation of state. Since the MURaM code uses ρ and e_{int} as the basic thermodynamical variables, it is needed to obtain other thermodynamical quantities T and p as functions of ρ and e_{int} :

$$T = T(\rho, e_{\text{int}}), \quad p = p(\rho, e_{\text{int}}). \quad (2.13)$$

The ionization energies for the second ionization of the elements included in the calculation are much higher than the energies of first ionization. Thus, for the temperature regime under consideration only the description of the first ionization state is required. The internal energy in this case can be written as:

$$\epsilon = \frac{3}{2\rho}(n_e + n_a)kT + \frac{1}{\rho} \sum n_i^* \chi_i, \quad (2.14)$$

where ϵ is internal energy per unit mass $\epsilon = e_{\text{int}}/\rho$, $n_a = \sum n_i$ is the total atomic and ionic number density, n_i is the number density of i th type of atoms, n_e is the number density of electrons, n_i^* is the number density of the ions of i th type, χ_i is ionization energy for the i th type of atoms. We define:

$$x_i = \frac{n_i^*}{n_i}, \quad (2.15)$$

the ionization degree of the i th type of atoms, dependent on the temperature, and

$$\nu_i = \frac{n_i}{n_a}, \quad (2.16)$$

the relative abundance of i th type of atoms. Thus the electron density n_e can be written as

$$n_e = n_a \sum x_i \nu_i, \quad (2.17)$$

and the concentration of i th type of atom can be rewritten as

$$n_i = x_i \nu_i n_a. \quad (2.18)$$

We write $n_a = \rho/(\mu_a m_0)$, $\mu_a = (\sum n_i \mu_i)/n_a$ the mean molecular weight (for solar composition, $\mu_a = 1.29$).

Using the relations (2.15), (2.16), (2.17) and (2.18), equation (2.14) can be rewritten in the form:

$$\epsilon = \frac{3}{2} \frac{1}{\mu_a m_0} kT (1 + \sum x_i \nu_i) + \frac{1}{\mu_a m_0} \sum x_i \nu_i \chi_i. \quad (2.19)$$

In order to obtain the gas temperature as a function of the internal energy and the density, we have to solve this equation numerically. For a given value of the internal energy and the density, the numerical scheme searches the value of the temperature and calculates the temperature- and density-dependent ionization degrees, which are the solution of Eq. (2.19) with the required precision, by a bisection method.

The ionization degrees x_i are determined from the Saha equation, describing the ionization equilibrium under the assumption of Local Thermodynamical Equilibrium. Under conditions of solar convection zone, the mean free path (and the thermalization length) of the particles is shorter than the distance over which the temperature of the gas changes markedly. Thus the LTE approximation and thermal ionization equilibrium is assumed and the use of Saha equation is justified (Stix 2002).

The Saha equation for first ionization stage can be written as

$$\frac{n_i^*}{n_i - n_i^*} n_e = \frac{u_{i,1}}{u_{i,0}} \frac{2(2\pi m_e kT)^{3/2}}{h^3} \exp(-\chi_i/kT), \quad (2.20)$$

where m_e is electron mass, h is Planck constant, k is Boltzmann constant, $u_{i,1}$ and $u_{i,0}$ are the partition functions for singly ionized and neutral atom of i -th type, respectively.

Using the definitions given above, one can rewrite Eq. (2.20) in the form

$$\frac{x_i}{1 - x_i} \sum x_j \nu_j = \frac{u_{i,1}}{u_{i,0}} \frac{\mu_a m_0}{\rho} \frac{2(2\pi m_e kT)^{3/2}}{h^3} \exp(-\chi_i/kT). \quad (2.21)$$

Here we have a system of i non-linear equations which are solved numerically by a Newton-Raphson method. The essence of the method is described below.

Suppose we have a vector equation $\mathbf{F}(\mathbf{x}) = \mathbf{0}$. Assume \mathbf{x}_0 as an initial guess for the solution vector. In the neighbourhood of \mathbf{x}_0 , the function \mathbf{F} can be expanded in Taylor series,

$$\mathbf{F}(\mathbf{x}_0 + \delta\mathbf{x}) = \mathbf{F}(\mathbf{x}_0) + \mathbf{J}\delta\mathbf{x} + O(\delta\mathbf{x}^2), \quad (2.22)$$

where \mathbf{J} is the Jacobian matrix with the components $J_{ij} = \partial F_i / \partial x_j$.

Neglecting the terms of order $\delta\mathbf{x}^2$ and higher and assuming $\mathbf{F}(\mathbf{x}_0 + \delta\mathbf{x}) = \mathbf{0}$, we obtain the following iteration scheme, which we will use to solve the system of Saha equations:

$$\delta\mathbf{x} = -\mathbf{J}^{-1} \cdot \mathbf{F}(\mathbf{x}_0), \quad (2.23)$$

$$\mathbf{x}_0 \rightarrow \mathbf{x}_0 + \delta\mathbf{x} \quad (2.24)$$

$$\text{if } \frac{|\delta\mathbf{x}|}{|\mathbf{x}|} > \epsilon \text{ then (2.23),} \quad (2.25)$$

where ϵ is a prescribed relative error of the solution. So, at each iteration one has to solve the linear system of equations (2.23), which defines a tangent line to the curve defined by the non-linear vector equation at point \mathbf{x}_0 , in order to get the corrections $\delta\mathbf{x}$ for initial guess solution \mathbf{x}_0 , and correct them until the required precision of solution ϵ will be reached.

In order to use the scheme, the equations of the system have to be slightly rewritten. The equation

$$\frac{x_i}{1-x_i} \sum x_j \nu_j = \Psi(\rho, T), \quad (2.26)$$

where $\Psi(\rho, T)$ is the right-hand side of the equation (2.21), can be easily transformed into the form of a quadratic equation, assuming $x_i \neq 1$:

$$x_i \sum x_j \nu_j - \Psi(\rho, T)(1-x_i) = 0. \quad (2.27)$$

In order to obtain the vector $\delta\mathbf{x}$, the values of the Jacobian matrix \mathbf{J} have to be calculated. The diagonal elements are written as:

$$\frac{\partial F_i}{\partial x_i} = 2x_i \nu_i + \sum_{j \neq i} x_j \nu_j + \Psi(\rho, T), \quad (2.28)$$

and the non-diagonal elements as:

$$\frac{\partial F_i}{\partial x_j} = x_i \nu_j. \quad (2.29)$$

It is easy to see from Eqs. (2.28) and (2.29) that the diagonal elements of the Jacobian matrix have much larger values than the non-diagonal elements. This makes it possible to use a simple and very fast Gauss-Jordan method without pivoting to solve the system of linear equations (2.23). Furthermore, in the case of very high temperatures one can neglect the non-diagonal elements of Jacobian matrix because of the exponential growth of the diagonal elements with the temperature: the third term in (2.28) grows exponentially with the temperature (cf. 2.21). Thus we simply write $J_{ii} \delta x_i = F_i(x_i)$, which corresponds to a set of independent equations.

Having the ionization degrees x_i for all the atomic species included in the calculation and using the equation (2.19), one can calculate the temperature. The pressure is then given by:

$$p = (n_e + n_a)kT = n_a(1 + \sum x_i \nu_i)kT = \frac{\rho}{\mu_a m_0}(1 + \sum x_i \nu_i)kT. \quad (2.30)$$

The calculations have been done for the eleven most abundant elements in the solar photosphere. The relative abundances and ionization energies for those elements are given in the Tab. 2.1. The dependence of the partition functions on temperature was taken from Irwin (1981). For the temperatures higher than 16000 K the elements are almost fully ionized once and the temperature dependence of the partition functions can be neglected.

The table obtained from the calculation was incorporated as a part of the MHD code. The size of the table is 324 values of the internal energy ($\log \epsilon = 11.4 \div 12.8$) and 1000

Atomic Number	Name	ν_i	χ_i [eV]
1	H	0.934042096	13.600
2	He	0.064619943	24.580
6	C	0.000371849	11.256
7	N	0.000091278	14.529
8	O	0.000759218	13.614
11	Na	0.000001997	5.138
12	Mg	0.000035511	7.644
13	Al	0.000002757	5.984
14	Si	0.000033141	8.149
20	Ca	0.000002140	6.111
26	Fe	0.000039844	7.896

Table 2.1: Relative abundances and ionization energies for the eleven most abundant elements in the solar photosphere.

values of the density ($\log \rho = -9 \div -5$). A non-linear scale for the internal energy was used in order to decrease the size of the table. For given values of the internal energy and density, the values of the temperature and the pressure are obtained by linear interpolation. The calculated dependences of temperature and pressure on density and internal energy are shown in Figs. 2.1 and 2.2.

Our tests of the equation of state were based on the standard VALSP atmosphere and convection zone model (Spruit 1977). We took the internal energy and density from the VALSP model, calculated the pressure and the temperature using our equation of state and compared them with the temperature and the pressure as given by VALSP model. In this way, we were able to check the correctness of our equation of state.

Height profiles of the internal energy of the gas with partial ionization (solid line) and without (ideal gas, dashed line) calculated for the VALSP parameters are shown in the Fig. 2.3. The figure shows large difference in the deep layers of the simulation domain. The difference vanishes in the upper layers of photosphere since the low temperature and density of the gas there leads to a very low ionization degree of hydrogen.

The height profiles of the temperature and the pressure on the internal energy and the density for the VALSP atmosphere are overplotted for comparison in Fig. 2.1 and Fig. 2.2.

The tests show good agreement between the parameters of VALSP atmosphere and the calculated parameters. The results of the tests are shown in Fig. 2.4. The relative difference between VALSP atmosphere and the calculations presented never exceeds 1% in the whole range of values relevant for the simulations. In most cases the differences are much smaller. The difference is largest for $T \geq 1.5 \cdot 10^4$ K, which rises from second ionization of helium, which is not included in our calculations.

2.3 The MURaM code

The MURaM (MPS/University of Chicago Radiative MHD) code has been developed jointly by the MHD simulation groups at the Max-Planck Institut für Sonnensystem-

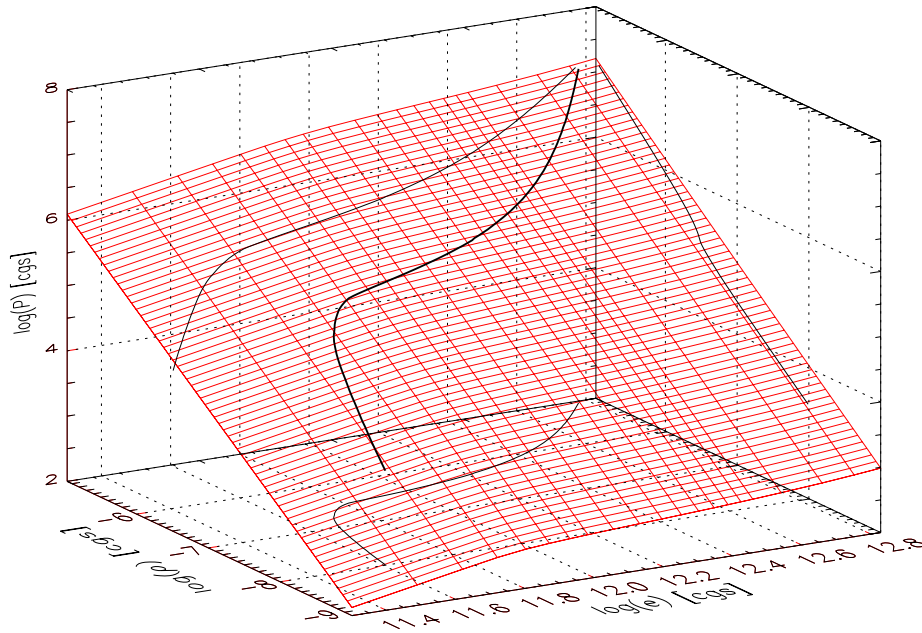


Figure 2.1: The calculated dependence of the pressure on density and internal energy (red surface). The profile corresponding to the VALSP atmosphere is overplotted. The grid for the internal energy is more dense for intermediate values. The curves on the $\log e$ - $\log \rho$, $\log P$ - $\log e$ and $\log \rho$ - $\log P$ planes are projections of the VALSP profile.

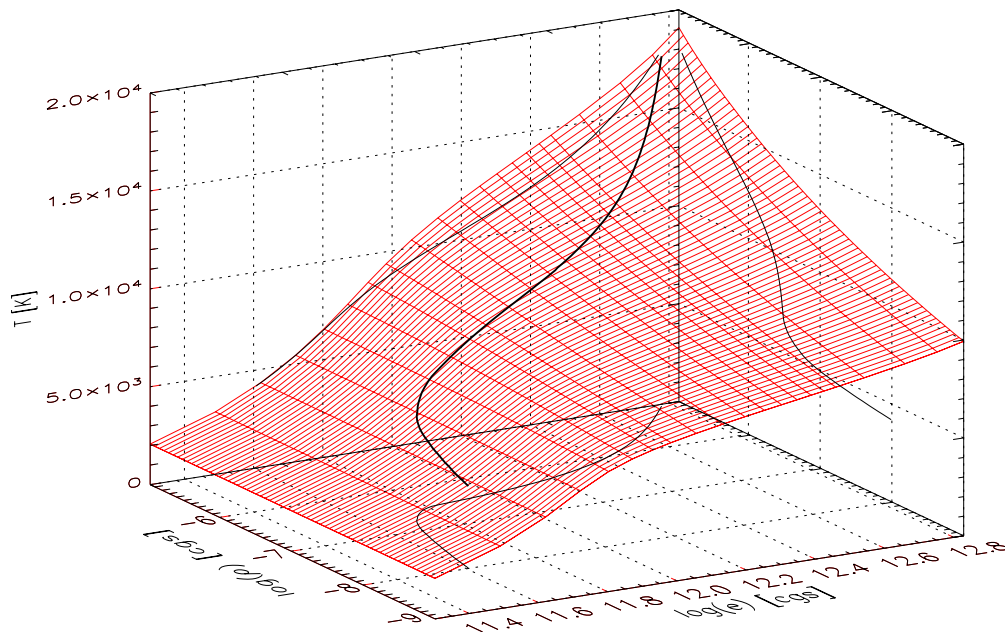


Figure 2.2: The calculated dependence of temperature on density and internal energy. The temperature profile from the VALSP atmosphere is overplotted.

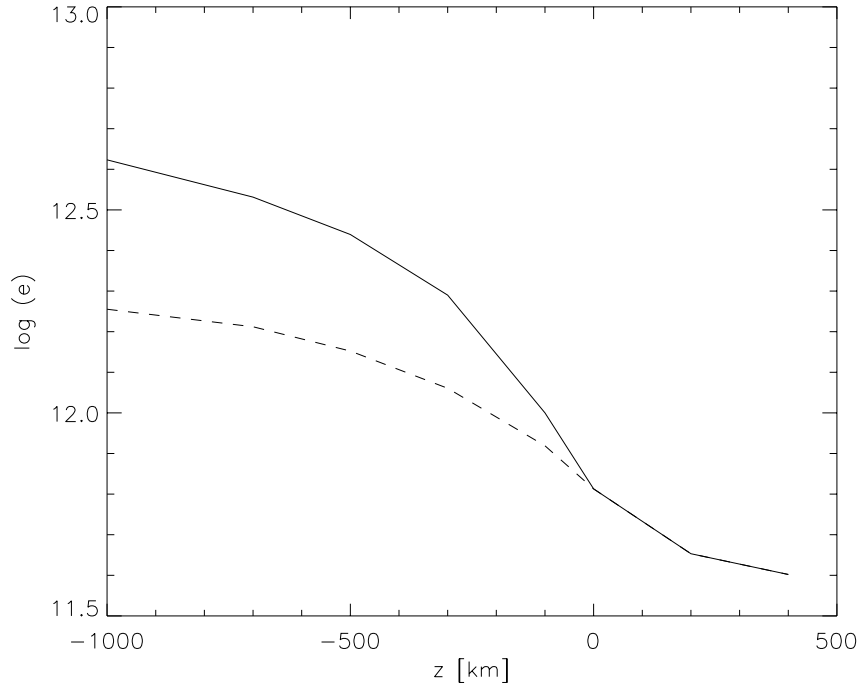


Figure 2.3: Height profiles of the internal energy of the gas including partial ionization (solid line) and the internal energy of an ideal gas (dashed line), calculated for the VALSP model. The difference, which is dramatically large in the deep layers of the simulation domain, almost vanishes in the upper and colder layers. $z = 0$ corresponds to $\tau_{5000} = 1$.

forschung (A. Vögler, S. Shelyag, M. Schüssler) and at the University of Chicago (F. Cattaneo, Th. Emonet, T. Linde). The basis of the code is a MHD solver for equations (2.1), (2.2), (2.10), and (2.7) without the radiative source term, using the equation of state for an ideal gas, and assuming constant diffusion coefficients μ , K and η . The code in this original form did not meet the requirements of realistic solar simulations. In order to realize the conditions of the upper convection zone and photosphere, significant modifications and additions are necessary. These include a non-local and non-grey radiative transfer module, which calculates the radiative source term, additional stabilization of the numerical scheme in order to cover the required density range, an open lower boundary (Vögler 2003), and the realistic equation of state for partial ionization (see Sec. 2.2).

The MURaM code solves the system of MHD equations on a three-dimensional, equidistant cartesian grid. The spatial discretization of the equations is based on a fourth-order centered-difference scheme. The code is parallelized using a domain decomposition scheme. The computational domain is divided into a three-dimensional array of rectangular subdomains, each of which assigned to a separate process on the computer (Vögler 2003). Temporal discretization utilizes a fourth-order Runge-Kutta scheme. The timestep is determined by the Courant-Friedrich-Levi (CFL) criterion, which ensures that flow velocities and wave speeds do not transport information across distances larger than the mesh size in a single timestep.

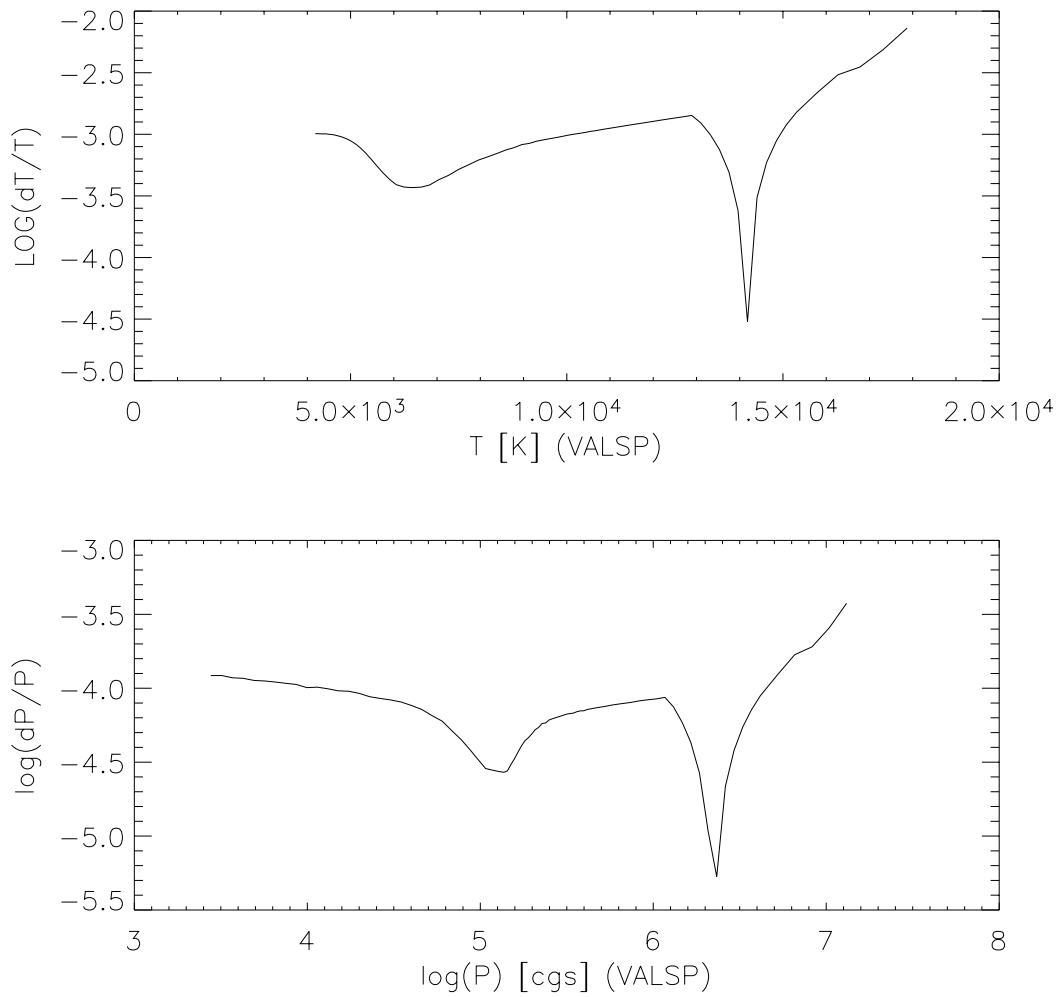


Figure 2.4: Relative difference between the VALSP model and the calculated values of temperature and pressure. For given VALSP values of temperature, density and internal energy the temperature and the pressure were calculated using our equation of state. The plots show the difference between calculated temperature and pressure and the values given in the VALSP model.

The available computing power does not permit us to resolve the diffusive length scales, which are of the order of centimeters owing to the low viscosity and correspondingly high Reynolds number in the solar convection zone. Thus, the simulations are large-eddy simulations, which simulate flows on resolvable scales and cut off the part of the energy, which lies below the grid scale. The code must provide some kind of numerical viscosity in order to prevent the build-up of energy at the grid scale. This is done by using hyperdiffusivities and shock-resolving diffusivities (Vögler 2003, Caunt and Korpi 2001).

The upper boundary of the computational domain is assumed to be closed, with stress-free conditions for the horizontal velocity components. The upper boundary of our simulation domain is located in the upper photosphere near the temperature minimum, where the density is rather low, so that the influence of the closed boundary on the dynamics of the granulation is negligible.

The lower boundary is located in the convectively unstable layers of the upper convection zone. Thus, an open boundary is implemented in order to allow free motions of the fluid through the boundary. Any formulation of the open boundary requires the knowledge of the physical conditions outside the domain, which is not directly available. Thus, the missing information is replaced by reasonable assumptions regarding the physical properties of the fluid at the boundary.

The first assumption is that the total pressure $p_{\text{tot}} = p_{\text{gas}} + |\mathbf{B}^2|/8\pi$ is constant across the lower boundary. This assumption is justified as long as the fluid motions are slow in comparison to the speed of magneto-acoustic waves (Vögler 2003). The magnetic field lines are forced to be vertical on the boundary. It implies that the net vertical magnetic flux in the simulation box remains constant in time.

The downflowing material in boundary regions leaves the box uninhibited. All inflows to the box are assumed to be vertical. The internal energy per unit mass for the inflowing gas ϵ_0 is assumed to be constant. The parameter ϵ_0 is used to control the net vertical energy flux through the computational domain and to make sure that the time-averaged value of the radiation flux density leaving the box is equal to the solar value $F_{\odot} = 6.34 \cdot 10^{10} \text{ erg s}^{-1} \text{ cm}^{-2}$.

Statistical fluctuations of the total mass in the simulated volume can be significant due to the small size of the computational domain. The total mass of the computational domain is kept constant with the precision of the order 10^{-4} by controlling the total pressure of the material flowing into the box.

Finally, the side boundaries are taken to be periodic in both horizontal directions.

2.4 Radiative transport in the MURaM code

Since the photosphere is the layer of the solar atmosphere where the transition from convective to radiative energy transport occurs, the code simulating magneto-convection in the photosphere has to include a detailed treatment of the radiative transport. The radiation field enters the MHD equations as the radiative heating rate per unit volume, Q_{rad} . The radiative heating rate is obtained by solving the radiative transfer equation (2.12) for a number of frequencies and directions, integrating the intensity $I_{\nu}(\boldsymbol{\mu})$ in order to determine the flux (Eq. 2.11) and then integrating the flux over all frequencies (Eq. 2.10).

Since the opacity in the solar atmosphere includes the contributions of about $10^6 - 10^7$ spectral lines, the direct modelling of the frequency-dependence in time-dependent two- and three-dimensional simulations is impossible due to computer performance limitations.

The most radical simplification is achieved by replacing the frequency-dependent opacity by an averaged value, e.g. the Rosseland mean. This simplification is called grey approximation. It is appropriate in the dense subphotospheric regions, and the radiative transport can be described as a local diffusion process. The grey approximation becomes unsatisfactory in optically thin layers, where the spectral lines affect the energy transport. The inclusion of line opacities in the calculations strongly modifies the temperature profiles, changes the photospheric dynamics and the emergent intensities. Therefore, a statistical treatment of the line opacities, which conserves the non-grey character of radiative transfer and reduces the computational requirements, is necessary.

The opacity binning approach is used in the code. It gives a reasonable approximation of the effect of frequency-dependence of the energy transport at grossly reduced computational cost.

The basic idea of opacity binning is to divide the frequency spectrum into 3-5 non-contiguous subsets (bins). The continuum opacities and lines of different strength are pooled in separate bins and represented by bin-averaged opacities. Assuming that the depth-dependence of the frequency-dependent opacity κ_ν is similar for the frequencies within one bin, a bin-average opacity $\bar{\kappa}_l$ is introduced, where l is the index of the bin. Thus, the frequency-dependent radiative transfer equation reduces to

$$\frac{dI_l}{ds} = -\bar{\kappa}_l \rho (I_l - B_l), \quad (2.31)$$

where I_l is bin-integrated intensity and B_l is bin-integrated source function (Planck function for LTE). For a given ray, Eq. (2.31) has to be solved for each of the 3-5 bins, thus strongly decreasing the computational time in comparison to a full frequency-dependent radiative transfer (spectral synthesis).

The bin-averaged opacities are calculated using τ -sorting procedure (Ludwig 1992). The radiative transfer equations for each bin and each direction are solved using the short-characteristics scheme (Kunasz and Auer 1988).

2.5 The results of radiative MHD simulations

The geometrical properties of the simulation domain are shown on Fig. 2.5. The size of the computational domain for the simulations considered here is $6000 \times 6000 \times 1400 \text{ km}^3$ with a resolution $288 \times 288 \times 100$ grid points. The simulation starts with a plane-parallel atmosphere extending between 800 km below and 600 km above the level of optical depth unity at 500 nm. After convection has developed and both the outgoing energy flux and the total kinetic energy have reached stationary values (with only short-term fluctuations on the granulation time scale), a homogeneous vertical magnetic field is introduced. We consider two runs with different initial magnetic field strengths of 10 G and 200 G corresponding to “quiet” and active solar regions, respectively. Within a few minutes of simulated time, most of the magnetic flux is assembled in the downflow regions of the convection pattern. After the decay of all transients caused by the introduction of the

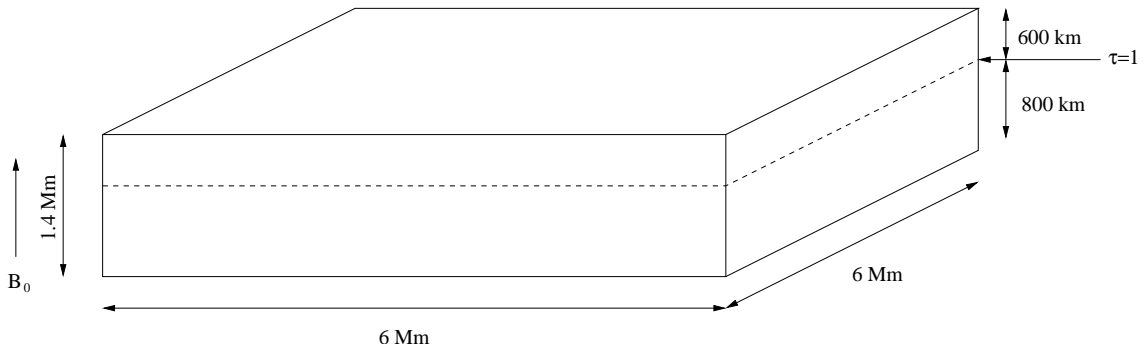


Figure 2.5: The simulation box. The vector \mathbf{B}_0 indicates the direction of the initial magnetic field, which is introduced in the beginning of the magnetic phase of the simulation.

magnetic field, we have continued the simulations for about another hour of solar time to be sure that the results have become independent of the initial distribution of magnetic flux. Some quantities from the 10 G and 200 G simulation snapshots are shown in Figs. 2.6 and 2.7. The 200 G snapshot is taken about 160 minutes after the start of simulation and 95 minutes after the vertical magnetic field was introduced. The 10 G snapshot is taken about 165 minutes after the start of the simulation and 45 minutes after the vertical magnetic field was introduced.

The lower-left parts of Figs. 2.6 and 2.7 show the temperature field at the continuum optical depth level $\tau = 1$ at 500 nm. The magnetic field maps in the upper-left panels show concentrations of magnetic flux up to 2700 G field strength in 200 G snapshot and up to 1800 G in 10 G snapshot. They are mainly located in intergranular downflow regions as evident from the map of the vertical velocity component shown on the upper-right panels. In the 10 G snapshot the magnetic field is concentrated in the regions of the strongest downflows on the mesogranular scale.

Most magnetic flux concentrations in the intergranular lanes correspond to local temperature enhancements (at constant optical depth) caused by partial evacuation and radiative heating of the flux concentrations by the hot surrounding plasma (Spruit 1976, Deinzer et al. 1984, Knölker et al. 1991, Vögler and Schüssler 2003). As shown in Fig. 2.8, to a very good approximation the magnetic flux concentrations are in total ($p_{\text{gas}} + |\mathbf{B}^2|/8\pi$) pressure balance with their environment up to the higher layers of the simulated atmosphere. This approximation (so-called thin flux tube approximation or slender tube approximation) assumes that the radius $r(z)$ of the tube at the height z is very much less than the vertical scale L_0 and leads to the reduction of the full MHD problem to a mathematically more simplified approach (Roberts and Webb 1978, Spruit and Roberts 1983). The vertical scale L_0 can be connected to the temperature height-scale.

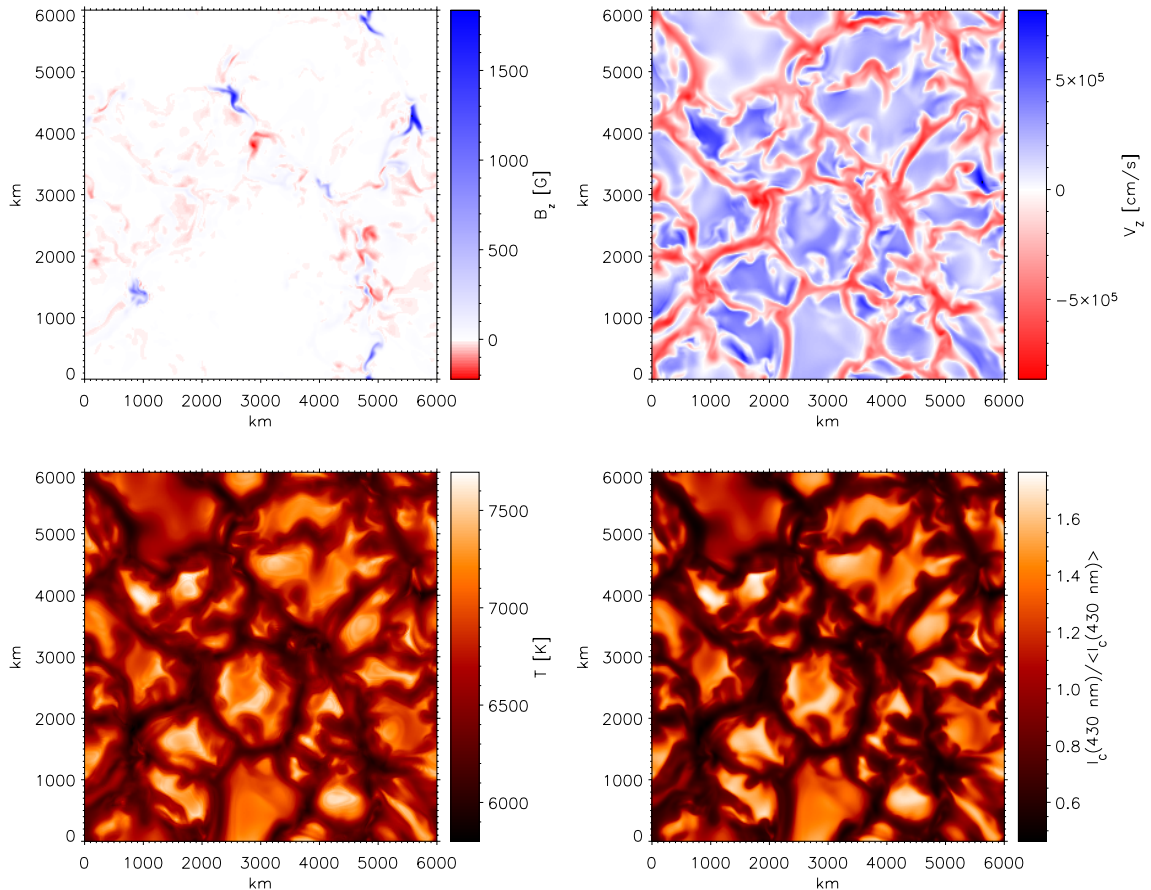


Figure 2.6: Maps of physical quantities for a snapshot from the run with 10 G average vertical magnetic field. Upper left: vertical component of the magnetic field at the level $\tau = 1$ at 500 nm, corresponding to the visible solar surface. The image shows a few magnetic flux concentrations in the intergranular lanes. Upper right: vertical component of the velocity at the level $\tau = 1$ at 500 nm. Positive (negative) values correspond to downflows (upflows). Lower left: gas temperature on the level $\tau = 1$ at 500 nm. There are local enhancements of the temperature in the regions of strong magnetic field in intergranular lanes. Lower right: normalized continuum intensity at 430 nm. The image shows bright granules with enhanced temperature, corresponding to the upflows and dark intergranular downflows.

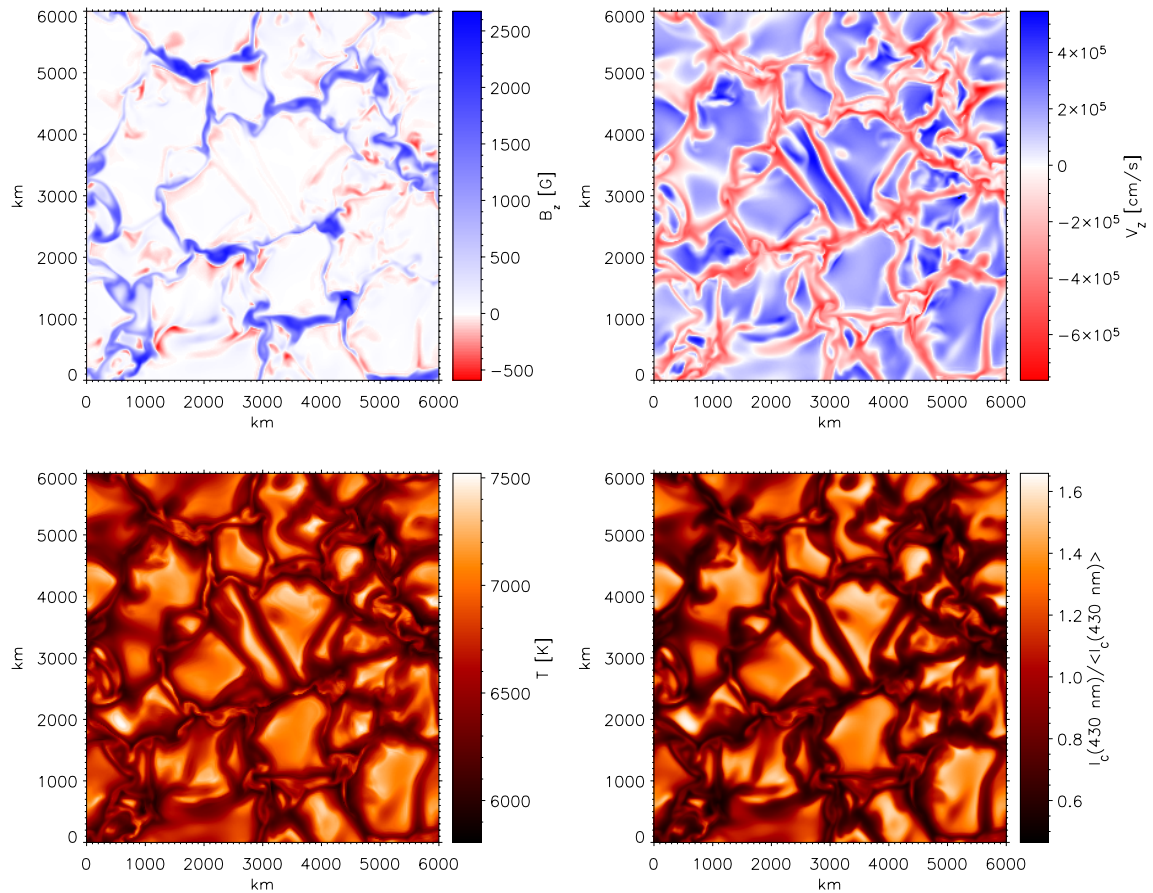


Figure 2.7: The same as Fig. 2.6 for the run with 200 G average vertical magnetic field. The image shows strong magnetic flux concentrations in the intergranular lanes. There are local enhancements of the temperature in the regions of strong magnetic field in intergranular lanes. The continuum intensity image (lower right) shows brightenings in the magnetic flux concentrations, which closely correspond to the local temperature enhancements.

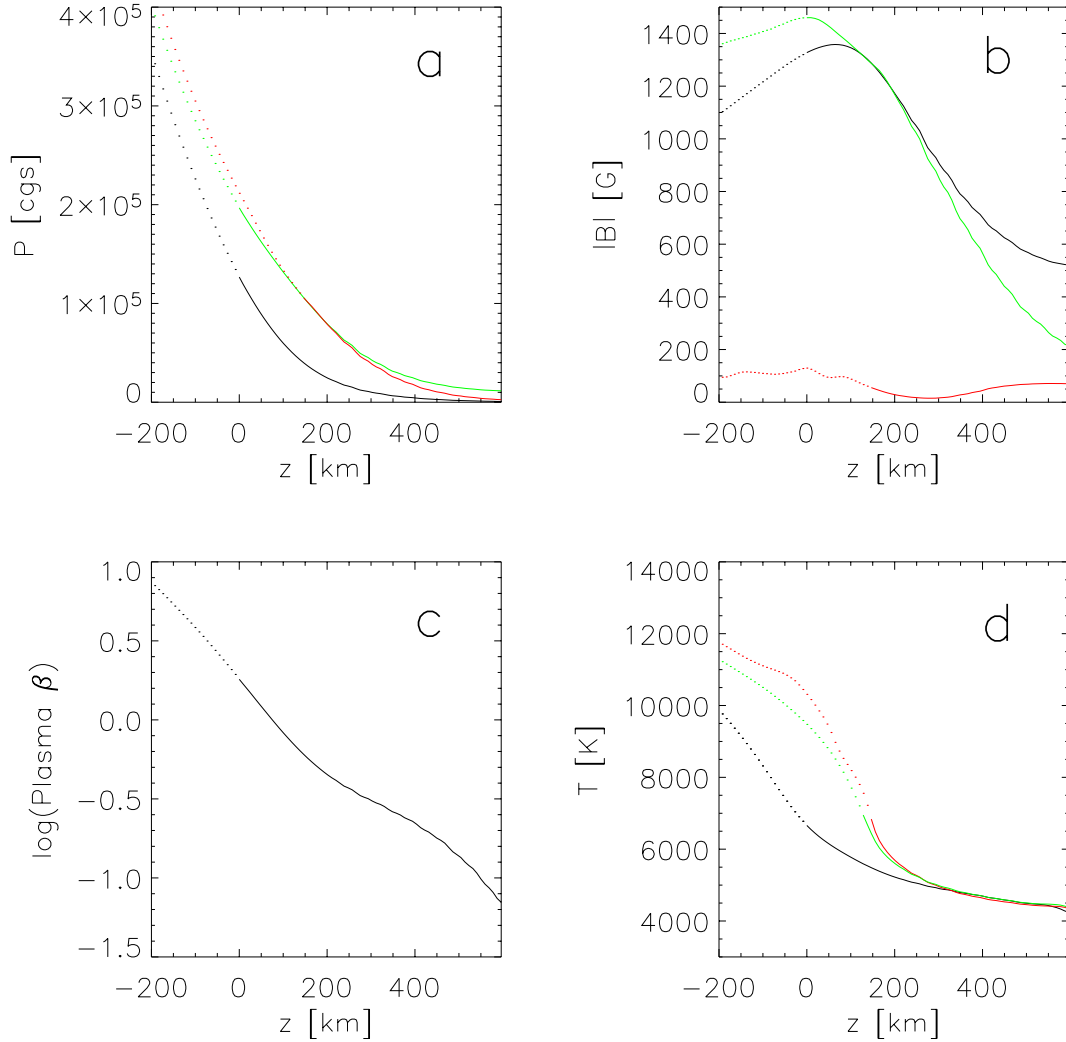


Figure 2.8: The dependence of pressure (a), magnetic field (b), plasma β (c), temperature (d) on the height, given for magnetic (black, $|B|_{\tau=1} > 1000$ G) and for non-magnetic (red, $|B|_{\tau=1} < 50$ G) points of the model. Zero height level corresponds to the optical level $\tau_{5000} = 0$. The green curve on plot (a) is the total pressure $p_{\text{tot}} = p_{\text{gas}} + |B|^2/8\pi$, the green curve on the plot (b) is the equivalent magnetic field strength derived from the total pressure in non-magnetic points, the green curve on the plot (d) is the average temperature. The dotted parts of the curves correspond to the parts of the atmosphere below the $\tau_{5000} = 1$ level. The plot shows that the thin-tube approximation is rather well applicable for magnetic features in the simulations.

3 Radiative transfer and line synthesis

In this chapter I briefly discuss the processes of spectral line formation in the solar photosphere. The influence of magnetic fields on the absorption lines results in line splitting governed by the Zeeman effect. In the following sections, the Zeeman effect for molecules and atoms and its connection to the transfer of radiation through the solar photosphere are described. The radiative transfer is treated using the formulation of the Unno-Rachkovsky equations for the Stokes vector, which describes the polarization state of the light.

3.1 Zeeman effect

The Zeeman effect consists in the splitting of a spectral line into several components. These components are usually collected in three groups: σ_b (blueshifted), σ_r (redshifted) and π (unshifted), which have different polarization properties.

The theory underlying the Zeeman effect (Zeeman 1897) is well-known (Landau and Lifshits 1989). The essence of the effect is the following. Let L , S , J and M_J be the quantum numbers which define the state of an atom. L characterizes the orbital angular momentum of the electrons, S their spin, J is total angular momentum, M_J is the “magnetic” quantum number, which determines the component of the total angular momentum in a given direction. M_J can take the values $-J, -J + 1, \dots, J$, while J can have the values $|L - S|, |L - S| + 1, \dots, L + S$. If the field strength B is zero, all the M_J states are degenerate and have the same energy. A non-vanishing magnetic field removes the degeneracy of M_J states and introduces a preferred direction, i.e. the direction of the magnetic field. The displacement of energy level can be written as

$$\Delta E = \frac{he}{4\pi m_e} g^* B, \quad (3.1)$$

so that the the displacement of the line from its original position, λ_0 , becomes

$$\Delta \lambda = \frac{e}{4\pi m_e c} g^* \lambda^2 B, \quad (3.2)$$

where B is the magnetic field strength and g^* is the Landé factor, defined as

$$g^* = g_u M_u - g_l M_l. \quad (3.3)$$

Here the g_u , g_l , M_u and M_l are the Landé factors and magnetic quantum numbers of the upper and lower states of the transition, respectively.

The Landé factors can be deduced theoretically or determined experimentally. In the first case, it is necessary to know the wavefunction of the states. For atomic states

correctly described by the L-S coupling scheme, the Landé factors are given by simple expression, which is valid for $J \neq 0$ (for $J = 0$ there is no splitting and the Landé factor is zero):

$$g_{LS} = \frac{3}{2} + \frac{S(S+1) - L(L+1)}{2J(J+1)}. \quad (3.4)$$

The selection rules for allowed dipole transitions, following from the Wigner-Eckart theorem, are:

$$\Delta J = 0, \pm 1, \text{ but } J = 0 \rightarrow 0 \text{ is forbidden,}$$

$$\Delta L = 0, \pm 1, \Delta S = 0$$

$$\Delta M = 0, \pm 1.$$

The line components σ_b and σ_r correspond to $\Delta M = \pm 1$ transitions, the component π corresponds to $\Delta M = 0$ transition.

The relative strengths of the components of Zeeman triplet (Landi Degl'Innocenti 2003) are given by the relation

$$S_q(M_l, M_u) = 3 \left(\begin{array}{ccc} J_l & J_u & 1 \\ -M_l & M_u & q \end{array} \right)^2, \quad (3.5)$$

where the expression in the brackets is Wigners $3j$ symbol value (Messiah 1962). Simplified expressions for the values of $3j$ symbols, used for quantum-mechanical calculations, are given by Condon and Shortley (1951). Here $q = 1$ corresponds to the blue-shifted, $q = -1$ to the redshifted, $q = 0$ to the central component of Zeeman triplet. The factor of 3 in the equation (3.5) assures normalization, so that the sum of the relative strengths over M_u and M_l equals to 1 (see Eq. (3.18)).

3.2 Stokes parameters

The decomposition of the harmonic oscillation of the electric field vector \mathbf{E} of a monochromatic electromagnetic wave propagating along the z -axis into the x and y components orthogonal to z is given by:

$$\begin{aligned} E_x &= A_x \cos(2\pi\nu t - \phi_x) \\ E_y &= A_y \cos(2\pi\nu t - \phi_y), \end{aligned} \quad (3.6)$$

where A_x and A_y are the amplitudes, ϕ_x and ϕ_y are the phase shifts and ν is the frequency.

Equivalent to the description by A_x , A_y , ϕ_x and ϕ_y is the description by the parameters introduced by G.G. Stokes in 1852. In the case of fully polarized wave, the four Stokes parameters are defined by:

$$\begin{aligned} I &\equiv A_x^2 + A_y^2 \\ Q &\equiv A_x^2 - A_y^2 \\ U &\equiv 2A_x A_y \cos(\phi_x - \phi_y) \\ V &\equiv 2A_x A_y \sin(\phi_x - \phi_y). \end{aligned} \quad (3.7)$$

It is easy to show that $I_\nu^2 = Q_\nu^2 + U_\nu^2 + V_\nu^2$.

Natural light is never perfectly monochromatic and fully polarized. So, in more general case, when the light is only partially polarized and the unpolarized component of the light $I_\nu^{\text{unpolarized}}$ exists, the first equation of (3.7) is transformed to:

$$I_\nu = I_\nu^{\text{unpolarized}} + A_x^2 + A_y^2. \quad (3.8)$$

The degree of polarization of partially polarized light here is defined as:

$$P = \left(\frac{Q^2 + U^2 + V^2}{I^2} \right). \quad (3.9)$$

The Stokes parameters have the advantage of being measurable by polarimetry. From the observational point of view, the Stokes parameters Q and U describe the intensity differences measured with two crossed in 45° linear polarimeters, and Stokes V parameter describes the difference between the intensities of left-handed and right-handed circularly polarized radiation (usually right-handed is assumed to be clockwise as seen by observer towards whom the light travels, looking back along the line of sight):

$$\begin{aligned} I_\nu &\equiv \text{total intensity} \\ Q_\nu &\equiv I_{0^\circ}^{\text{linear}} - I_{90^\circ}^{\text{linear}} \\ U_\nu &\equiv I_{+45^\circ}^{\text{linear}} - I_{-45^\circ}^{\text{linear}} \\ V_\nu &\equiv I_{\text{right}}^{\text{circular}} - I_{\text{left}}^{\text{circular}}. \end{aligned} \quad (3.10)$$

The four Stokes parameters are combined into the Stokes vector $\mathbf{I} = (I, V, Q, U)$ for use in matrix transformations (Mueller calculus), which quantitatively describe all effects of optical elements on a beam of light (Stenflo 1994).

3.3 Basics of radiative transfer and line synthesis

The detailed radiative transfer and line synthesis are treated here in the formulation given by Rees et al. (1989).

First we define the system of coordinates as shown in Fig. 3.1. The line of sight is oriented along the z axis. The angles γ and χ define the inclination of magnetic field with respect to the line of sight.

The transfer equation for the Stokes vector $\mathbf{I} = (I, V, Q, U)$ (also called Unno-Rachkovsky equation (Unno 1956)) is written as:

$$\frac{d\mathbf{I}}{dz} = -\mathbf{K}\mathbf{I} + \mathbf{j}, \quad (3.11)$$

where \mathbf{K} is the total absorption matrix,

$$\mathbf{K} = \kappa_c \mathbf{1} + \kappa_0 \Phi, \quad (3.12)$$

and \mathbf{j} is the total emission vector,

$$\mathbf{j} = \kappa_c S_c \mathbf{e}_0 + \kappa_0 S_l \Phi \mathbf{e}_0. \quad (3.13)$$

Here $\mathbf{1}$ is the unit 4x4 matrix, $\mathbf{e}_0 = (1, 0, 0, 0)$, κ_c and S_c are the absorption coefficient and source function in the unpolarized continuum, respectively. In Local Thermodynamic

Equilibrium (LTE) we have $S_c = B_\nu(T)$, the Planck function at the local temperature T . In LTE, the line source function S_l is also assumed to be determined by the local temperature, so that $S_l = S_c$. The line center absorption coefficient κ_0 (for zero damping, zero magnetic field and corrected for stimulated emission) is written in different ways for atomic and molecular lines and will be discussed in the following sections. The line absorption matrix is expressed via generalized absorption and anomalous dispersion profiles and is identical for atomic and molecular transitions, once the magnetic splitting pattern of the spectral line is prescribed:

$$\Phi = \begin{pmatrix} \phi_I & \phi_Q & \phi_U & \phi_V \\ \phi'_Q & \phi'_I & \phi'_V & -\phi'_U \\ \phi_U & -\phi'_V & \phi_I & \phi'_Q \\ \phi_V & \phi'_U & -\phi'_Q & \phi_I \end{pmatrix}, \quad (3.14)$$

where

$$\begin{aligned} \phi_I &= \frac{1}{2}\phi_p \sin^2 \gamma + \frac{1}{4}(\phi_r + \phi_b)(1 + \cos^2 \gamma), \\ \phi_Q &= \frac{1}{2}\left[\phi_p - \frac{1}{2}(\phi_r + \phi_b)\right] \sin^2 \gamma \cos 2\chi, \\ \phi_U &= \frac{1}{2}\left[\phi_p - \frac{1}{2}(\phi_r + \phi_b)\right] \sin^2 \gamma \cos 2\chi, \\ \phi_V &= \frac{1}{2}(\phi_r - \phi_b) \cos \gamma, \\ \phi'_Q &= \frac{1}{2}\left[\phi'_p - \frac{1}{2}(\phi'_r + \phi'_b)\right] \sin^2 \gamma \cos 2\chi, \\ \phi'_U &= \frac{1}{2}\left[\phi'_p - \frac{1}{2}(\phi'_r + \phi'_b)\right] \sin^2 \gamma \cos 2\chi, \\ \phi'_V &= \frac{1}{2}(\phi'_r + \phi'_b) \cos \gamma. \end{aligned} \quad (3.15)$$

The generalized absorption and anomalous dispersion profiles are denoted by $\phi_{p,b,r}$ and $\phi'_{p,b,r}$. The profiles $\phi'_{p,b,r}$, which describe magneto-optical effects, are usually neglected (Auer et al. 1977). For a normal triplet, the indices p , b and r refer to the unshifted π component and the *blue*- and *red*-shifted σ components of a profile, respectively.

Let $N_{p,b,r}$ be the quantum numbers of the Zeeman components of each type, governed by the selection rules,

$$\Delta M = M_u - M_l = \begin{cases} +1 \equiv b, \\ 0 \equiv p, \\ -1 \equiv r, \end{cases} \quad (3.16)$$

where M_u and M_l are the magnetic quantum numbers of the Zeeman levels in the upper and lower states of the line transition. Level $k(= u, l)$ splits into $2J_k + 1$ Zeeman states, $M_k = -J_k, \dots, +J_k$. The wavelength shift of the Zeeman component i_j (where $j = p, b, r$, $i_{p,b,r} = 1, \dots, N_{p,b,r}$) according to Eq. (3.2) is:

$$\Delta\lambda_{i_j} = \frac{e\lambda_0^2 B}{4\pi m_e c^2} (g_l M_l - g_u M_u)_{i_j}. \quad (3.17)$$

The strength of the component i_j is S_{i_j} , and

$$\sum_{i_j=1}^{N_j} S_{i_j} = 1, \quad j = p, b, r. \quad (3.18)$$

The generalized profiles ϕ_j can be written as

$$\phi_j = \sum_{i_j=1}^{N_j} S_{i_j} H(a, v - v_{i_j} + v_{los}), \quad (3.19)$$

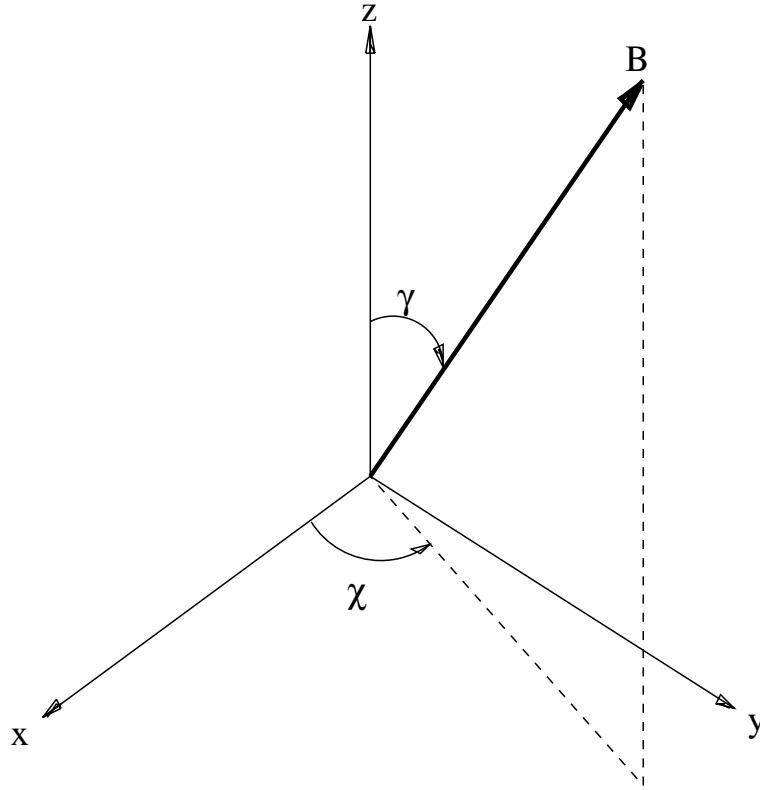


Figure 3.1: Reference frame in which the Stokes vector I and magnetic field vector B are defined. The z axis corresponds to the line of sight.

where $H(a, v)$ is the Voigt profile

$$H(a, v) = \frac{a}{\pi} \int_{-\infty}^{\infty} \frac{e^{-y^2}}{(v - y)^2 + a^2} dy. \quad (3.20)$$

The parameters in the equations (3.19) and (3.20) are written in the units of Doppler width $\Delta\lambda_D$:

$$a = \Gamma \lambda_0^2 / 4\pi c \Delta\lambda_D, \quad (3.21)$$

where Γ is the line damping parameter,

$$v = (\lambda - \lambda_0) / \Delta\lambda_D, \quad (3.22)$$

λ is the wavelength in the line,

$$v_{ij} = \Delta\lambda_{ij} / \Delta\lambda_D, \quad (3.23)$$

and the Doppler shift induced by a macroscopic velocity field \mathbf{v}_{mac}

$$v_{los} = \lambda_0 \mathbf{v}_{mac} \cdot \mathbf{n} / c \Delta\lambda_D. \quad (3.24)$$

Here, the Doppler width $\Delta\lambda_D$ is expressed as

$$\Delta\lambda_D = \lambda_0 \frac{v_T}{c}, \quad (3.25)$$

where (under the assumption of Maxwellian velocity distribution) $v_T = (2kT/m)^{1/2}$, T is kinetic temperature of the plasma, m is the atomic weight.

The line damping parameter Γ consists of two parts, i.e. collisional damping and radiative damping, and often is corrected by an empirical factor. Radiative damping is connected to the uncertainty of the energy of the atomic levels owing to their finite lifetime. The collisional broadening is determined as $\Gamma = 2/\tau$, where τ is the mean time between atomic collisions (resonance and van der Waals damping) or of a charged particle and an atom (linear and quadratic Stark effects) (Mihalas 1978).

The continuum absorption coefficient at any given frequency contains contributions from all possible transitions (bound-free, free-free) of all chemical species (atoms and molecules) which can absorb photons at that frequency. Under the LTE assumption, continuum absorption coefficient can be written as (Mihalas 1978):

$$\kappa_c(\nu) = \left[\sum_i n_i \alpha_{ik}(\nu) + \sum_k n_e n_k \alpha_{kk}(\nu, T) \right] \times (1 - e^{-h\nu/kT}), \quad (3.26)$$

where the scattering term is neglected. Here the bound-bound, bound-free, free-free transitions correspond to the first, second and third term, respectively. n_i is the LTE population of state i calculated from the Saha-Boltzmann equation (2.20), describing the chemical equilibrium in LTE. α_{ij} , α_{ik} , α_{kk} are absorption cross-sections for bound-bound, bound-free and free-free transitions. They are calculated by means of quantum mechanics and usually are given in tables.

The line center absorption coefficients are reviewed in the next sections.

3.4 Atomic lines

For the ij -th transition in an atom in ionization state k , the line center absorption coefficient is given by:

$$\kappa_0^{\text{at}} = \frac{\sqrt{\pi} e^2}{m_e c^2} \frac{\lambda_0^2}{\Delta\lambda_D} f_{ij} \frac{N_{ik} g_{ik}}{Q_k(T)} e^{-\chi_{ik}/kT} (1 - e^{-hc/\lambda_0 kT}), \quad (3.27)$$

where λ_0 is the line center wavelength, f_{ij} is the oscillator strength, N_{ik} is the number density of the atom in ionization state k , $Q_k(T)$ is the temperature-dependent partition function of the atom in the ionization stage k ,

$$Q_k(T) = \sum_i g_{i,k} e^{-\chi_{i,k}/kT}, \quad (3.28)$$

where $\chi_{i,k}$ are the excitation energies of level i in the atom in the ionization state k , and g_{ik} are the statistical weights of the level i in the atom in the ionization state k .

The center wavelength, oscillator strength, excitation energy and statistical weight for a line are given in tables and usually are taken as input parameters of the line synthesis programs. The number densities are derived from the Saha equation using the procedure, similar to the one discussed in Sect. 2.2.

3.5 Molecular lines

The molecular line center absorption coefficient is calculated as follows:

$$\kappa_0^{\text{mol}} = \frac{\sqrt{\pi}e^2}{m_e c^2} \frac{\lambda_{J',J''}^2}{\Delta\lambda_D} f_{J',J''} N \frac{2J'' + 1}{Q} e^{-E_{J''}/kT} (1 - e^{-hc/\lambda_0 kT}), \quad (3.29)$$

where $f_{J',J''}$ is the absorption oscillator strength, N is the number density of a given molecule, Q is its partition function, J' and J'' correspond to the upper and lower levels of the transition, $\lambda_{J',J''}$ is the wavelength of the transition, $\Delta\lambda_D$ is the Doppler width (3.25), and $E_{J''}$ is the lower level excitation energy.

The absorption oscillator strength $f_{J',J''}$ is given by the relation

$$f_{J',J''} = f_{v'v''} \frac{S_{J',J''}}{2J'' + 1} \frac{\lambda_{v'v''}}{\lambda_{J',J''}}, \quad (3.30)$$

where $f_{v'v''}$ and $\lambda_{v'v''}$ are the oscillator strength and the wavelength of the vibrational band (v', v'') within which the rotational transition occurs. These parameters are taken from laboratory measurements. The oscillator strength is related to the Hönl-London factor (Schadee 1964), which represents the full theoretical strength of the molecular line. It is different for different molecules and transitions.

The G-band wavelength range is mainly covered by the lines of CH molecule and some atomic lines. Thus, here we are interested in the synthesis of the lines produced by CH molecules, and the following discussion will be about the parameters of the CH molecule only.

The behaviour of molecules in a magnetic field is different from the behaviour of atoms. A detailed discussion of the molecular Zeeman effect can be found in the paper of Berdyugina and Solanki (2002). Here we give a brief summary.

The molecular state of the diatomic CH molecule (in Hund's case b, see Berdyugina and Solanki (2002)) is described by five quantum numbers Λ, S, N, J, M , where $\Lambda = 0, 1, 2 \dots L$ is the orbital angular momentum of electron, S is spin angular momentum of electron, $N = \Lambda, \Lambda + 1, \Lambda + 2, \dots$ is the angular momentum of nuclear rotation (the angular momentum excluding spin), $J = N + S, N + S - 1, N + S - 2, \dots, |N - S|$ is the total angular momentum including spin, $M = J, J - 1, \dots, -J + 1, J$ is the projection of the total angular momentum on the magnetic field direction (magnetic quantum number). The vector diagram for a diatomic molecule in Hund's case (b) is shown on the Fig. 3.2.

The magnetic splitting of the rotational level J is expressed as:

$$\begin{aligned} \Delta E = \mu_0 B \frac{M}{J(J+1)} \left\{ \frac{\Lambda^2}{2N(N+1)} \times \right. & (3.31) \\ \times [J(J+1) + N(N+1) - S(S+1)] + & \\ \left. + J(J+1) - N(N+1) + S(S+1) \right\} = \mu_0 B \cdot gM, & \end{aligned}$$

where B is the external magnetic field and g is the analogue of the Landé factor. The Zeeman displacement for a transition between the upper level $\Lambda_u, S_u, N_u, J_u, M_u$ and the lower level $\Lambda_l, S_l, N_l, J_l, M_l$ is calculated according to Eqs. (3.3) and (3.2) with Landé factors given by Eq. (3.32).

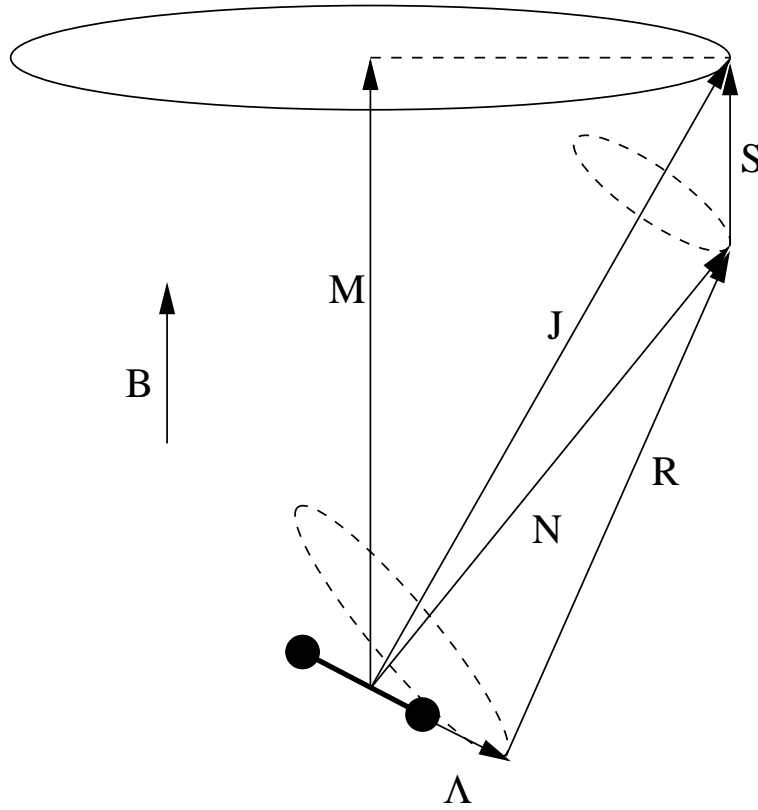


Figure 3.2: Vector diagram of a diatomic molecule. Solid ellipse indicates the precession of \mathbf{J} in the magnetic field \mathbf{B} . The nutation of $\mathbf{\Lambda}$ about \mathbf{N} is much faster than the precession of \mathbf{N} and \mathbf{S} about \mathbf{J} , while the latter is much faster than the precession of \mathbf{J} in the magnetic field. The faster motions are shown by dashed-line ellipses. \mathbf{R} is the angular momentum of nuclear rotation.

The strengths of transitions S between the Zeeman sublevels can be represented as a product of two parts, the first depending on Λ , J and N , the second depending on J and M :

$$S = S_{N_l N_u} S_{M_l M_u}, \quad (3.32)$$

where $S_{N_l N_u}$ is the Hönl-London factor (see Schadee (1964)). The strengths of Zeeman components $S_{M_l M_u}$ are given in the paper of Berdyugina et al. (2003).

3.6 Spectral line calculations

The spectral lines are calculated using the STOPRO routine. The first version of the STOPRO routine was written by S.K. Solanki and described in his thesis (Solanki 1987). Later a set of routines implementing the DELO (Diagonal Element Lambda Operator) technique (Rees et al. 1989) was incorporated for the solution of the Unno-Rachkovsky equations. Response functions were added to the code by C. Frutiger, M. Fligge and J.H.M.J. Bruls. The calculation of molecular lines was added by S. Berdyugina in collaboration with C. Frutiger.

The STOPRO routine calculates the four Stokes parameters I , V , Q and U of one or

more spectral lines upon input of their atomic data and one or more model atmospheres. The code generally assumes LTE. An interface to the non-LTE code MULTI by Mats Carlson in order to use non-LTE departure coefficients in radiative transfer has been added by C. Frutiger.

The parameters of the input atmosphere, which are required by STOPRO are described in Table 3.1, while the direct output quantities of the MURaM code are given in Table 3.2.

N	Quantity	Dimension
1	$\log \tau$	[-]
2	Height z	[cm]
3	Temperature T	[K]
4	Pressure p	[g cm ⁻¹ s ⁻²]
5	Electron pressure p_e	[g cm ⁻¹ s ⁻²]
6	Continuum absorption coefficient κ	[g ⁻¹]
7	Density ρ	[g cm ⁻³]
8	Magnetic field strength $ B $	[G]
9	Micro-turbulence velocity	[cm · s ⁻¹]
10	Line-of-sight velocity	[cm · s ⁻¹]
11	γ (angle between B and LOS)	[deg]
12	χ (azimutal angle of B)	[deg]

Table 3.1: Input quantities, required by the STOPRO routine for the line profiles calculations.

N	Quantity	Dimension
1	Temperature T	[K]
2	Pressure p	[g cm ⁻¹ s ⁻²]
3	Horizontal velocity components v_x, v_z	[cm/s]
4	Vertical velocity component v_y	[cm/s]
5	Internal energy per unit volume	[erg cm ⁻³]
6	Horizontal magnetic field components B_x, B_z	[G]
7	Vertical magnetic field component B_y	[G]

Table 3.2: Output quantities of the MURaM code.

In order to obtain the quantities, which are not delivered by the MURaM code, the MODCON subroutine was used. This subroutine calculates the ionization equilibrium (Sec. 2.2) for a given chemical composition and, derives electron pressure p_e , continuum optical depth, τ , and continuum absorption coefficient, κ (for a given wavelength), according to Eq. 3.26.

The atomic/molecular input data file specifies the lines to be calculated and provides the necessary atomic and molecular data for calculation. The file may contain one or more spectral lines. The required parameters for atomic and molecular lines are different; they are given in the Tables 3.3 and 3.4, respectively.

N	Variable	Description	Dimension
1	NLINES	Number of lines	[-]
2	WLREF	Reference wavelength (line center)	[Å]
3	WL1 WL2 NWL	wavelength grid $\lambda_i = WLREF - WL1 + i \frac{WL2 - WL1}{NWL},$ $i = 1, \dots, NWL$	[Å]
4	NATOM	Atomic number, e.g. Fe=26	[-]
5	ION	Ionization state. 1-neutral, 2=+, ION ≥ 3 is not allowed	[-]
6	ALOGGF	Logarithm of oscillator strength	[-]
7	ABUND	Abundance of the element on a log scale, A(H) = 12.0	[-]
8	EPOT	Energy of the lower level	[eV]
9	IPOT1	First ionization potential $X \rightarrow X^+$	[eV]
10	IPOT2	Second ionization potential $X^+ \rightarrow X^{++}$	[eV]
11	RMASS	Atomic mass	[amu]
12	DMPEMP	Empirical damping enhancement factor	[-]
13	LANDEC	{ =0: g_u and g_l are calculated from L,J,S =1: g_u and g_l are taken from input (see 18)	[-]
14	CFGL	Term description of the lower level	[-]
15	$2S_l + 1$ L_l J_l	Standard term description of the lower level $^{2S_l+1}L_l J_l$	[-]
16	CFGU	Term description of the upper level	[-]
17	$2S_u + 1$ L_u J_u	Standard term description of the upper level $^{2S_u+1}L_u J_u$	[-]
18	GL	Landé factor of the lower level g_l (used if LANDEC=1, see 13)	[-]
19	GU	Landé factor of the upper level g_u (used if LANDEC=1, see 13)	[-]

Table 3.3: The description of atomic data record, required by the STOPRO.

We have developed the program LINE, which calculates the Stokes parameters for the 3D atmosphere simulated by the MURaM code. The program uses STOPRO and MODCON as subroutines. In order to obtain additional diagnostic parameters such as abundances and line center absorption coefficients, the STOPRO code was modified accordingly.

Especially for the the G-band spectrum, which consists of hundreds of molecular and atomic lines, the calculation requires significant computing resources. To reduce the computational time, the program was parallelized. During initialization, the program creates a number of threads corresponding to the number of available processors. Each of the threads consists of a local copy of the MODCON and STOPRO subroutines. The program

N	Variable	Description	Dimension
1	NLINES	Number of line blends	[-]
2	WLREF	Reference wavelength (line center)	[Å]
3	$\left. \begin{array}{l} \text{WL1} \\ \text{WL2} \\ \text{NWL} \end{array} \right\}$	wavelength grid $\lambda_i = WLREF - WL1 + i \frac{WL2 - WL1}{NWL},$ $i = 1, \dots, NWL$	[Å]
4	NMOLEC	Notation in the form of an integer comprising the numbers of the atoms in the molecule, e.g. 601=CH	[-]
5	$\left. \begin{array}{l} \text{ABUND1} \\ \text{ABUND2} \end{array} \right\}$	abundances of the atoms comprising the molecule	[-]
6	BRANCH	branch name='R','P','Q'	[-]
7	IU, IL	upper and lower multiplet sublevels = 1,2,3,...	[-]
8	JL	low rotational number = 0,1,2,3,... or 0.5,1.5,2.5,...	[-]
9	VU, VL	upper and lower vibrational levels = 0,1,2,3,...	[-]
10	FVV	band oscillator strengths	[-]

Table 3.4: The description of molecular data record, required by the STOPRO.

loads the atmospheric model and continuously distributes it ray by ray over the threads until the whole computational domain is covered. The threads calculate the Stokes parameters independently of each other, so that the processors do not have to communicate during the calculation. The calculated spectra are stored in an array which is common for all threads. Since the processors do not communicate during the most expensive part of the computation, the performance scales linearly with the number of available processors. The MPI-1.0 standard library was used for parallelization. The program was running on IBM SP/3 supercomputer at Gesellschaft für wissenschaftliche Datenverarbeitung mbH Göttingen (GWDG).

The output of the LINE program consists of a file containing the 3D atmosphere, converted to the τ -scale, and a file containing the Stokes parameters. Optionally, it is also possible to save the abundance of the CH molecule and the absorption coefficient for the line center of a selected CH line.

4 Fe I lines diagnostics

The radiative diagnostics based on the spectral lines of neutral iron (Fe I) at the wavelengths 630.15 nm, 630.25 nm, 1564.85 nm and 1565.28 nm is presented in this chapter. The general properties of the selected lines and their observational use are described in first section. Second section is dedicated to the results of the radiative diagnostics based on these lines. The comparison of the simulations with the observational data is presented in third section. Fourth section - conclusions.

4.1 Selected lines of Fe I

Measurements of the solar magnetic fields are mostly based on polarimetric observations of spectral lines. In particular, spectral lines of iron have often been used for the polarimetric observations (Kneer and Stolpe 1996, Kneer et al. 1996, Rüedi et al. 1992, Solanki 1993). The very large number of infrared, visible and ultraviolet spectral lines of iron results from the complexity of the iron atom, which contains about 300 identified terms and 5000 multiplets. The iron absorption lines are easy to observe owing to the high abundance of iron in the solar atmosphere.

The Fe I lines at 630.15 nm, 630.25 nm, 1564.85 nm and 1565.28 nm were selected to provide the radiative diagnostics of our MHD model. These lines have often been used for polarimetric studies because they are not blended by other lines, and because the two pairs of visible and infrared lines, respectively, can be observed simultaneously by one instrument due to their proximity in wavelength. The main properties of the transitions corresponding to these lines, such as the transition wavelength, the transition term, the effective Landé factors, the excitation potentials of the lower levels and the weighted logarithmic oscillator strengths, are given in Table 4.1.

Wavelength [nm]	Transition	g_{eff}	χ_e [eV]	$\log(g^*f)$
630.15	$z^5P_2^0 - e^5D_2$	1.66	3.654	-0.718
630.25	$z^5P_1^0 - e^5D_0$	2.5*	3.686	-1.235
1564.85	$e^7D_1 - 3d^64s5p^7D_1^0$	3*	5.43	-0.652
1565.28	$f^7D_5 - (9/2)[7/2]_4^0$	1.53	6.25	-0.050

Table 4.1: Atomic transition parameters for the lines used for the radiative diagnostics. *These lines are Zeeman triplets, so that the g_{eff} value corresponds to the true Landé factor of the line.

The lines are calculated assuming LTE. The validity of this assumption for calcula-

tions of Fe I lines has been analyzed by Shchukina and Trujillo Bueno (2001). For the 630.15 nm and 630.25 nm Fe I lines these authors show that abandoning the LTE assumption in the calculations leads to changes in the profiles emerging from granular regions and also in the average profiles. This is caused by the underpopulation of the all Fe I levels due to overionization by the near-UV radiation field mainly in the granular regions and results in a slight weakening of the Fe I profiles in comparison to the calculations under the assumption of LTE.

Infrared spectral lines can give more precise information about the magnetic fields compared to lines in the visible due to the quadratic dependence of the Zeeman splitting on wavelength compared to the linear dependence of the line width on wavelength. The magnetic sensitivity of the infrared 1564.85 nm and 1565.28 nm Fe I lines is discussed by Solanki et al. (1992). The IR lines allow the magnetic fields in solar magnetic features to be measured with great accuracy due to their small temperature sensitivity and the large Landé factors. The 1564.85 nm Fe I line has $g = 3$, which allows it to reliably measure magnetic field strengths as low as 200-300 G. Compared to lines in the visible, they are also formed deeper in the atmosphere. These lines are definitely the most widely used lines in the infrared for solar magnetic field diagnostics. For example, they are the standard lines employed by the Advanced Stokes Polarimeter (ASP, Tomczyk et al. (1992)), in the POLIS spectrograph at the VTT on Tenerife (Schmidt et al. 2003), in the spectropolarimeter to fly on Solar B (Shimizu 2002) and on SUNRISE (Solanki et al. 2002, 2003).

The visible Fe I lines at 630.15 nm and 630.25 nm are widely used. Compared to the other widely used line pair of Fe I 524.7 nm and 525.0 nm, the lines 630 nm have the advantage of being less temperature sensitive and being formed somewhat deeper in the atmosphere, so that they are less affected by the upper boundary of the simulation box.

Simultaneous observations of the visible and infrared Fe I lines show the kilogauss magnetic field strengths measured with the visible lines and sub-kilogauss strengths traced by the infrared lines for the same region (Sánchez Almeida et al. 2003). These authors interpret their observations in terms of the existence of magnetic structures with different field strengths (and even of the opposite polarities) in one resolution element.

4.2 Diagnostics of simulation results

In the following sections we consider the simulation results for the two snapshots taken from 200 G and 10 G average magnetic field simulations. The vertical magnetic and velocity fields for these snapshots are shown in Fig. 4.1. The 200 G snapshot represents an active solar region with large amount of magnetic flux concentrations located in the regions of strong downflows. The 10 G snapshot is almost non-magnetic and represents weakly magnetized solar granulation.

4.2.1 General properties of the simulation results

We have calculated all four Stokes profiles of the Fe I lines for a snapshots from each of the runs with 200 G and 10 G average magnetic field strength. The results of the calculations are presented in Figs. 4.2 and 4.3, respectively, which show the continuum

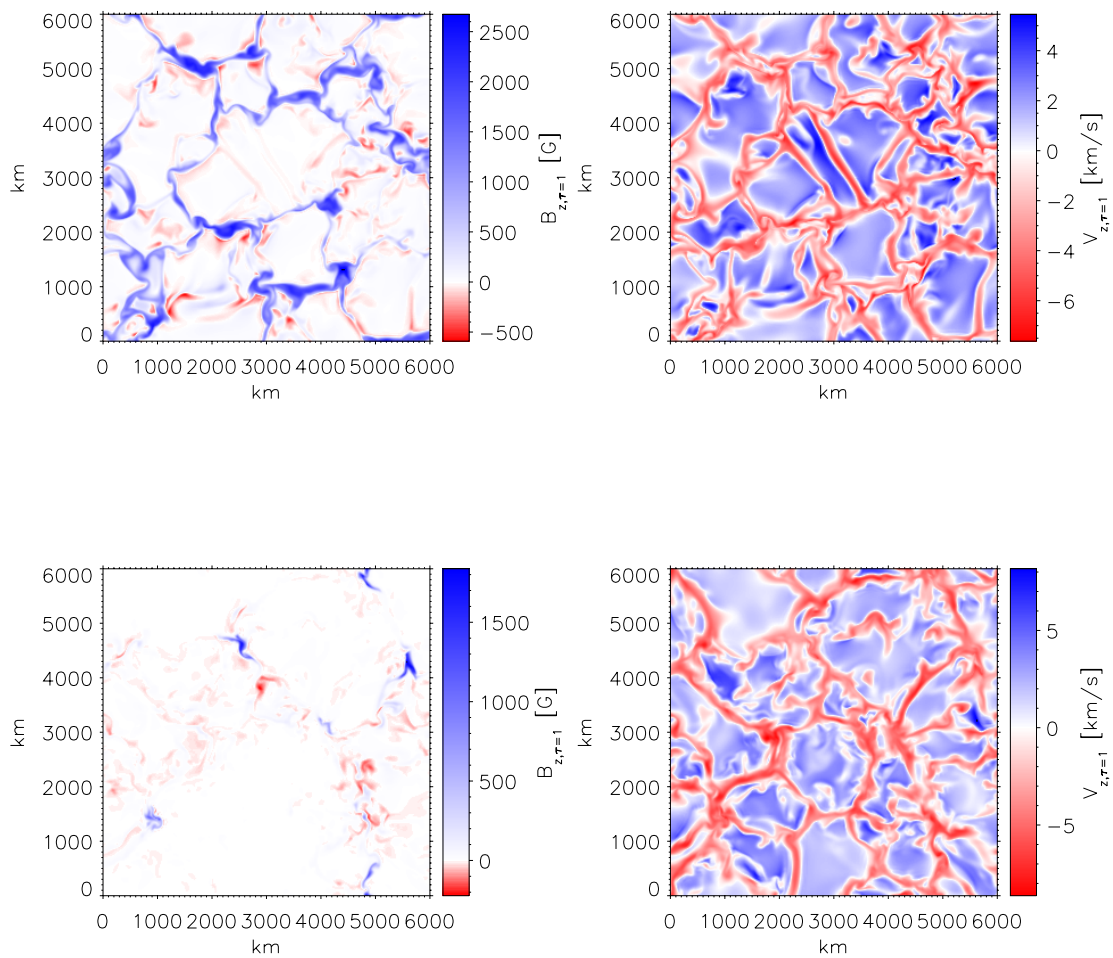


Figure 4.1: Vertical magnetic field strength (left panels) and vertical velocity (right panels) for the snapshots from the 200 G (upper panels) and 10 G (lower panels) average magnetic field simulations. Negative values of the velocity field correspond to downflows.

intensity at 630.2 nm, together with what we call the line strength for the 630.2 nm line, defined as

$$S = \frac{1}{\lambda_0} \int \frac{(I_c - I)}{I_c} d\lambda, \quad (4.1)$$

the total Stokes- V areas, defined as

$$A_V = \int \frac{|V|}{I_c} d\lambda, \quad (4.2)$$

and the normalized Stokes- V area asymmetries, defined as

$$\delta A_V = \int \frac{V}{|V|} d\lambda, \quad (4.3)$$

for the 630.2 nm and 1564.8 nm Fe I lines, respectively. The continuum image (upper left panel) for the 200 G case shows small brightness enhancements corresponding to the regions of strong vertical magnetic field, as can be seen from the total Stokes- V area maps (middle-left and bottom-left images). In the image of the line strength, defined in Eq. (4.1), one can see strong line weakenings in the regions of the strong magnetic field. The maps of normalized Stokes- V area asymmetry indicate significant asymmetry near the edges of strong field regions while their centers show almost no asymmetry. The total Stokes- V area in both lines follows the total field strength quite well, at least qualitatively. Differences between the two lines are visible, however, with the contrast in A_V between the regions with strong and weak field being larger for the 630.2 nm line than for the IR line. The contrast is even larger for the 630.1 nm line (not shown). This is due to the larger Zeeman sensitivity of the 1564.8 nm line. The asymmetry δA_V is considerably larger for the visible line, due to its larger strength and smaller Zeeman splitting. Other than that, however, the δA_V images produced in both lines are relatively similar. The dominantly positive value of δA_V corresponds to the blue lobe of Stokes- V profile having larger area than the red lobe. These points will be discussed in greater detail later.

The 10 G case images represent a “quiet” solar region with low magnetic flux. The continuum image in the upper-left panel of Fig. 4.3 shows a nearly undisturbed granulation pattern, in contrast to the granules in Fig. 4.2, which have smoother edges. The total Stokes- V area maps (middle left and lower left panels) show signal only in isolated patches. The magnetic flux is mainly concentrated in a few small isolated magnetic structures. The elongated thin sheet-like magnetic field concentrations, which are revealed on the total Stokes- V area image calculated for the Fe I 1564.8 nm line (lower left panel), outline a long-living “mesogranular” pattern (Domínguez Cerdeña 2003). The images of the normalized Stokes- V area asymmetry (middle and lower right panels of Fig. 4.3) show almost no correspondence to the structures in the continuum image, because very weak granular magnetic fields show strong asymmetries.

The vertical component of the velocity field at the $\log \tau_{500} = 0$, the modulus of the magnetic field strength at the same level, the Doppler velocity shifts and the line widths, calculated for the Fe I 630.2 nm and 1564.8 nm lines for the 200 G and 10 G snapshots, respectively, are shown in Figs. 4.4 and 4.5. The vertical component of the velocity (upper left panels) shows strong downflows in the intergranular regions, which, for the 200 G case often, but not always, harbour strong magnetic fields, if comparison is made with the

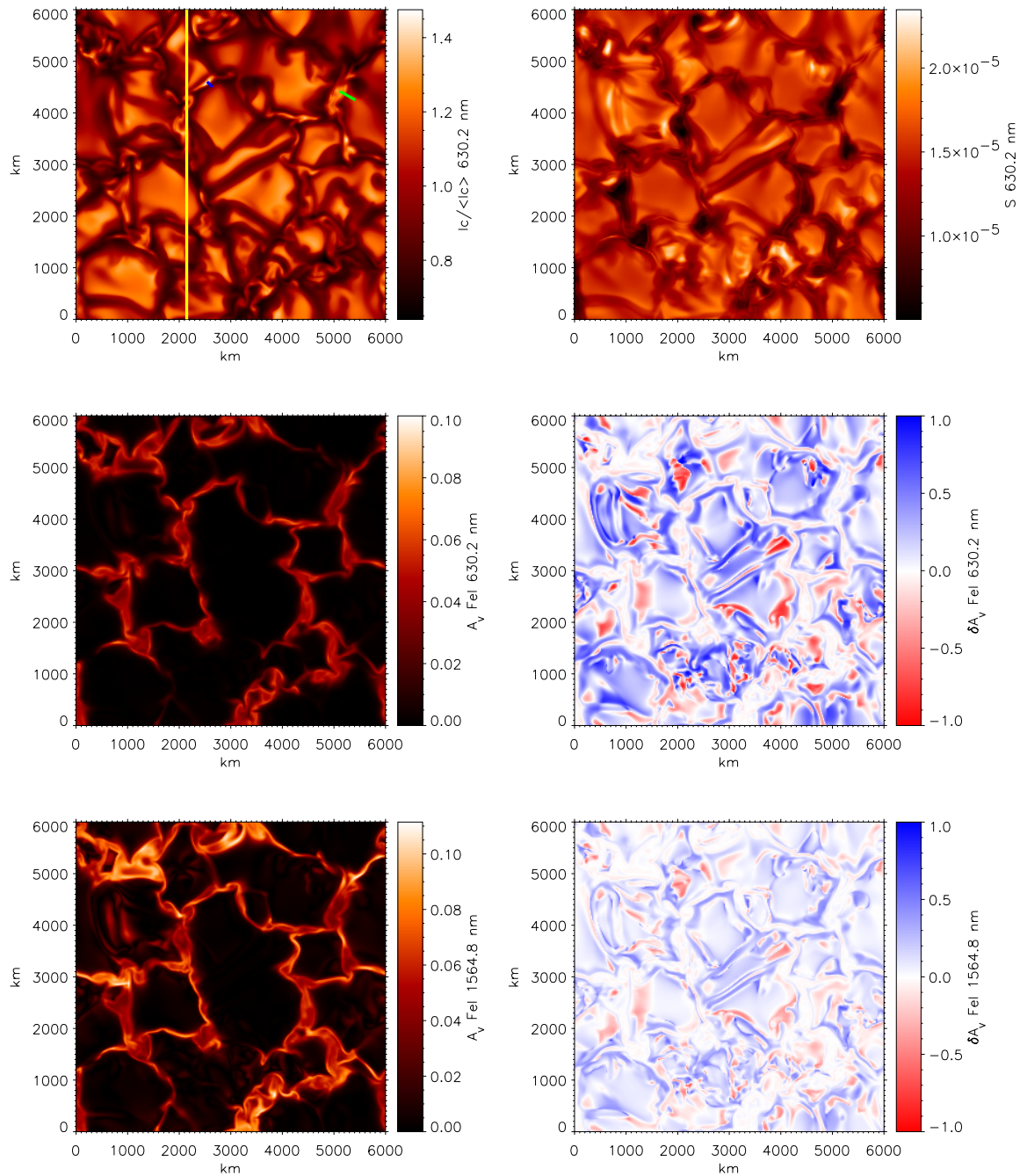


Figure 4.2: Continuum intensity, $I_c / \langle I_c \rangle$, line strength, total Stokes-V area and relative area asymmetry calculated for the 630.2 nm and 1564.8 nm Fe I lines for the snapshot from the 200 G average magnetic field simulation (top 4 frames). The Stokes-V area and relative area asymmetry of the Fe I 1564.8 nm line is plotted in the two lowest panels. The slit position for Figs. 4.19, 4.20, 4.21, 4.22 is marked by yellow line on the continuum intensity image. The thin and thick magnetic feature cuts shown in Figs. 4.7 and 4.10 are marked by the green and blue lines.

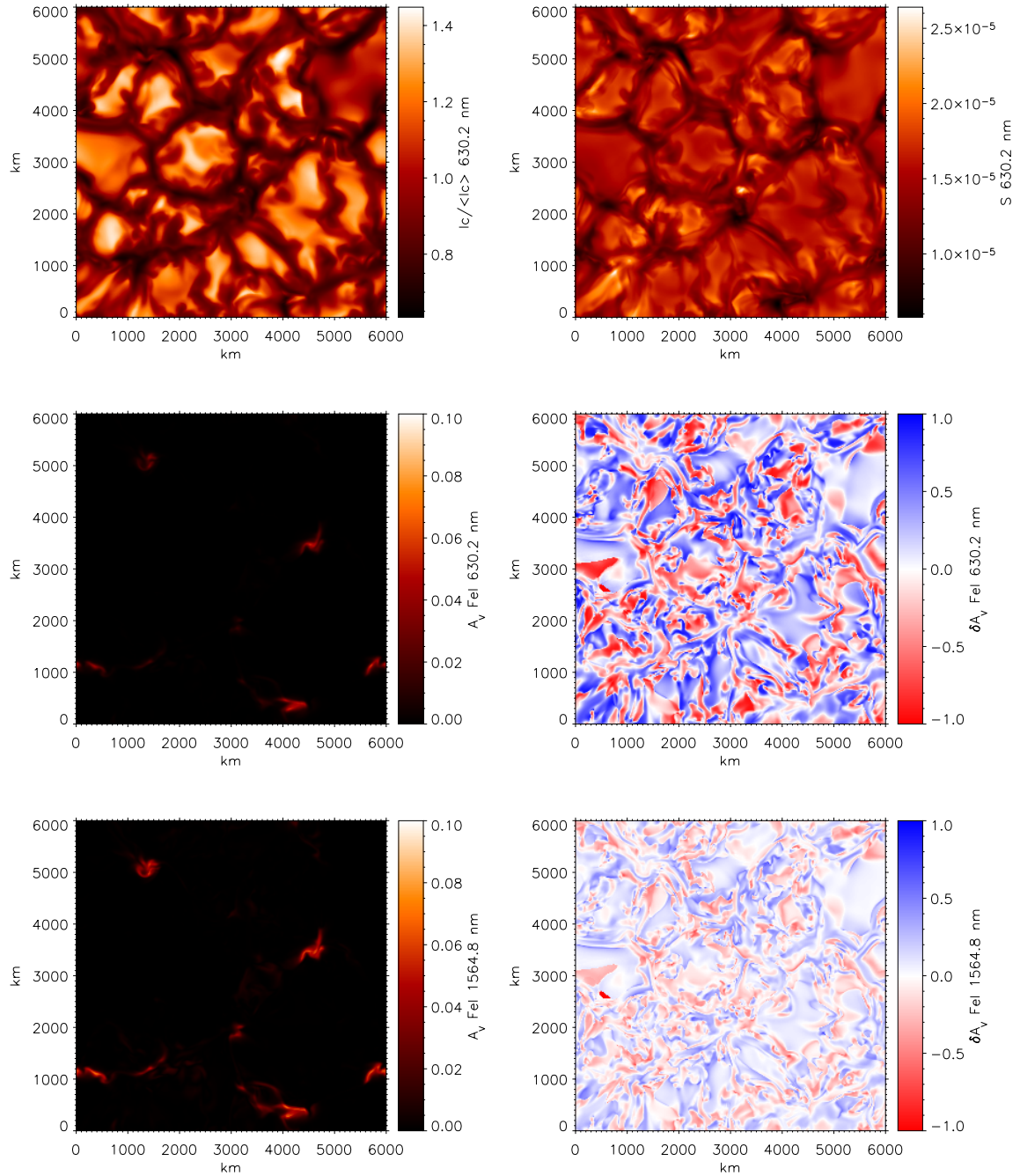


Figure 4.3: Continuum intensity, $I_c / \langle I_c \rangle$, integrated Stokes- I profile, the total Stokes- V area and the area asymmetry calculated for the 630.2 nm and 1564.8 nm Fe I lines for the snapshot from the 10 G average magnetic field simulation.

magnetic field map (upper right). The Doppler velocity shifts are calculated according to:

$$\Delta v = \frac{\lambda_0 - \lambda_c}{\lambda_0} \cdot c, \quad (4.4)$$

where c is the velocity of light, λ_0 is the wavelength of the line center in the rest frame, and λ_c is the center of gravity of the line, which is defined as the first moment of the profile:

$$\lambda_c = \frac{\int (I_c - I) \lambda d\lambda}{\int (I_c - I) d\lambda}, \quad (4.5)$$

where I_c is the continuum intensity and I is Stokes- I parameter dependences on the wavelength. The line widths are determined as the standard deviations of the profiles (square roots of the second moments):

$$\text{Line width} = \sqrt{\frac{\int (I_c - I) (\lambda - \lambda_c)^2 d\lambda}{\int (I_c - I) d\lambda}}. \quad (4.6)$$

The maps of the Doppler velocity shifts, shown in the middle panels of Fig. 4.4 and 4.5 indicate that the velocity field, as determined by analysis of the Stokes- I profiles is in good agreement with the original velocity field in the model, although the latter is plotted at $\tau_{500} = 1$, i.e. lower than the level to which λ_c (on average) pertains. The agreement is better for the quiet region represented by 10 G run since in this case the Stokes- I profiles are largely unaffected by the magnetic field. Negative values of the velocity correspond to downflows and are marked in red.

The maps of line width (lower panels) reflect the different magnetic and temperature sensitivities of the visible and infrared Fe I lines. In the case of 630.2 nm Fe I line, the magnetic sensitivity is lower. Thus, for the 630.2 nm line, although the width is enhanced close to the regions of magnetic fields, there is no line width enhancement in the regions themselves. As can be seen from a comparison of Figs. 4.4 and 4.5, the enhancements in line width are basically independent of the magnetic field and are probably related to the downflows in the intergranular lanes (Nesis et al. 1996, Solanki et al. 1996).

However, there is a clear correspondence between the magnetic field strength and the line width for the 1564.8 nm Fe I line, which is clearly due to the large Zeeman sensitivity of this line.

4.2.2 Two-dimensional cuts through the magnetic features

A two-dimensional vertical cut through the atmosphere, which is marked on the continuum image (upper left panel of Fig. 4.2) by the green line, is shown in Fig. 4.6. The individual panels of the figure show the distribution of temperature (upper left), gas pressure (upper right), magnetic field strength (lower left) and vertical velocity (lower right). The structure of the magnetic flux concentration, which looks very similar to a standard magnetic flux tube or flux sheet, is clearly visible in the images. The gas at the location of strong magnetic field is cooler and has reduced gas pressure (which is compensated by the magnetic pressure $|B|^2/8\pi$), so that in total pressure the magnetic region is hardly visible. There is also a strong downflow of about -3 km/s, mainly at the periphery of the

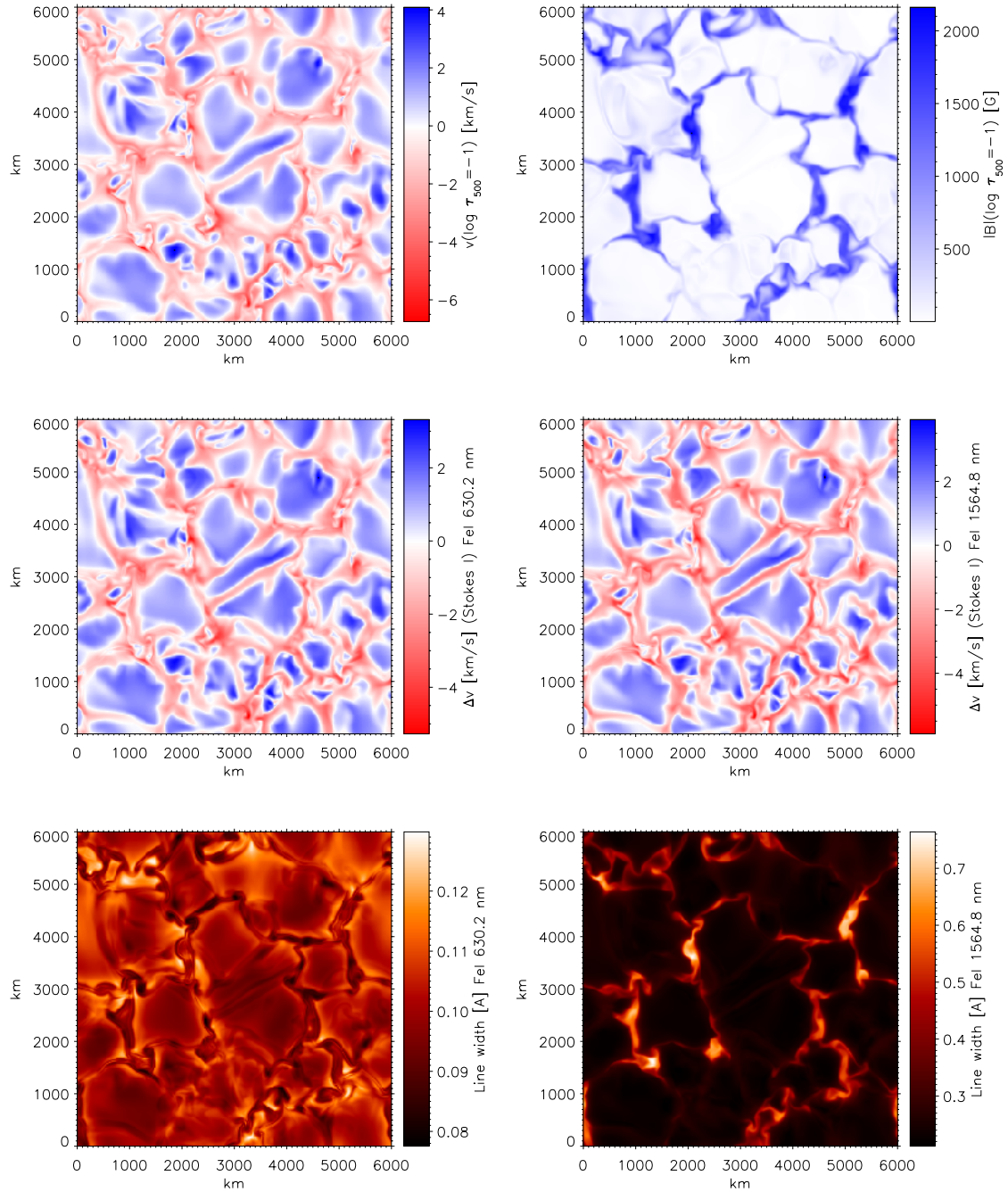


Figure 4.4: Vertical component of velocity, modulus of the magnetic field strength, Doppler shifts of the 630.2 nm and 1564.8 nm Fe I lines, and line widths of these lines, calculated for the snapshot from the 200 G average magnetic field simulation.

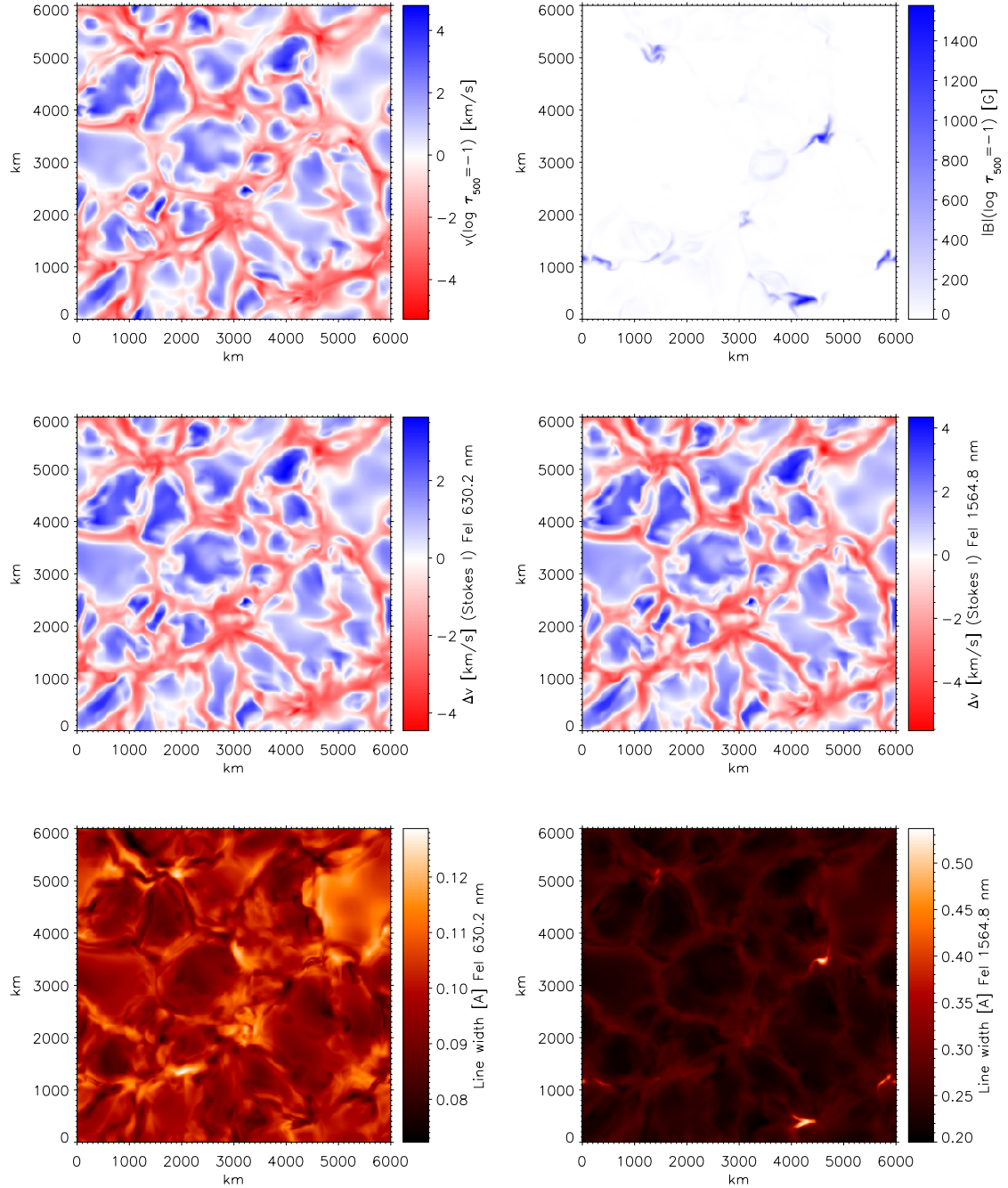


Figure 4.5: Vertical component of velocity, modulus of the magnetic field strength, Doppler shifts of the 630.2 nm and 1564.8 nm Fe I lines, and line widths of these lines, calculated for the snapshot taken the 10 G average magnetic field simulation.

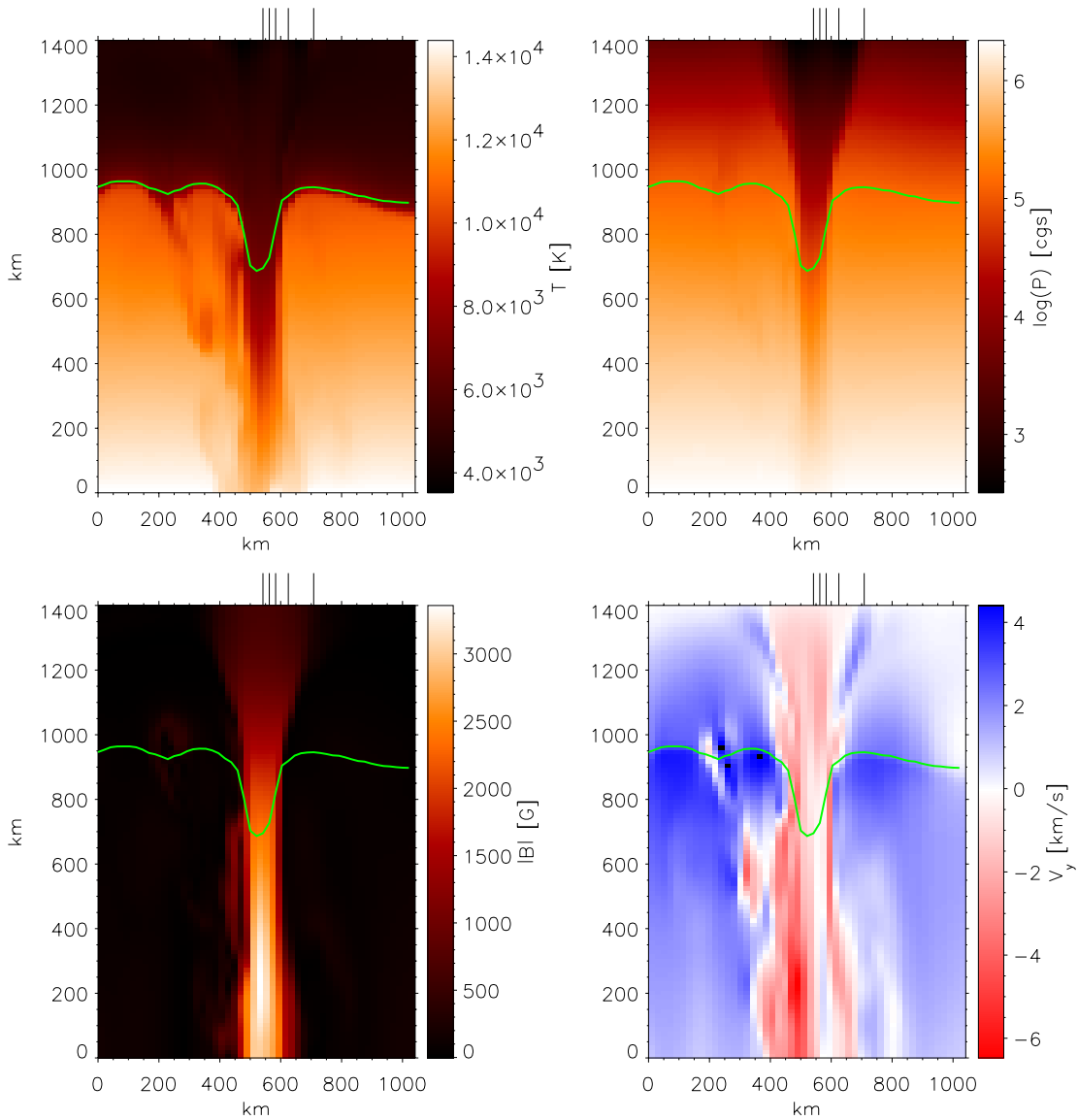


Figure 4.6: Temperature, pressure, modulus of the magnetic field strength and vertical velocity field for the 2D cut which is marked by green line on the continuum intensity image of Fig. 4.2. The green line on the images shows the $\log \tau = 0$ level. Negative values of the velocity (red color) correspond to a downflow. The pixels which are used for detailed profile analysis, shown in Fig. 4.7, are marked by lines on the top of the images.

magnetic flux concentration. The structure of the vertical velocity field is relatively complex, with strong upflows concentrated at the periphery of the flux tube and downflows inside it in the upper photosphere, i.e. the reverse of the signal seen in deeper layers.

The green line on the images shows the $\log \tau_{500} = 0$ level. One can see that the $\log \tau_{500} = 0$ surface is depressed by about 200 km in the regions of the strong magnetic field. This effect, which is mainly caused by the lower gas pressure in the magnetic regions is analogous to the Wilson depression in sunspots.

Stokes- I and $-V$ profiles emerging from the 2D cut shown in Fig. 4.6 are shown in

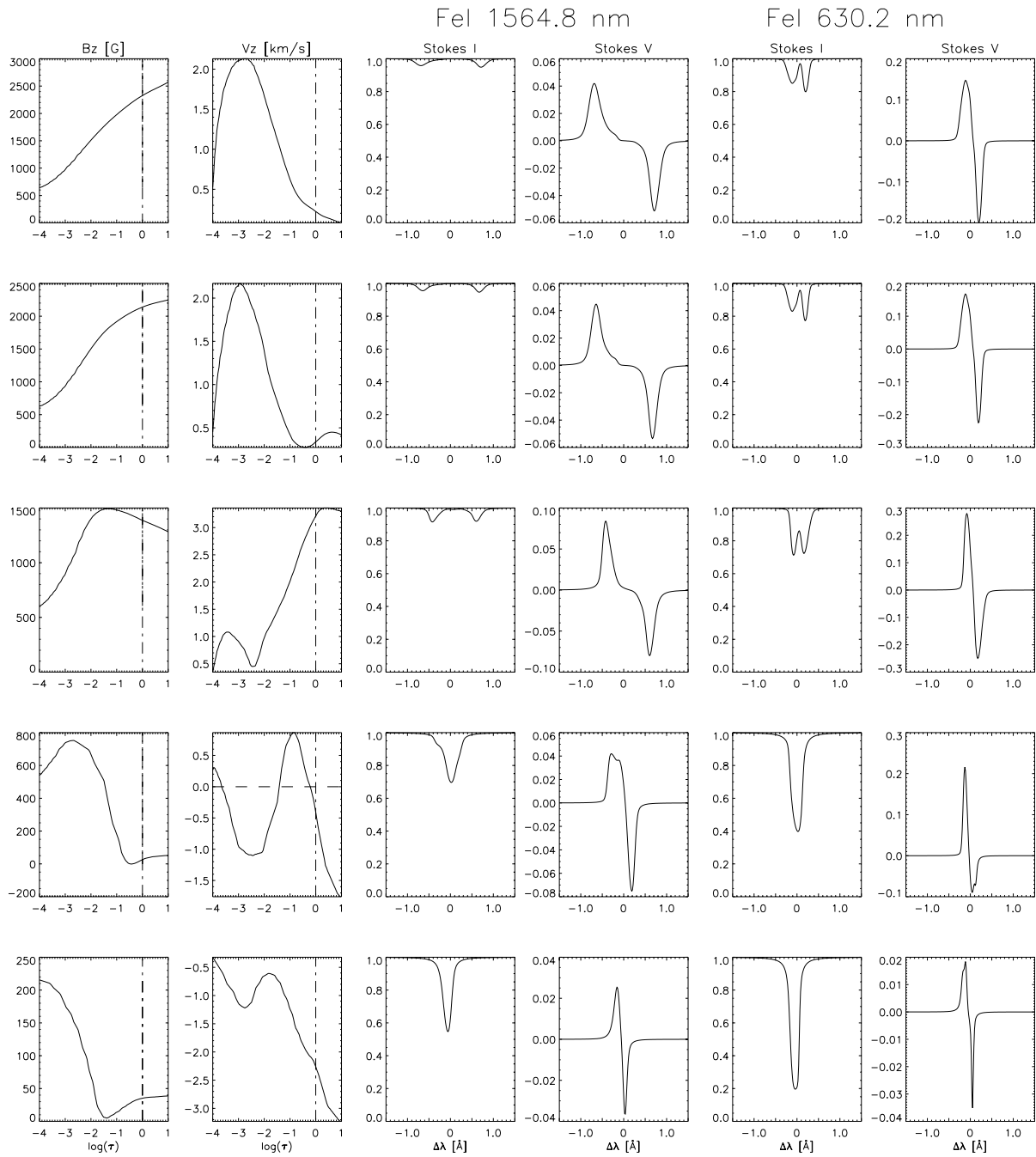


Figure 4.7: Stokes- I and - V profiles calculated for the iron lines for the pixels marked on the cut through the magnetic flux tube shown in Fig. 4.6. The corresponding magnetic field and velocity profiles on the optical depth scale are shown in the two left columns. The level $\log \tau = 0$ is marked by the dash-dotted line. The zero velocity level is marked by the dashed line.

Fig. 4.7. The first two columns give the vertical magnetic field strength and the vertical velocity profiles on the τ_{500} -scale. The next columns show the Stokes- I and $-V$ profiles for the 1564.8 nm and 630.2 nm Fe I lines. Negative values of the velocity correspond to downflows. The horizontal locations of the rays along which the profiles are calculated are marked in Fig. 4.6. The bottom row shows profiles formed far from the center of the flux tube, the top row profiles are coming from the central part. The location of the ray can easily be judged by considering the stratification of the magnetic field. Whereas the field strength decreases with height (or decreasing optical depth) at the center of the flux tube, the rays lying further out actually show a rapid increase of the field strength at increasingly greater heights, as the rays cut through the canopy of the expanding flux tube at even greater heights. The decreased field strength and increasing height of the flux tube boundary seen by the outer rays are reflected in the splittings (mainly for the IR line) and Stokes- V amplitudes (mainly visible line) of the two lines. The velocity profiles are more complex. At the center of the flux tube only weak flows (of both signs) are present, while next to it a strong upflow is present. With increasing distance to the center of the flux tube this is gradually converted into a downflow, mainly below the canopy. The plots show strongly weakened and split lines in the points with high magnetic field strength. The Stokes- V profiles have significant amplitude and area asymmetries at the edges of the magnetic flux tube (first two rows), where the gradients of the magnetic field strength and the velocity at the level of the line formation have an opposite signs.

The possibility of the formation of asymmetric unshifted Stokes- V profiles at the edges of magnetic flux tubes has been demonstrated by Grossmann-Doerth et al. (1988). They assumed a simple two-component atmosphere model: the upper component of the atmosphere has a magnetic field and no velocity, and the lower component of the atmosphere has a systematic vertical flow and no magnetic field. A vertically directed line of sight crosses both components. The structure of this model atmosphere is sketched in Fig. 4.8. The Stokes- V profile emerging along the line of sight will be asymmetric and have unshifted zero-crossing wavelength. The formation of the asymmetric Stokes- V profiles in an atmosphere with gradients of magnetic field and velocity has been studied by Illing et al. (1975). The sign of the asymmetry is determined by the sign of the product of the velocity and magnetic field gradients. Solanki and Pahlke (1988) showed that the blue wing of the Stokes- V profile is stronger than the red wing (positive area asymmetry) if the inequality

$$\frac{d|B_{\text{los}}|}{d\tau} \frac{dv_{\text{los}}}{d\tau} < 0 \quad (4.7)$$

holds. Here positive values of the velocity correspond to downflows. The scatterplot in Fig. 4.14 shows that the asymmetry in the models is in accordance with Eq. (4.7). The asymmetry is positive in regions where the velocity and the magnetic field gradients have opposite signs.

The amplitude and area asymmetries can be also defined by equations

$$\delta a = (a_b - a_r)/(a_b + a_r), \quad \delta A = (A_b - A_r)/(A_b + A_r), \quad (4.8)$$

where a_b and A_b are the amplitude and area of the blue wing of the Stokes- V profile, respectively, and a_r and A_r are the corresponding quantities of the red wing of the Stokes- V profile. The amplitude and area asymmetries of the lines plotted in Fig. 4.7 are given in Table 4.2. Clearly, Fe I 630.2 nm line shows larger asymmetry values than 1564.8 nm line.

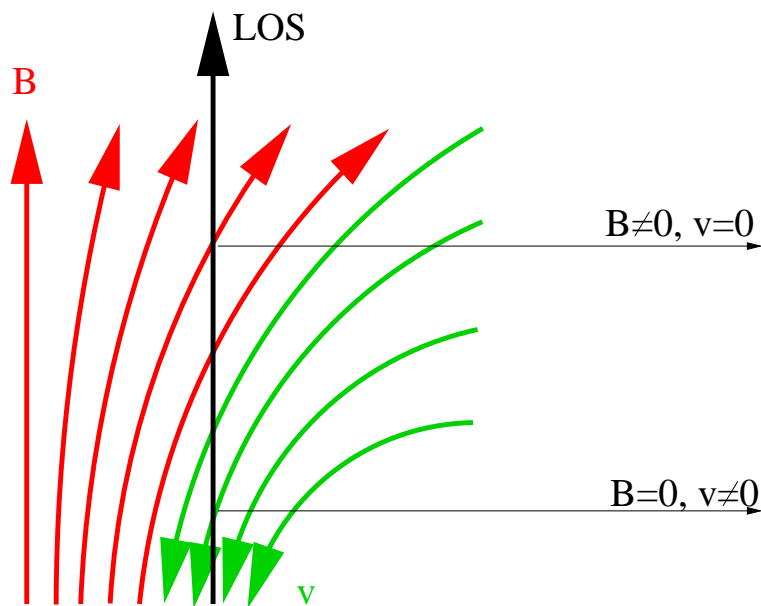


Figure 4.8: Sketch of the structure of a flux concentration which leads to asymmetric, unshifted Stokes- V profile. Red: magnetic field lines. Green: stream lines.

This is due to the combination of stronger saturation and weaker splitting (Grossmann-Doerth et al. 1989). Also, for this line the δA value is considerably larger in the outermost rays (a similar trend is also seen in the IR line, but less strongly). The asymmetry found here is less extreme than that obtained by Solanki (1989) on the basis of an idealized model with sharp gradients of the magnetic field and velocity.

	630.2 nm		1564.8 nm	
Point	δa	δA	δa	δA
1	-0.15	0.07	-0.10	0.02
2	-0.15	0.07	-0.08	0.01
3	0.06	-0.03	0.03	0.00
4	0.42	0.23	-0.28	0.03
5	-0.31	0.02	-0.18	0.00

Table 4.2: Stokes- V amplitude and area asymmetries of the 630.2 nm and 1564.8 nm Fe I lines for the cut shown in Fig. 4.7.

The cut through a thin magnetic feature is shown in Fig. 4.10. The cut is marked by the blue line in the continuum image (upper left) in Fig. 4.2. The asymmetry values for this cut are shown in Table 4.3.

4.2.3 Statistical comparison of the simulated profiles with the atmospheric parameters

The scatterplots of the line strength S against the modulus of the magnetic field strength are shown in Fig. 4.11. The averages over individual bins of width are given by the red

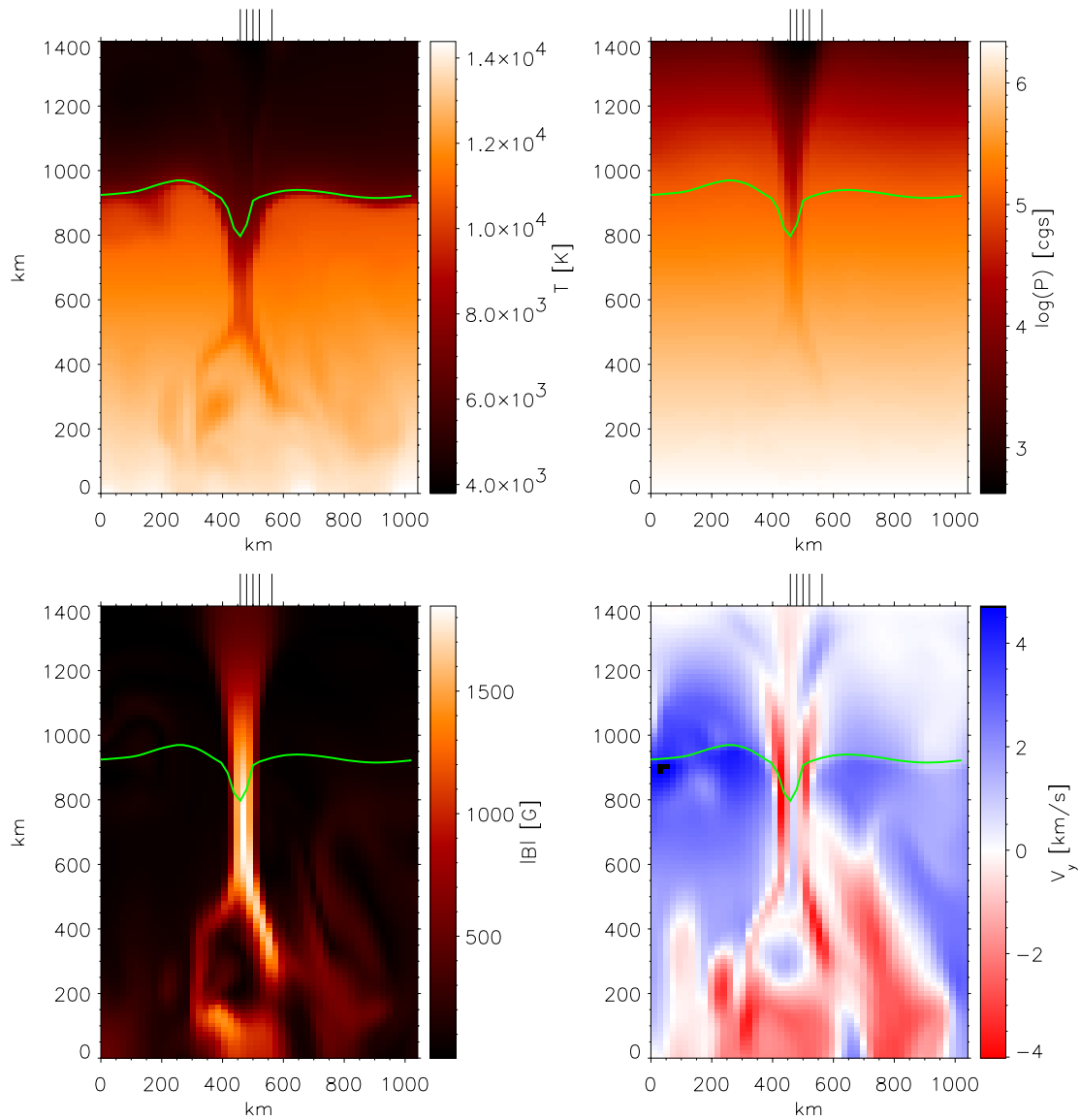


Figure 4.9: Temperature, pressure, modulus of the magnetic field strength and vertical velocity field for the 2D cut which is marked by blue line on the continuum intensity image of Fig. 4.2. The green line on the images shows the $\log \tau = 0$ level. Negative values of the velocity (red color) correspond to a downflow. The pixels which are used for detailed profile analysis, shown in Fig. 4.10, are marked by lines on the top of the images.

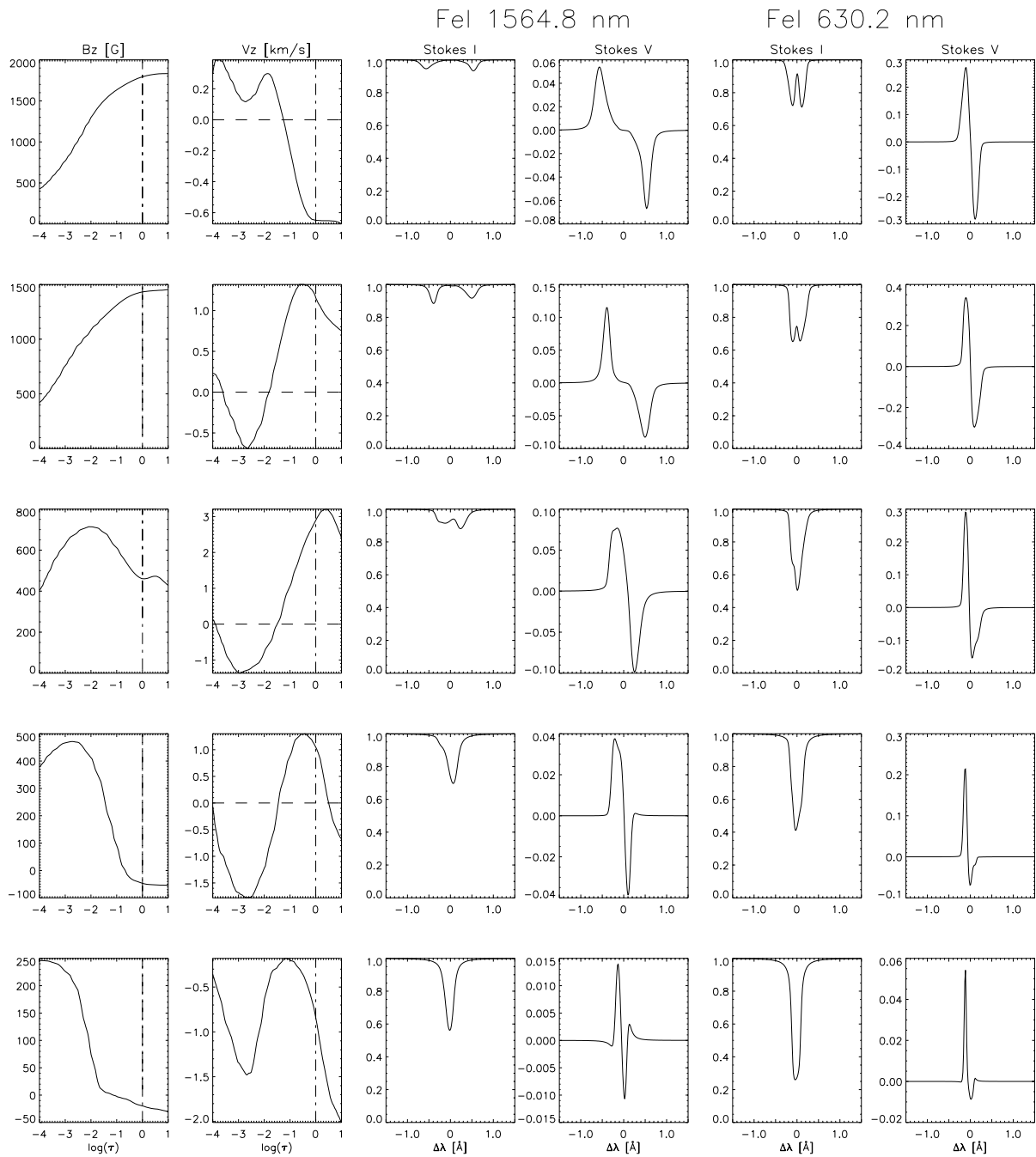


Figure 4.10: Stokes- I and - V profiles calculated for the iron lines for the pixels marked on the cut through the magnetic flux tube (Fig. 4.9). The corresponding magnetic field and velocity profiles on the optical depth scale are shown in the two left columns. The level $\log \tau = 0$ is marked by the dash-dotted line. The zero velocity level is marked by the dashed line.

	630.2 nm		1564.8 nm	
Point	δa	δA	δa	δA
1	-0.02	0.03	-0.11	0.01
2	0.06	-0.07	0.16	-0.03
3	0.31	0.05	-0.12	0.04
4	0.51	0.43	-0.02	0.33
5	0.72	0.59	0.13	0.27

Table 4.3: Stokes- V amplitude and area asymmetries of the 630.2 nm and 1564.8 nm Fe I lines for the cut, shown in Fig. 4.10.

line. The spectral lines become weaker with larger magnetic field strength. The dependence is almost linear, although for the 630.2 nm line there is an indication that the slope changes to a steeper decrease for strong magnetic fields. This is caused by the change of the thermodynamic regime in these regions. The lateral heating and partial evacuation of magnetic structures causes the abundance reduction of iron and thus decreases the absorption in the lines. The IR line exhibits a steeper relative decrease in S , implying that the IR line is more strongly weakened in spite of its higher excitation potential.

The scatterplots of the total Stokes- V area A versus the strength of the vertical component of magnetic field, shown in Fig. 4.12, illustrate the different magnetic sensitivities of the 630.2 nm and 1564.8 nm lines. The dependence of the total Stokes- V area of 630.2 nm line on the magnetic field is linear in the regions of weak magnetic fields $B_z < 1200$ G. The IR line saturates close to half this field strength. This line also exhibits much larger scatter of A values for intermediate field strengths. The hook-like structure visible for the both profiles can be ascribed to a temperature effect. In the hot regions with high magnetic field strength, the higher dissociation rates, lower density and smaller temperature gradients lead to the reduction of the absorption by iron and, thus, weakening of the amplitude of the spectral line. The more rapid decrease of A with B of the IR line agrees with the more rapid decrease seen in Fig. 4.11 for this line. These scatterplots also show that the infrared Fe I line is formed deeper than the visible line because the largest value of the net circular polarization for the infrared line (~ 800 G) is smaller than this value for the visible line.

The scatterplots of the normalized area asymmetry δA_V against the vertical magnetic field strength are shown in Fig. 4.13. The large scatter of the asymmetry values for low magnetic field strengths indicates that Stokes- V signals with small amplitudes associated with these magnetic fields, are rather asymmetric. For the very weak profiles, although both signs of δA_V are common, positive values dominate. Many of those very weak V profiles are associated with the upflowing parts of granules and many are due to fields strongly inclined to the vertical. Note that some of the weak profiles have δA values reaching 1, i.e. the model does produce single lobed profiles of the Fe I 630.2 nm line (but not of the IR line). According to the definition given by Eq. (4.3) δA_V is restricted to the range ± 1 , so that complex profiles, e.g. with 3 or more lobes, cannot be distinguished from normal profiles in this diagram. The average dependence of the asymmetry on the magnetic field strength is shown by the red line. There is no systematic area asymmetry in flux concentrations with the strong magnetic fields. In the regions of weaker magnetic

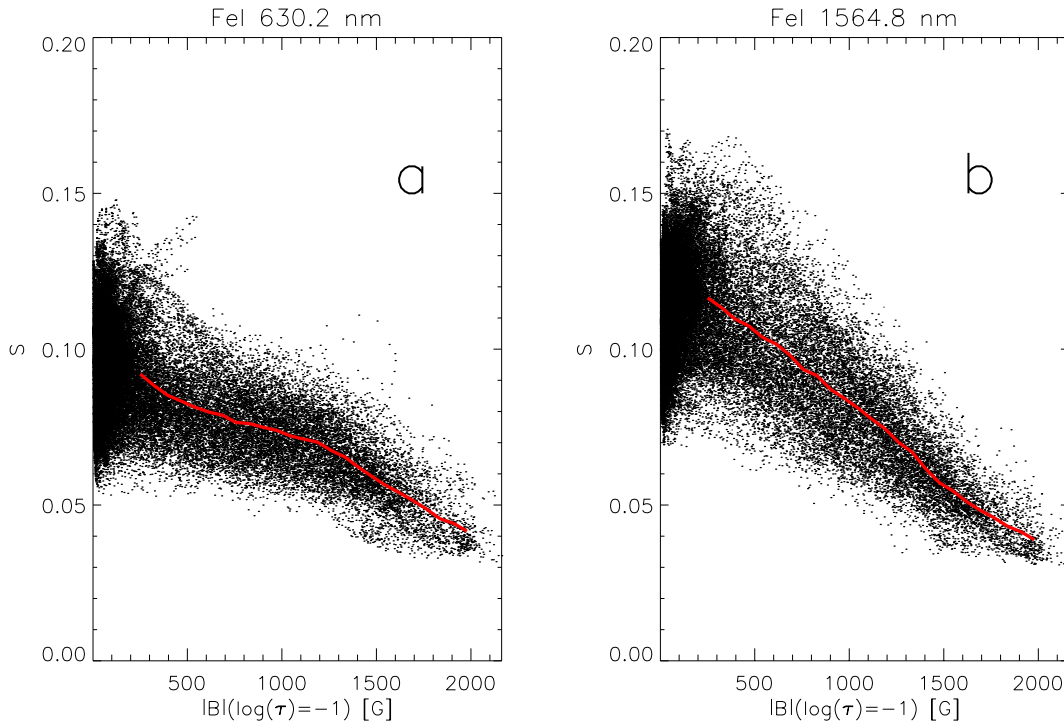


Figure 4.11: Scatterplots of the line strength versus the modulus of the magnetic field strength, calculated for the 630.2 nm (a) and 1564.8 nm (b) Fe I lines. The red lines show the averages.

fields ($B \sim 500$ G), which are mainly located near the edges of the magnetic flux tubes, the area asymmetry values are on average significantly positive.

The dependence of the normalized Stokes- V area asymmetry on the product of the quantities, representing the gradients of vertical magnetic field and the vertical component of velocity, $(v_{z,\tau_{500}=0.1} - v_{z,\tau_{500}=0.11}) \cdot (|B_z|_{\tau_{500}=0.1} - |B_z|_{\tau_{500}=0.11})$, plotted in Fig. 4.14, shows that the asymmetry grows with the growth of the product of gradients, in agreement with the expectation from Eq. (4.7). This supports the general theory for the production of δA_V (cf. Solanki (1993) and references therein). The relation shows some scatter since the line is formed over a range of heights while the gradient refers to a fixed optical depth.

The 1564.8 nm Fe I line is formed deeper in the atmosphere than the 630.2 nm line. Thus, the diagnostics using both lines can give information about the spatial structure and the depth dependence of the magnetic field in the solar photosphere. The scatterplot in Fig. 4.15 shows that the total Stokes- V areas of the 630.2 nm line and the 1564.8 nm line correlate, although there is considerable scatter. The average dependence (red curve in the figure) is roughly linear for weak magnetic fields. Also, the density of points is inhomogeneous on the scatterplot, suggesting the presence of different populations of points. The most significant population is located in the region higher than the average curve at the coordinates around (0.06,0.06) on the figure. In order to determine whether they really are different populations with distinct origins we compare the spatial distributions of these points with spatial features of the magnetic field in the atmosphere. The plots shown in Fig. 4.16 reveal a connection between the magnetic gradient and the location of points

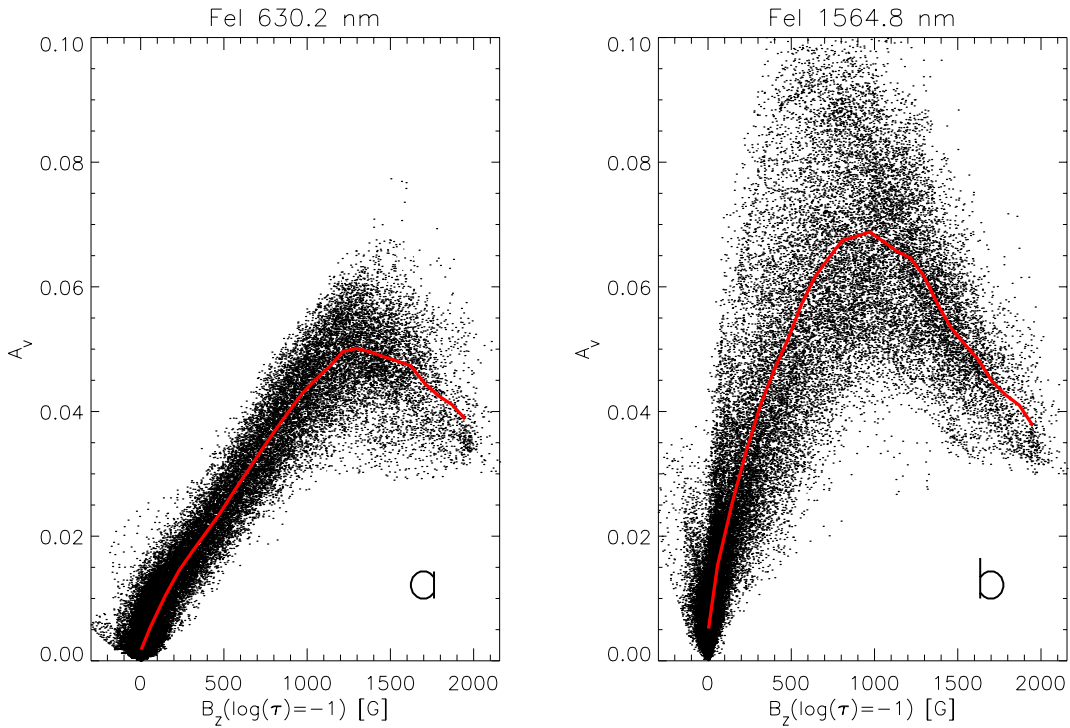


Figure 4.12: Scatterplots of the total Stokes- V area versus the strength of the vertical component of the magnetic field, calculated for the 630.2 nm (a) and 1564.8 nm (b) Fe I lines. The corresponding binned averages are shown by the red lines.

in the diagram shown in Fig. 4.15. In the upper panel of Fig. 4.16, the map of the gradient of the vertical magnetic field strength is shown. The gradient is calculated as a difference between the vertical magnetic field strengths at the $\tau_{500} = 0.1$ and the $\tau_{500} = 0.11$ levels. The gradient has positive values if the vertical magnetic field increases with depth. The image reflects the structure of the magnetic field in the magnetic flux concentrations, which expand upward. The structure is similar to the shown in Fig. 4.8. In the central regions of the flux tube, the magnetic field strength decreases with height owing to the horizontal pressure balance and the decreasing gas pressure. At the edge of the flux tube, the line of sight crosses the deeper region outside of the flux tube and the higher region inside, thus the magnetic field strength increases with height.

The observational consequences of this effect can be discussed using the lower part of Fig. 4.8. The red crosses on the scatterplot are formed in the red regions on the magnetic field gradient map. The blue crosses in the scatterplot can be divided in two populations. One population corresponds to the central regions of the magnetic flux tubes. The Stokes- V signals, corresponding to this population, are strong for both the visible and infrared lines. The second, smaller population is connected to the weakly magnetized granulation, and has weaker Stokes- V signals. Green points on the scatterplot mostly correspond to weakly magnetized granulation, show no strong vertical magnetic field gradient and have weak Stokes- V signals. There is also a small population of points in magnetic concentrations, which do not show strong gradients of vertical magnetic field. These points are marked by green.

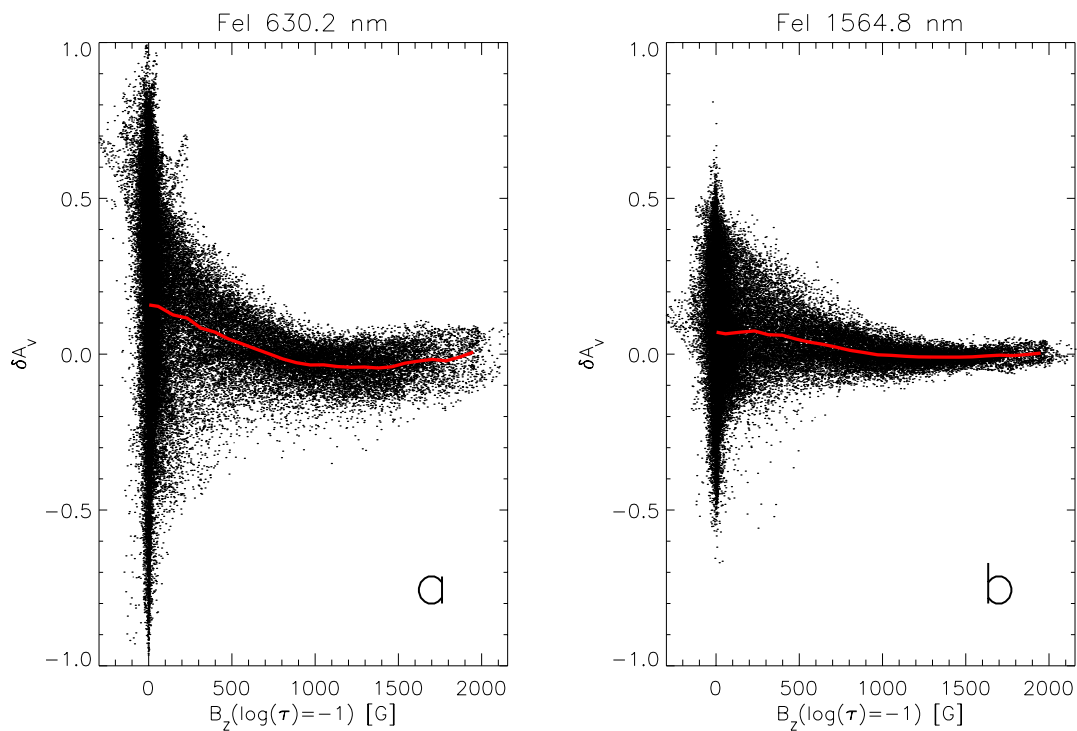


Figure 4.13: Scatterplots of the dependence of the normalized Stokes- V area asymmetry versus the strength of the vertical component of the magnetic field, calculated for the 630.2 nm (a) and 1564.8 nm (b) Fe I lines. The average dependences are shown by the red lines.

4.3 Comparison with observational data

In order to check the realism of the model calculations, we have compared the calculated Fe I lines with observational data. The average profiles emerging from the simulated atmospheres are compared with the observed spectrum of the quiet Sun (Delbouille et al. 1973). The spectra are shown in Fig. 4.17 and 4.18. The green lines on the spectra correspond to the spatially averaged profiles from the simulations. The agreement between the observed and the simulated infrared lines is very good for both the 200 G (Fig. 4.17) and 10 G (Fig. 4.18) simulations. Some discrepancy in the rest intensity between the average profiles of the 630.1 nm and 630.2 nm lines for the 10 G simulation is probably caused by the neglect of NLTE effects in the calculations. The possibility of such a discrepancy in the line depths of the 630.1 nm and 630.2 nm Fe I lines is shown by Shchukina and Trujillo Bueno (2001).

Synthetic slit spectra calculated for the slit marked by the vertical yellow line on the continuum image of the 200 G snapshot in Fig. 4.2, are shown in Figs. 4.19, 4.20, 4.21, 4.22. The Stokes- I spectra contain the information about the continuum intensity along the slit direction, while the V , Q and U profiles are normalized to the continuum intensity. The simulated slit crosses a large magnetic concentration between $x \sim 3000$ km and $x \sim 4000$ km. There is also a small concentration of magnetic flux at ~ 1800 km. The magnetic flux concentrations show a strong Stokes- V signal and split lines in the Stokes- I spectra at least for the more Zeeman sensitive lines. The largest splitting can be observed

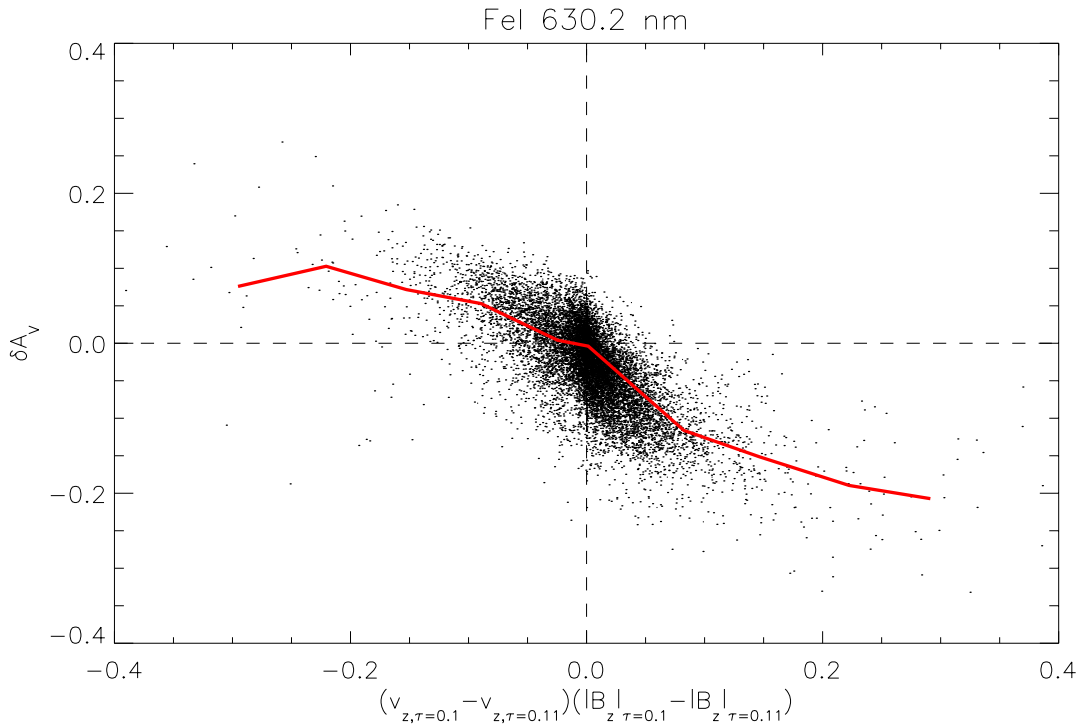


Figure 4.14: Scatterplot of the normalized Stokes- V area asymmetry versus the product of the quantities, representing the gradients of the strength of the modulus of the vertical component of the magnetic field and the vertical component of velocity, calculated for the 630.2 nm Fe I line.

for the 1564.8 nm Fe I line. The intrinsic pattern of the displacement of the line center in the spectra is mainly due to the granulation in Stokes- I . However, Stokes- V (and Q and U) also show a complex pattern of Doppler shifts within the larger magnetic features, with both blue and red shifts being present. Together with the structure in the Zeeman splitting of 1564.8 nm line this points to the presence of significant internal structure along the long axis of a magnetic flux sheet. Note that some of the variation seen in Stokes- V of Figs. 4.19-4.22 may be due to the fact that the flux sheet is bent and the straight slit samples central and peripheral regions of it at different locations. Stokes- Q and $-U$ parameters show almost no strong signals meaning that there is no strong horizontal magnetic fields in the model. The granules show no magnetic field and a blueshift.

The magnetogram image calculated for the 630.2 nm Fe I line for the 200 G average magnetic field snapshot is shown in Fig. 4.23. The magnetogram intensity is defined as

$$M = \int V(\lambda)F(\lambda)d\lambda, \quad (4.9)$$

where $V(\lambda)$ is Stokes- V profile, and $F(\lambda)$ is the magnetograph filter function. The filter function is assumed to be Gaussian. The filter center is shifted by 0.12\AA from the unshifted line center at 630.25 nm towards the red side. The FWHM of the filter equals to 0.04\AA . The scatterplot of the magnetogram intensity M versus the magnetic field strength at the optical depth level $\log \tau_{500} = -1$ is shown in the lower part of Fig. 4.23. The scatterplot shows almost linear dependence of the magnetogram intensity on the magnetic

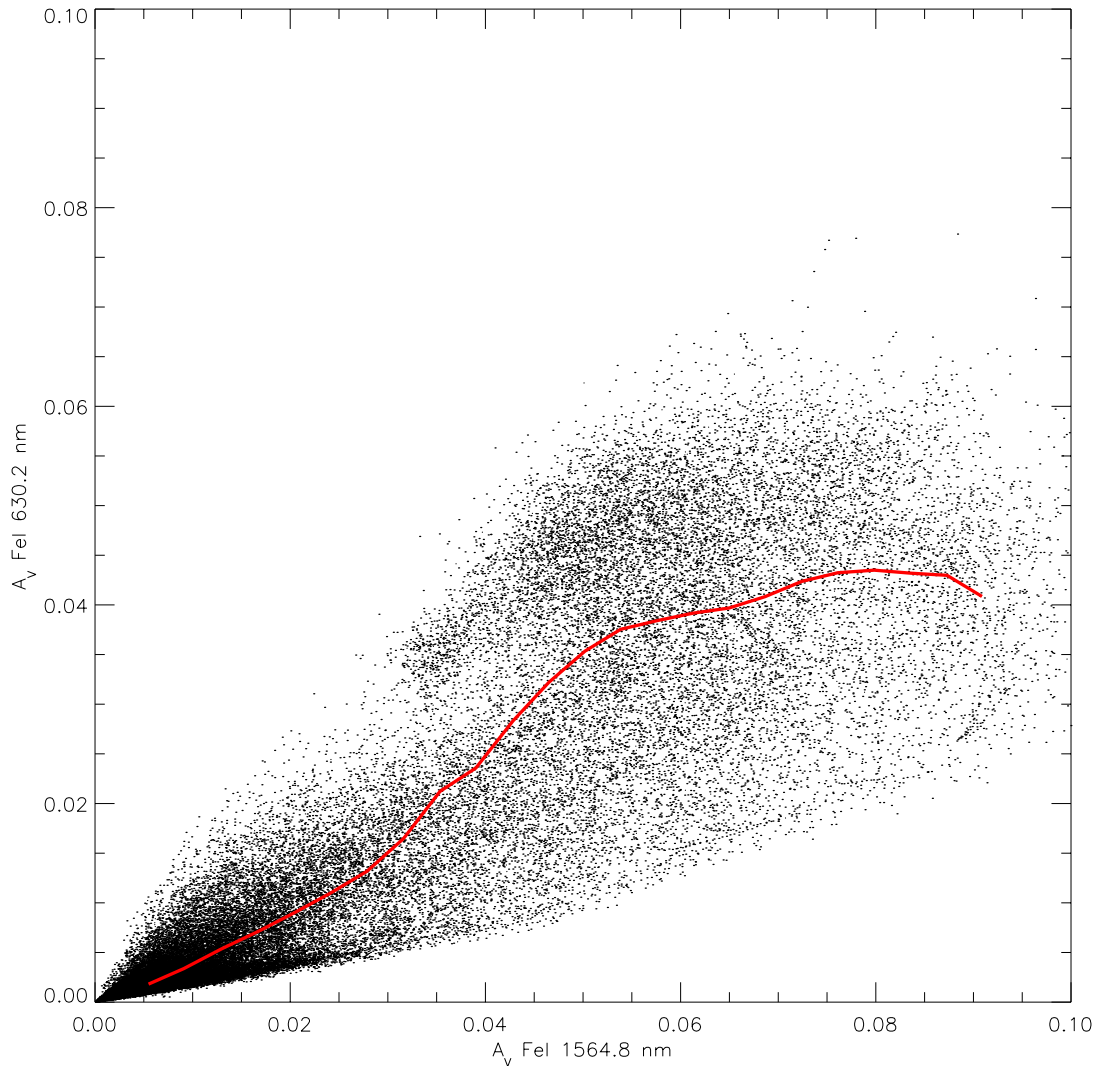


Figure 4.15: Scatter plot of the total Stokes- V areas of the 630.2 nm Fe I line versus the same quantity for the 1564.8 nm Fe I line.

field strength.

4.4 Conclusions

In this chapter I have presented the radiative diagnostics of realistic 3D MHD models, based on the synthesis of four neutral iron lines at 630.1 nm, 630.2 nm, 1564.8 nm and 1565.2 nm. All these lines are sensitive to the magnetic field through the Zeeman effect, and thus provide a direct diagnostics of the magnetic field in the simulated atmosphere. Various effects connected to the spatial distribution of the magnetic field, the velocity distribution and its gradient, the magnetic field strength and its gradient in the regions of Fe I line formation are discussed. These effects have observational consequences, which still have to be analyzed. Some comparisons of the calculated Stokes profiles with observa-

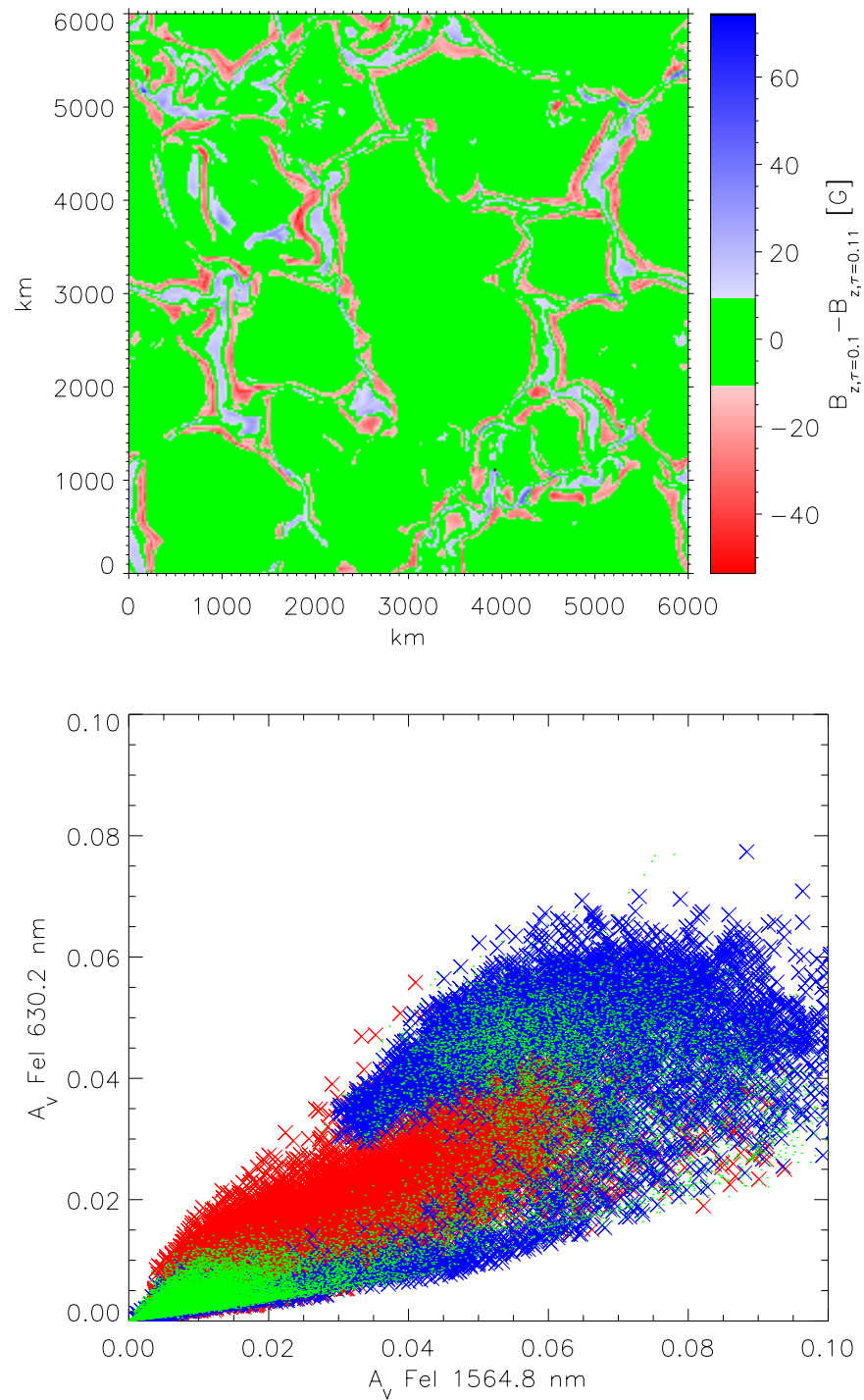


Figure 4.16: Upper panel: image of the quantity $(B_{z,\tau_{500}=0.1} - B_{z,\tau_{500}=0.11})$, representing the gradient of the vertical magnetic field strength. Lower panel: scatter plot of the total Stokes- V areas of the 630.2 nm Fe I line versus the same quantity for the 1564.8 nm Fe I line. The red, blue and green pixels on the upper panel correspond to the red and blue crosses and green points, respectively, on the scatter plot.

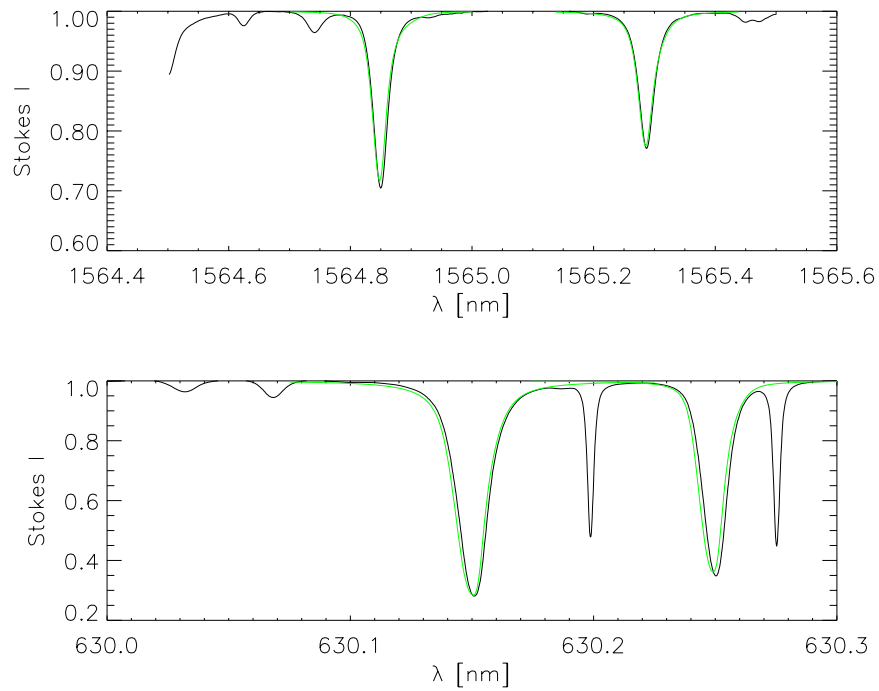


Figure 4.17: Comparison between the averaged simulated Fe I profiles for the 200 G run (green lines) and the observed profiles.

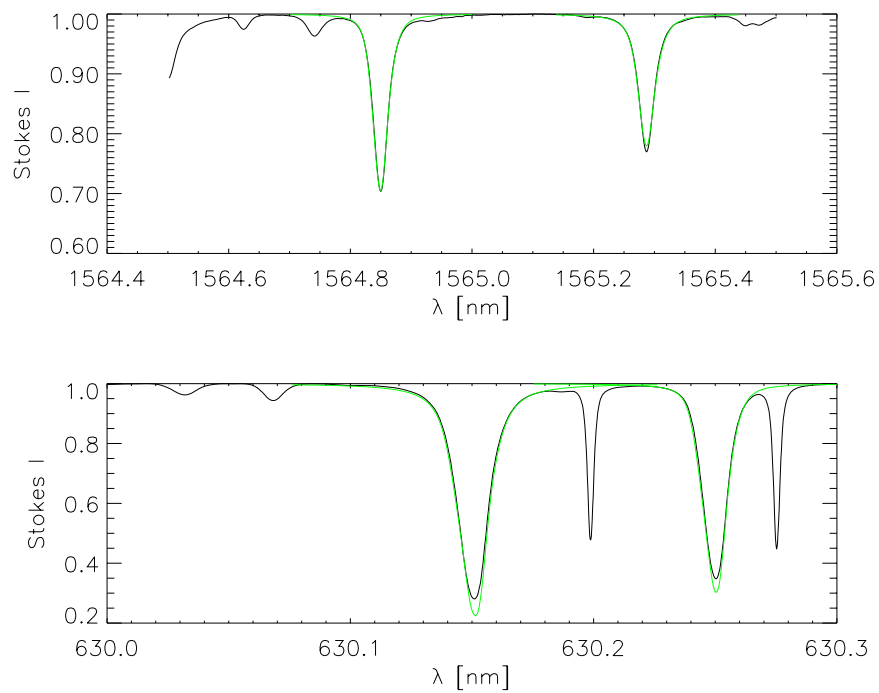


Figure 4.18: Comparison between the averaged simulated Fe I profiles for the 10 G run (green lines) and the observed profiles.

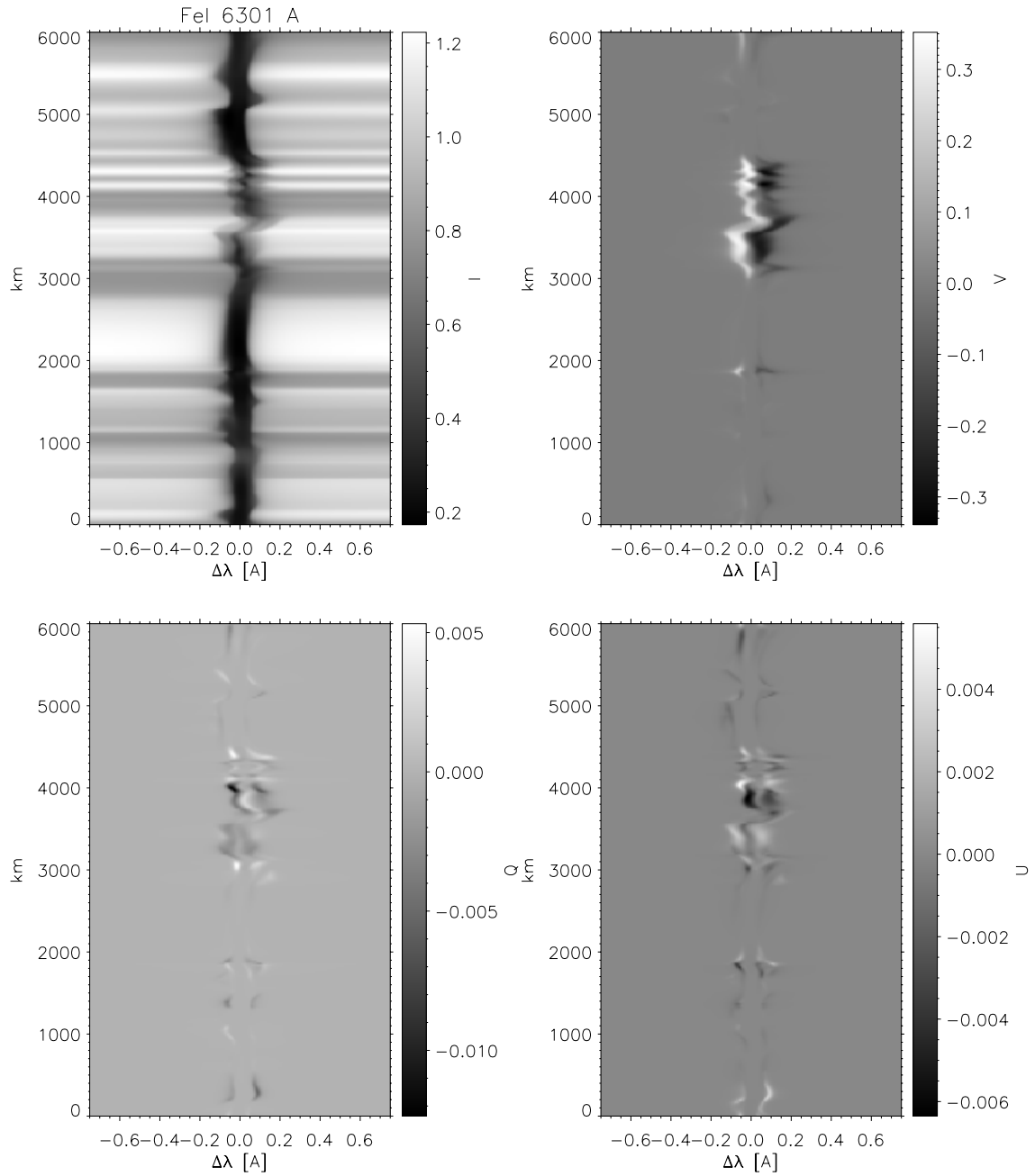


Figure 4.19: Simulated slit spectra, calculated for the 630.1 nm Fe I line. The position of the slit which is used for the calculation is indicated in Fig. 4.2. Upper left - Stokes-I, upper right - Stokes-V/I, lower left - Stokes-Q/I, lower right - Stokes-U/I.

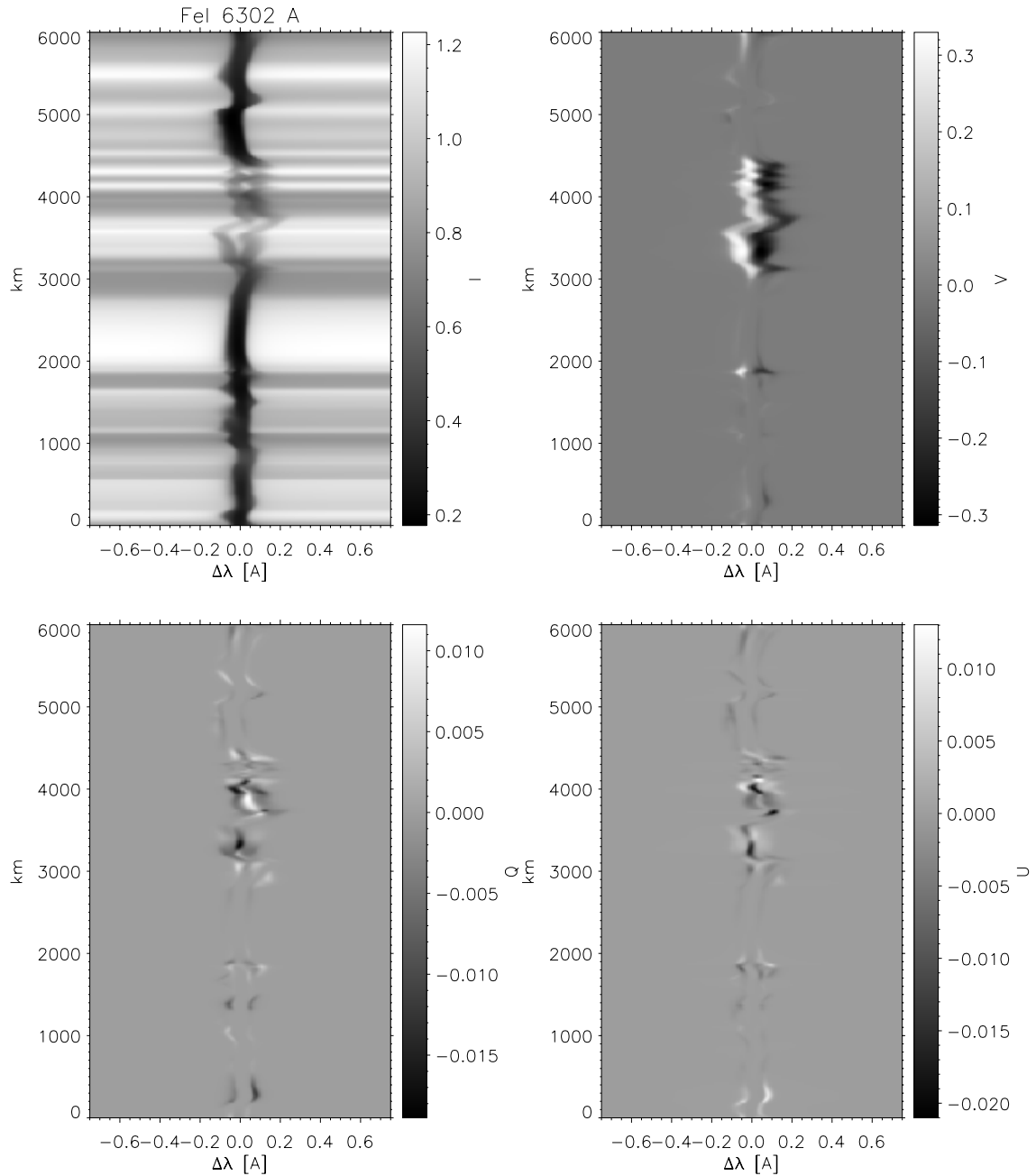


Figure 4.20: Simulated slit spectra, calculated for the 630.2 nm Fe I line. The position of the slit which is used for the calculation is shown in Fig. 4.2. Upper left - Stokes- I , upper right - Stokes- V/I , lower left - Stokes- Q/I , lower right - Stokes- U/I .

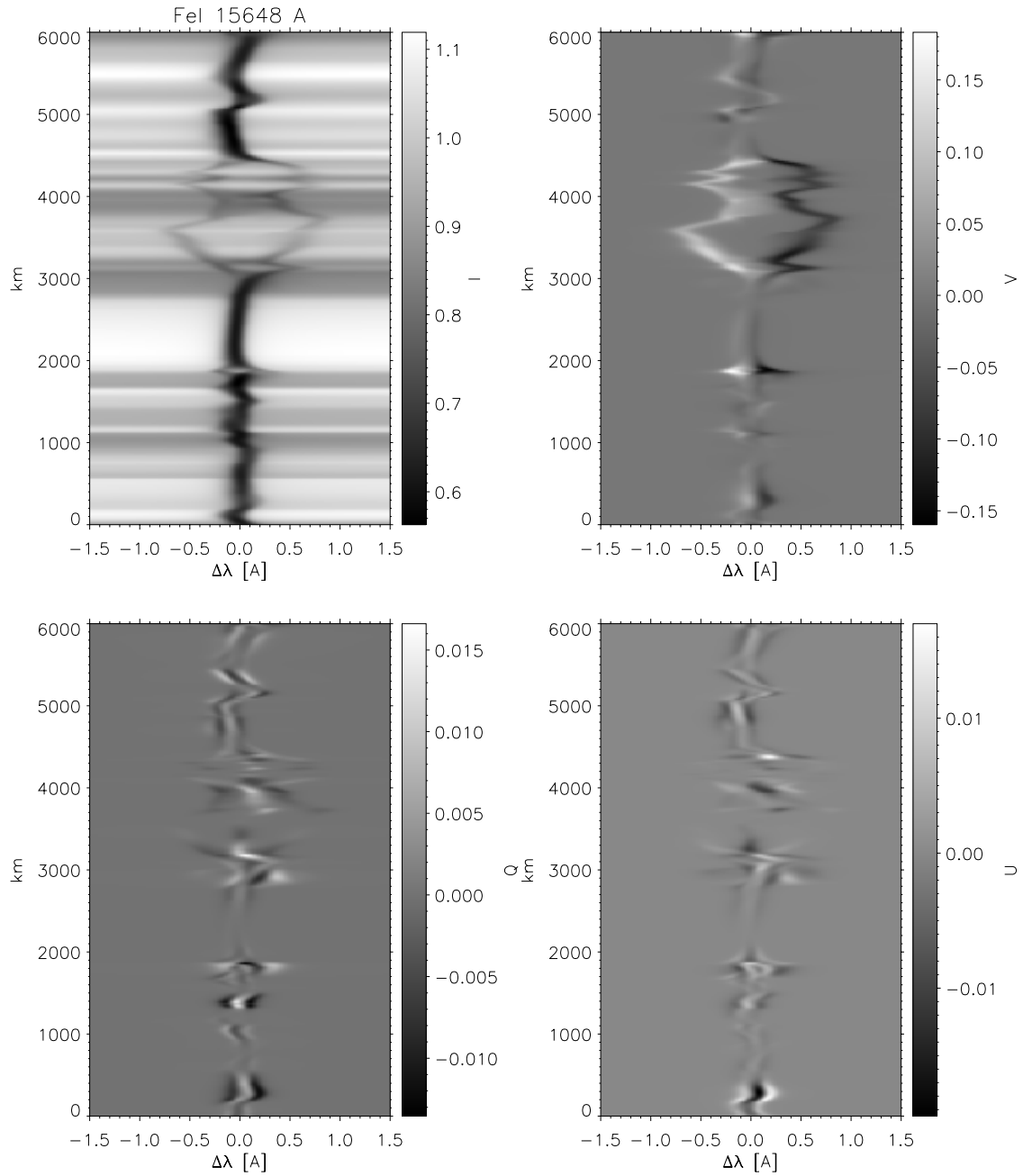


Figure 4.21: Simulated slit spectra, calculated for the 1564.8 nm Fe I line. The position of the slit which is used for the calculation is shown in Fig. 4.2. Upper left - Stokes- I , upper right - Stokes- V/I , lower left - Stokes- Q/I , lower right - Stokes- U/I .

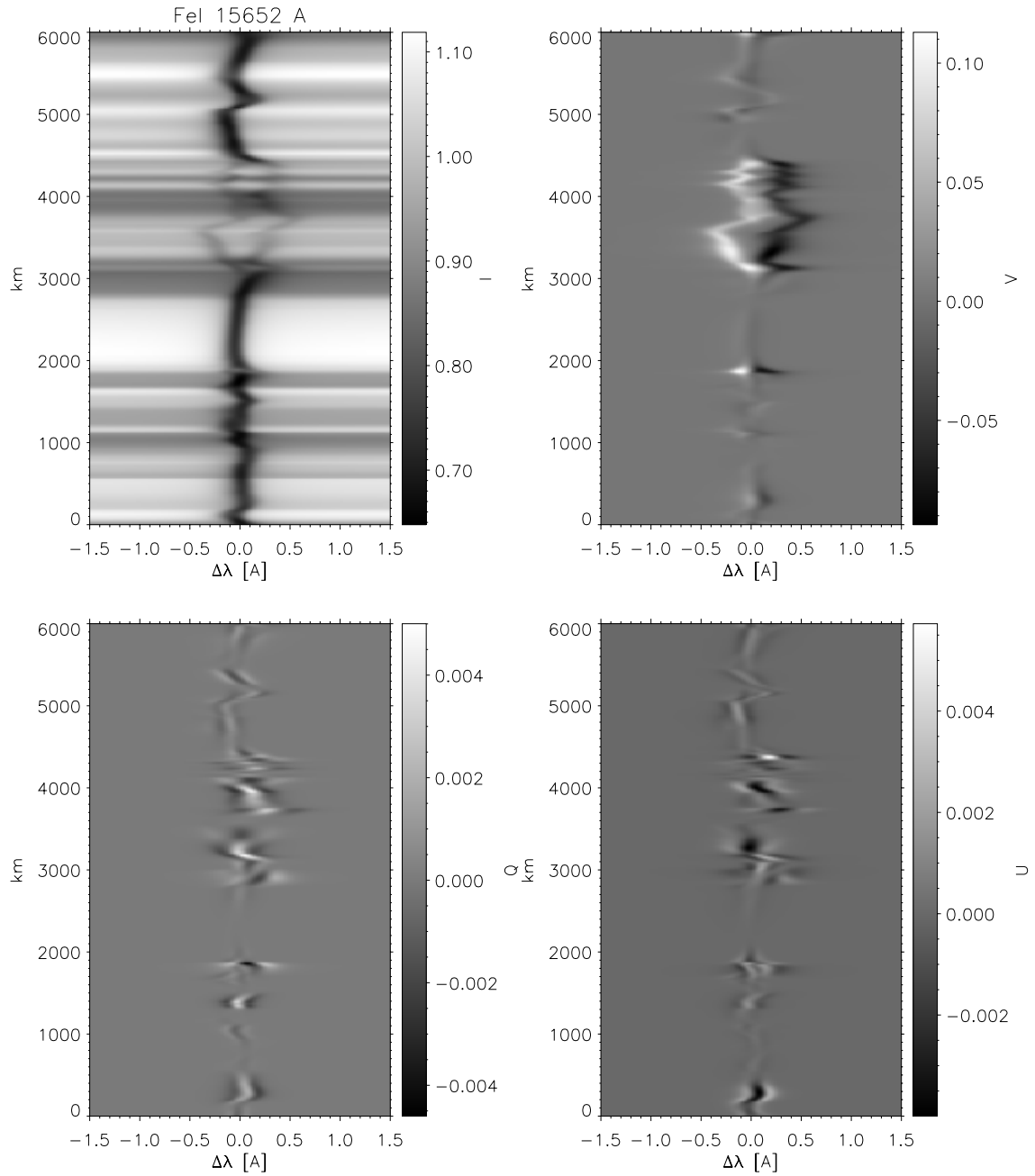


Figure 4.22: Simulated slit spectra, calculated for the 1565.2 nm Fe I line. The position of the slit which is used for the calculation is shown in Fig. 4.2. Upper left - Stokes- I , upper right - Stokes- V/I , lower left - Stokes- Q/I , lower right - Stokes- U/I .

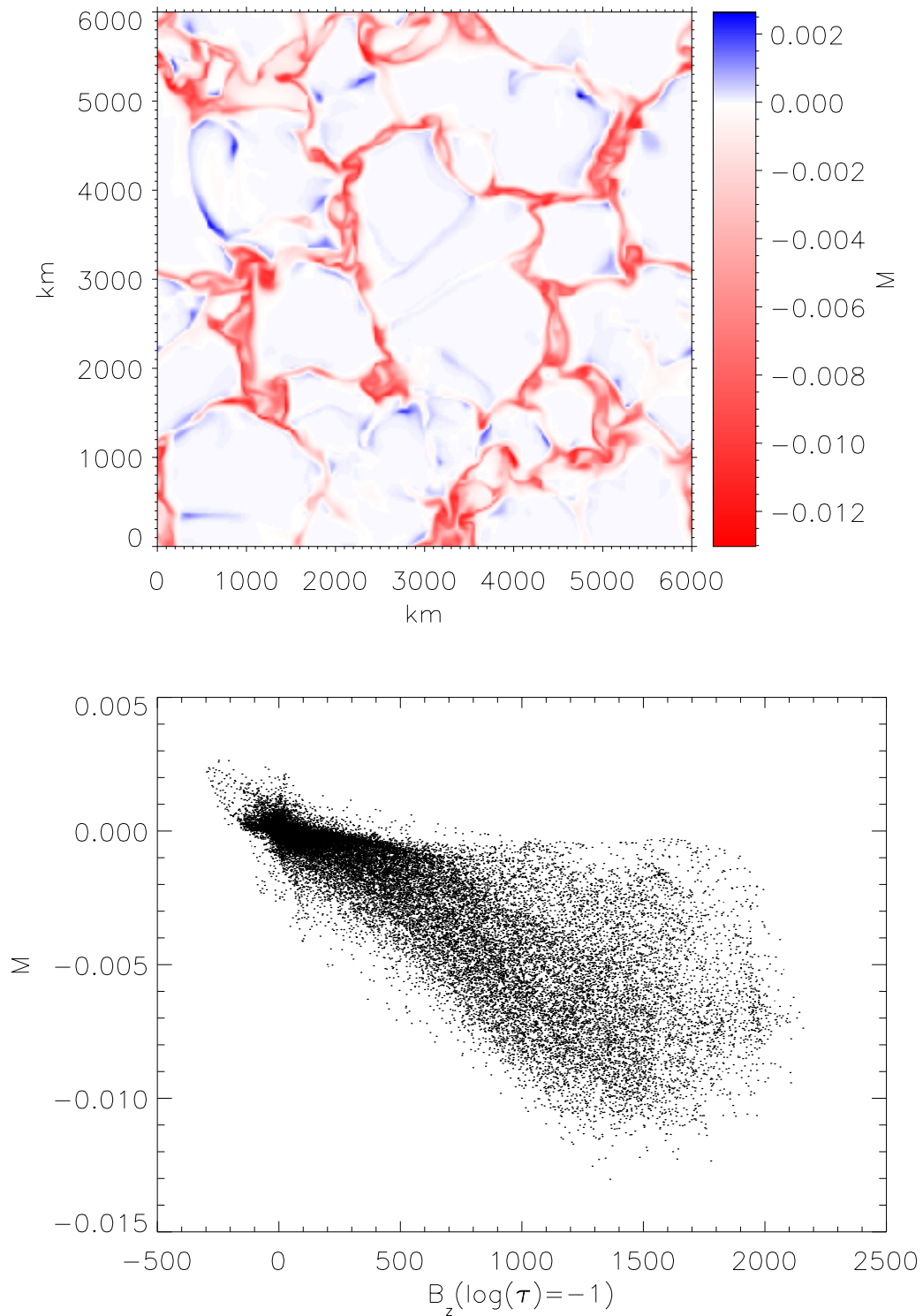


Figure 4.23: Upper part: magnetogram calculated for the 630.2 nm Fe I line for the 200 G average magnetic field snapshot. The Gaussian filter center is located at 0.12\AA to the red side from the unshifted line center. The FWHM of the filter equals to 0.04\AA . Lower part: scatterplot of the magnetogram intensity vs. vertical magnetic field strength at the level $\log \tau_{500} = -1$.

tional data have already been carried out. The average profiles emerging from the simulated atmosphere have been compared with the spectral atlas data (Delbouille et al. 1973). A reasonable agreement with the observational spectrum is obtained. The simulated slit and magnetogram images can be directly compared with polarimetric observations in a statistical sense.

5 G Band simulations

In this chapter, I discuss the simulations of the solar emergent spectrum in the G-band spectral range. First section of the chapter describes the properties of the G-band spectral range and the simulation setup. The physical background of the brightenings in G Band (the G-band bright points) and their connection to the magnetic field are presented in second section. The possibilities of the direct measurements of the magnetic field strength in the G-band bright points through the Zeeman polarimetry of the CH lines are discussed in third section. The comparison with the observational data is given in fourth section.

5.1 G Band simulations

Images of the solar surface layers taken in Fraunhofer's G band, a spectral region in the wavelength range 429.5-431.5 nm, which is populated by many spectral lines of the CH molecule, show bright features in the intergranular downflow regions, the so-called G-band bright points (Muller and Roudier 1984, Muller 1985, Berger and Title 1996, Rutten et al. 2001, Langhans et al. 2002). The G-band bright points are believed to correspond to the locations of the magnetic flux concentrations and thus are often used as "proxies" for small-scale magnetic elements (Berger et al. 1995, 1998, van Ballegoijen et al. 1998, De Pontieu 2002).

Realistic simulations of the G-band spectral range have been done based on the results of the MURaM code, described in Chapter 2 and the line calculation code, described in Chapter 3. The calculations of the Stokes parameters for atomic and molecular spectral lines has been done under Local Thermodynamic Equilibrium (LTE) assumption. In the case of CH lines, LTE is generally considered valid since the photodissociation of the CH molecule through bound levels of excited states is negligible in the solar atmosphere (Sánchez Almeida et al. 2001), the ionization energy of carbon is high and it remains primarily neutral in the solar atmosphere, so there are no effects of overionization as they may occur for molecules with metal compounds. Furthermore, there is no scattering polarization observed in CH lines within the G band at the solar limb in quiet regions, indicating that the line formation is controlled by collisions rather than radiative processes (Gandorfer 2002).

The molecular and atomic line data table (see Appendix A) which has been used for our G-band calculations consists of 241 CH lines and 87 atomic lines, mainly from neutral iron. The G-band spectrum emerging along vertical rays is calculated for each of the 288×288 pixels corresponding to the simulation grid. The calculated G-band spectra have 2055 frequency points covering the wavelength range from 429.5 nm to 431.5 nm. In order to obtain the G-band brightness, we multiply the spectra by a filter function

centered at 430.5 nm with FWHM of 1.2 nm, similar to the characteristics of filters used for observations, and integrate over the G-band wavelength range.

The spatially averaged G-band spectra (Stokes I and V) calculated for a snapshots from the runs with 10 G and 200 G average vertical field are shown in Figs. 5.1 and 5.2. The dashed lines indicate the filter function used for calculating the integrated G-band intensity. The thick solid lines show the average observed spectrum of quiet Sun (Delbouille et al. 1973). Atomic and CH lines are marked by small vertical dashes at the top and bottom of the Stokes- I plot, respectively. Whereas the Stokes- I spectrum is strongly affected by the molecular band, the Stokes- V spectrum is dominated by atomic lines, which are more sensitive to the magnetic field. The effective Landé factors of the CH lines are mostly of the order of 0.1-0.2 (Berdyugina and Solanki 2002)¹. There is no strong response of the molecular lines to the magnetic field, so that we do not have a direct influence of the magnetic field on the integrated G-band intensity.

Fig. 5.3 shows the G-band brightness distributions (upper panels) together with maps of the absolute field strength (lower panels) for the two simulation snapshots of quiet and active regions, corresponding to 10 G (right panels) and 200 G (left panels) average vertical magnetic field, respectively. One can see strong local brightenings up to $I_G/\langle I_G \rangle = 2.2$ corresponding to the regions of concentrated magnetic field. On the corresponding continuum intensity image (Fig. 2.7) the same brightenings have a relative brightness of about 1.7. The close visual correspondence of bright structures in the G band and strong magnetic field regions in both cases is not so clear in the scatter plots of G-band brightness vs. magnetic field strength shown in Fig. 5.4. For $B > 500$ G, the G-band brightness indeed increases rapidly with B (a roughly quadratic dependence seems indicated). However, there are also magnetic features with negative G-band contrast ($I_G/\langle I_G \rangle < 1$). In the 200-G run, this applies to about 30% of the points with $B > 1000$ G field. At small B , we also see a broad range of brightness, corresponding to bright granules and dark intergranular lanes. In the 10-G run, the brightest features are actually associated with granules, where magnetic field is weak. In the image, granules and magnetic elements are easily distinguished by their different sizes and shapes. This information is, of course, lost in the scatter plots. The situation is clearer when we consider only regions harbouring downflowing gas. Almost all (98%) of the points in downflow regions with $I_G/\langle I_G \rangle > 1.5$ are associated with strong magnetic field, $|B| > 1000$ G.

Scatterplots of G-band brightness versus continuum intensity at 430 nm for both runs are shown in Fig. 5.6. The separation of the image pixels in two components with a different slope of I_G vs. I_C is very similar to the observations of Berger et al. (1998) (see their Fig. 3). The component with larger G-band intensity for the same continuum intensity (indicated in green) corresponds to points with strong vertical magnetic field ($|B| > 500$ G), while the other component corresponds to weakly magnetized granules. Fig. 5.6 also shows that although 30%-50% of the strong magnetic fields can be recognized, many points are indistinguishable from points associated with weak fields.

¹The effective Landé factors in this paper are a factor of 2 too large, as pointed out by Landi degl'Innocenti. The correct values have been used for Stokes profile calculations in STOPRO.

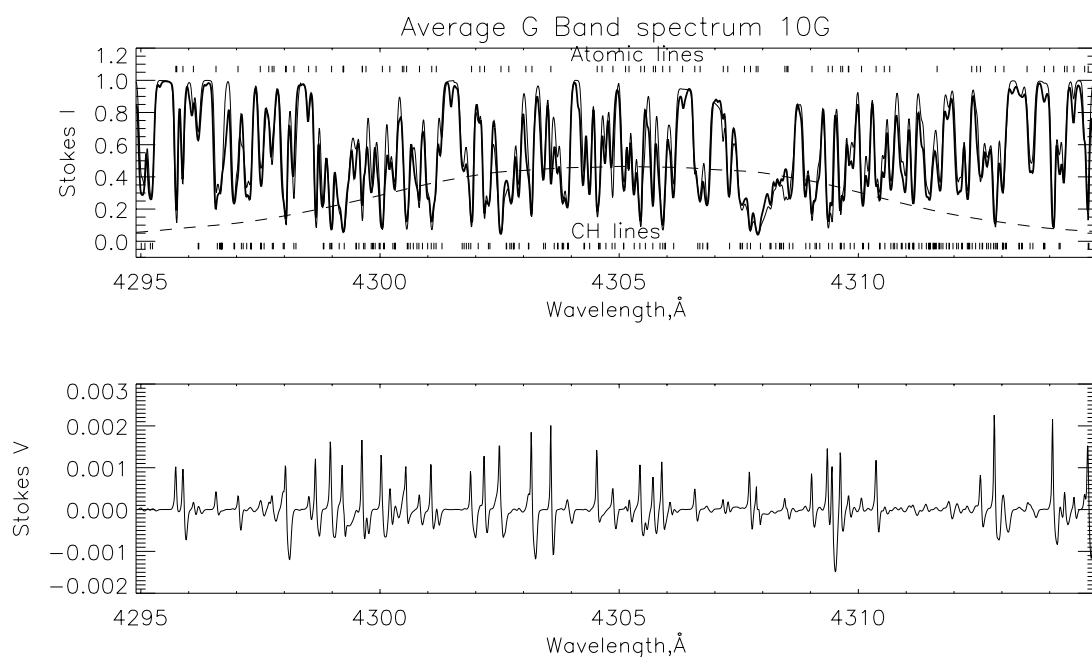


Figure 5.1: Spatially averaged spectra of Stokes I (top) and Stokes V (bottom) calculated for a snapshot from the run with 10 G average vertical magnetic field. Atomic and molecular lines are indicated on the Stokes- I plot. The dashed line shows the shape of the filter function which is used for calculating the G-band intensity. The thick line shows the observed spectrum of quiet region of the Sun (Delbouille et al. 1973).

5.2 Why are magnetic bright points bright?

The G-band spectral range is dominated by lines of the CH molecule and its integrated brightness is thus dependent on the strengths of those lines. The mechanism for the enhancement of G-band brightness in magnetic flux concentrations can be revealed by studying the dependence of the CH molecule concentration on the atmospheric parameters within and without magnetic flux concentrations, respectively.

A map of the number density of CH molecules at the optical depth level $\log \tau = -1$, which roughly corresponds to the level of CH line formation, is shown in Fig. 5.7. For the 200-G case comparison with the left side of Fig. 5.3 shows that there is a strong (more than one order of magnitude) decrease of the CH molecule concentration at the locations where the G-band brightness is high and the magnetic field is strong. The clear anticorrelation ($r = -0.85$) of CH number density and magnetic field strength for strong magnetic fields ($B > 500$ G) evident from the scatter plot of both quantities shown in Fig. 5.8 confirms this impression.

The latter figure also indicates the number density depends roughly quadratically on B , which fits well to the similar dependence of G-band brightness on B as revealed by Fig. 5.4. This results suggest that the G-band brightness for $B > 500$ G is determined by reduced number density of CH molecules in the magnetic flux concentrations.

Actually, there are two effects that can lead to a local brightness enhancement in G-band filtergrams: (1) a larger continuum intensity and (2) weaker CH lines. Fig. 5.6 shows

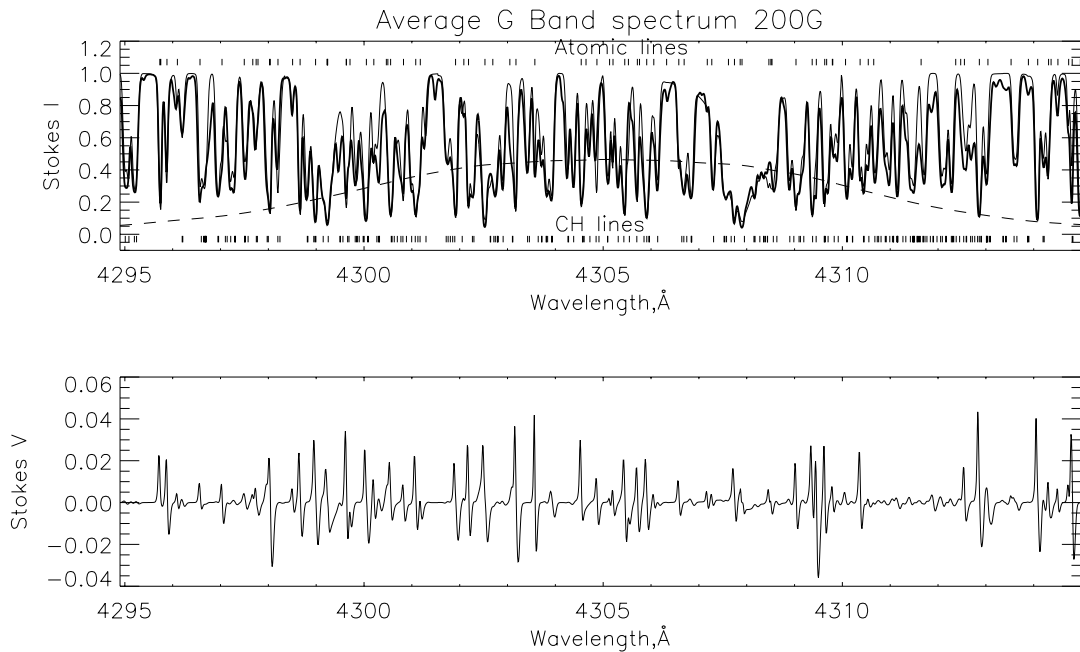


Figure 5.2: Spatially averaged spectra of Stokes I (top) and Stokes V (bottom) calculated for a snapshot from the run with 200 G average vertical magnetic field. Atomic and molecular lines are indicated on the Stokes- I plot. The dashed line shows the shape of the filter function which is used for calculating the G-band intensity. The thick line shows the observed spectrum of quiet region of the Sun.

that the first effect is responsible for the brightening of (non-magnetic) granules: the normalized G-band intensity is, on average, equal to the normalized continuum intensity at 430 nm. For the magnetic bright points, the G-band intensity is much larger than the normalized continuum intensity, indicating that weakening of the CH lines is an important factor. This is demonstrated by Fig. 5.10, which shows the G-band spectra of a magnetic bright point, a bright granule, a weakly magnetic intergranular dark point, and a magnetic dark point, all normalized to the average continuum intensity at 430 nm. While the granule has a G-band intensity enhancement nearly equal to the corresponding normalized continuum intensity, the magnetic bright point shows a much larger G-band brightness due to the drastic weakening of the CH lines. The intergranular dark point has a low G-band brightness mainly because of its low continuum intensity (Fig. 5.5).

The large G-band intensity of magnetic bright points and the weakening of the CH lines are connected with the higher temperature (at equal optical depth) and lower density in the flux concentrations. To a good approximation, these are in total (gas + magnetic) pressure balance with their environment leading to an average Wilson depression of about 170 km (Shelyag et al. 2004). The vertically outgoing radiative flux in the flux concentrations is provided by lateral radiation from the ‘hot walls’ of the flux concentrations, so that the total radiative cooling rate in the flux concentrations is near to zero, in contrast to the non-magnetic solar surface where a strong radiative cooling is balanced by heating through convection.

The strong weakening of the CH lines in magnetic flux concentrations can be under-

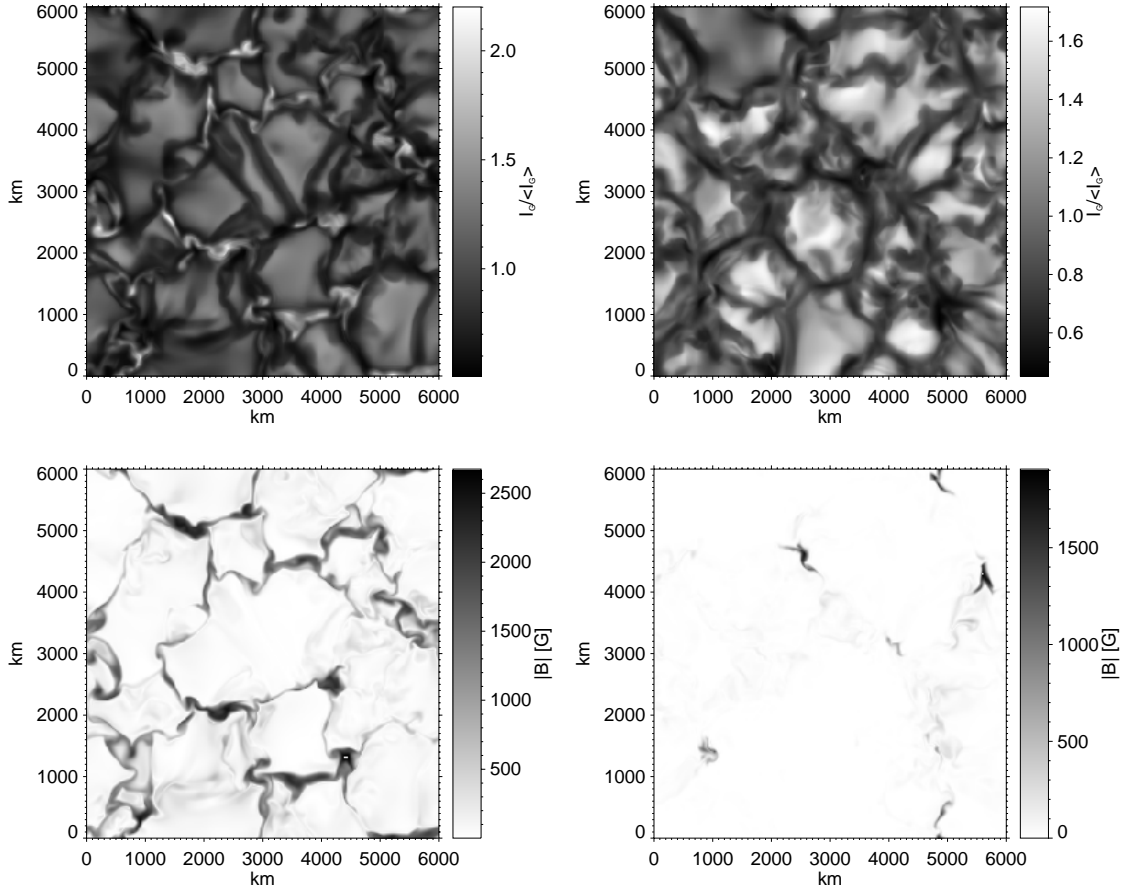


Figure 5.3: Comparison between normalized G-band brightness (upper panels) and magnetic field strength at $\tau = 1$ (500 nm, lower panels) for the snapshot from the 200-G run (left side) and the 10-G run (right side), respectively. While the simulated plage region (200-G run) shows many brightenings of magnetic features exceeding the brightness of granules, there are only a few bright features in the simulated quiet region.

stood by considering Figure 5.9, which shows the main thermodynamic quantities and the number density of CH molecules for the average atmospheres corresponding to the magnetic bright points ($B > 1000$ G and $I_G / \langle I_G \rangle > 1.5$; solid curves) and the average weakly magnetized part ($B < 50$ G; dot-dashed curves) of the atmosphere. Diamond and asterisk symbols indicate the heights at which $\tau = 1$ is reached in G-band continuum and in the center of the CH line at 429.5 nm (taken as a representative for the CH lines), respectively, and thus roughly cover the height range over which the CH lines are formed.

The prominent maximum in the CH number density for the granules (Fig. 5.9d) is produced by the rapid outward drop in temperature around the continuum-forming layers (Fig. 5.9a) and the associated density plateau (Fig. 5.9b). On the other hand, the low density in the magnetic flux concentrations leads to a strong depletion of CH above $z \approx 0$. Therefore, the optical depth scale at the center of any CH line is geometrically shifted downward more strongly than the corresponding level for the G-band continuum, so that the line is formed over a height range of only $\simeq 30$ km (in comparison to about 180 km for the weakly magnetic atmosphere). Together with the flatter temperature gradient in

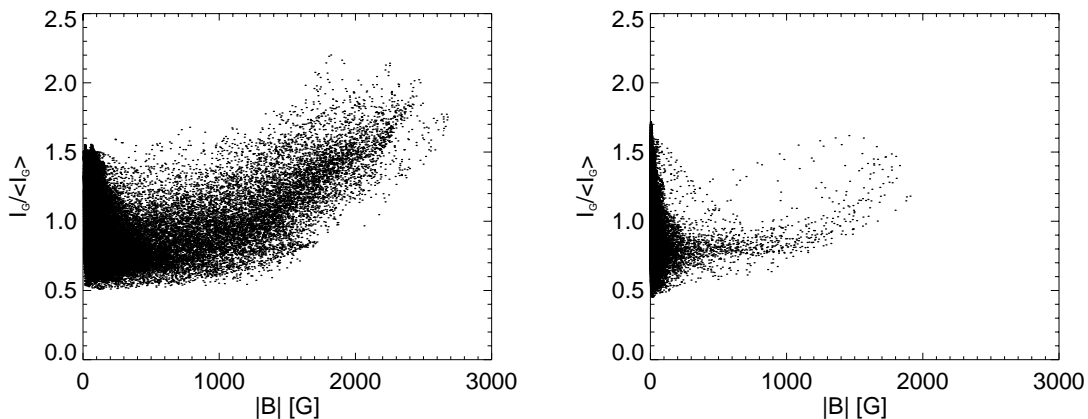


Figure 5.4: Scatter plots of G-band brightness vs. magnetic field strength for the 200-G run (left) and for the 10-G run (right). The brightness of the points with strong magnetic field exceeds that of the (weakly magnetized) granules in the 200-G case. The few flux concentrations in the 10-G case are smaller and weaker than the features shown by the 200-G case, and they do not exceed the brightness of the brightest granules.

the flux concentrations, this leads to a much smaller temperature difference between the layers where the continuum and where the CH line core is formed as in the case of the non-magnetic atmosphere: the line becomes weaker in regions of strong magnetic field. In combination with their high continuum intensity due to lateral radiative heating of the flux concentrations in that height range, this leads to a strong increase of G-band brightness in the magnetic flux concentrations.

5.3 Polarimerty in G Band

As it is shown in the previous section, the magnetic sensitivity of the CH lines in the G band is not strong in comparison to the atomic lines. But it is of interest to study the polarization signals of the CH lines in order to provide direct measurements of the magnetic fields in the G-band bright points. By comparing the synthetic G-band spectra with and without the atomic lines included, Uitenbroek et al. (2004) have shown that the wavelength range around 430.4 nm can be used as a diagnostical tool for the investigation of the magnetic fields in the layers of CH line formation. This wavelength range includes six lines. Two lines in this range (main branch lines with rotational transition R_{11} at 430.3925 and 430.3932 nm with $J_l = 1.5$ and $J_u = 2.5$ and $g_{\text{eff}} = 0.8833$) are more magnetically sensitive and overlap other less sensitive CH lines. This results in the appearance of the asymmetric Stokes- V profile around 430.4 nm in strong magnetic field.

The simulated slit images, the corresponding G-band intensity and the vertical magnetic field strength are shown in Fig. 5.11. The images show the strong weakening of the CH lines in the strong magnetic field, and the response of the Stokes- V signal to the magnetic field. Also one can see that the G-band intensity doesn't directly represent the magnetic field strength, and the strong magnetic field is necessary, but not sufficient to make the magnetic bright point to appear. The reason of the low G-band intensity in some

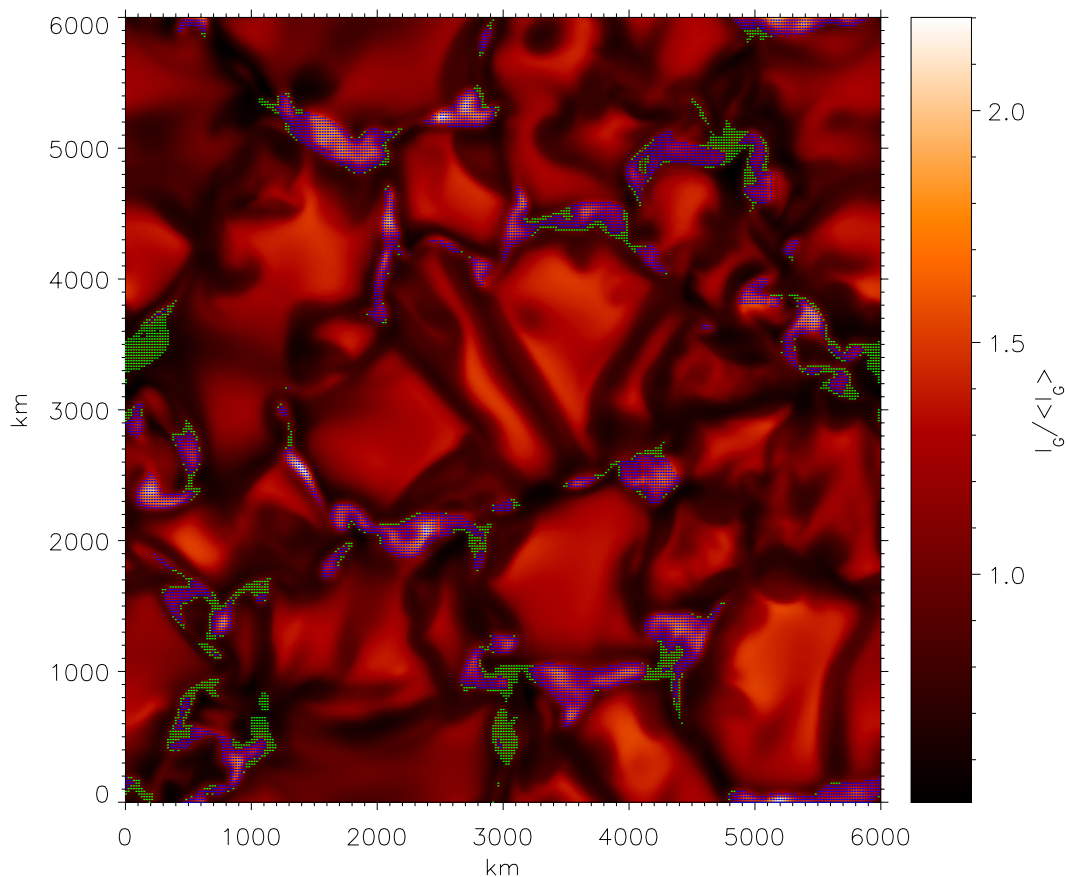


Figure 5.5: Map of the G-band intensity with the regions of strong magnetic field and weak G-band intensity ($B > 1000\text{ G}$, $I_G / \langle I_G \rangle < 1$), marked by green, and the regions of strong magnetic field and strong G-band intensity ($B > 1000\text{ G}$, $I_G / \langle I_G \rangle > 1$), marked by blue. The regions with the strong magnetic field and the weak G-band intensity are mainly located on the edges of the magnetic downflows, where the continuum intensity is weak.

regions of strong magnetic field is the low continuum intensity (see Sect. 5.2).

The images of the unnormalized area asymmetry (integrated Stokes- V parameter), the total Stokes- V area (integrated modulus of the Stokes- V parameter) and their correlations to the vertical magnetic field strength, calculated for the synthetic Stokes- V profiles of the CH lines at 430.4 nm, are shown in Fig. 5.12. The scatterplots show that the unnormalized area asymmetry of the Stokes- V profiles is maximal at the magnetic field $B_z \approx 1\text{ kG}$, but the maximum of the total Stokes- V area is located at the stronger magnetic fields $B_z \approx 1.5\text{ kG}$. As one can see from the image of the area asymmetry, the strongest asymmetry appears on the borders of the magnetic flux concentrations, where the gradient of the velocity and the gradient of the magnetic field are strong and have the opposite sign (Grossmann-Doerth et al. 1988). The hook-like structure of dependence of the total Stokes- V area on the magnetic field strength is caused from one side by the increase of the Stokes- V amplitude with increase of the magnetic field, and from the other side by the CH line weakening due to the smaller absorption of the CH molecules.

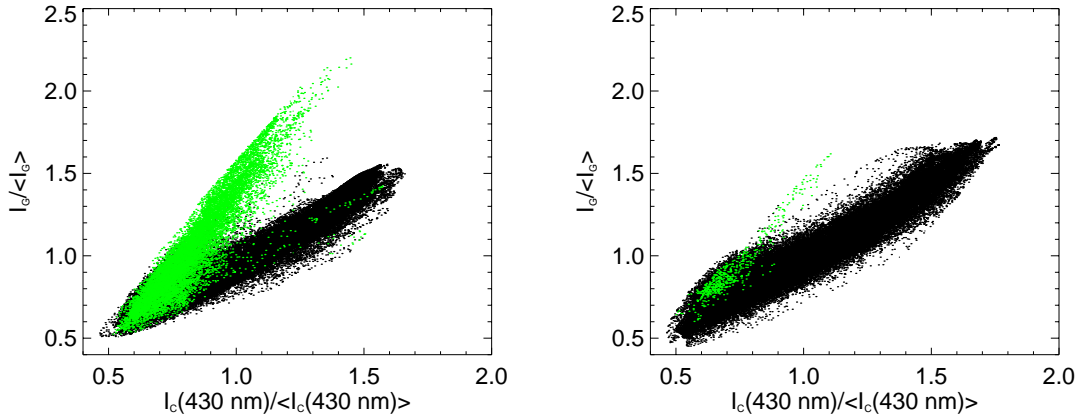


Figure 5.6: Scatter plots of G-band brightness vs. continuum brightness at 430 nm for the 200-G (left) and 10-G (right) runs. The slope of the distributions indicates a clear separation into two components corresponding to magnetic flux concentrations ($|B| > 500$ G, green dots) and weakly magnetized atmosphere (black dots), mainly corresponding to granules. In the 10-G case, the component corresponding to the magnetic flux concentrations is only weak, reflecting their small area fraction.

5.4 Comparison with observational data

The rms contrast of our synthetic G-band images is about 25% for the 200-G run, which is much larger than the value of about 10% obtained from ground-based observations under very good seeing conditions. Apparently, the image degradation due to the turbulent terrestrial atmosphere leads to reduced values of the contrast observed on the ground. In order to compare our results with observations, we have to artificially degrade the synthetic G-band images, thus mimicking the effect of the atmosphere and telescope. We have therefore convolved our images with a point spread function consisting of two parts: an Airy function $A_{\lambda,D}$ for the telescope and a function representing the effect of the atmosphere (Nordlund 1984, Collados and Vázquez 1987):

$$\text{PSF}(r) = A_{\lambda,D}(r) + \frac{b}{(a^2 + r^2)^{3/2}}, \quad (5.1)$$

Here $\lambda = 430$ nm (wavelength of observation) and D is the telescope aperture. The parameters a and b of the atmosphere function describe its width and amplitude, respectively. As long as the atmosphere PSF is much wider than the telescopic PSF, the former only degrades the rms intensity contrast without strongly affecting the spatial resolution of the image (the resolution being more affected by speckle effects, which are not included in our simplistic treatment). In this case, the smoothing does not depend sensitively on the precise value of a since the wings of the atmosphere PSF are anyway very broad. Effectively the only remaining free parameter is then b , the relative amplitude of the atmosphere PSF. We fix b by requiring that the rms intensity contrast of the smoothed image matches the value for the observed image.

The observed image of an active region, which was used for comparison, was recorded on May 22, 2002 with the Dutch Open Telescope (DOT) (Hammerschlag and Bettonvil

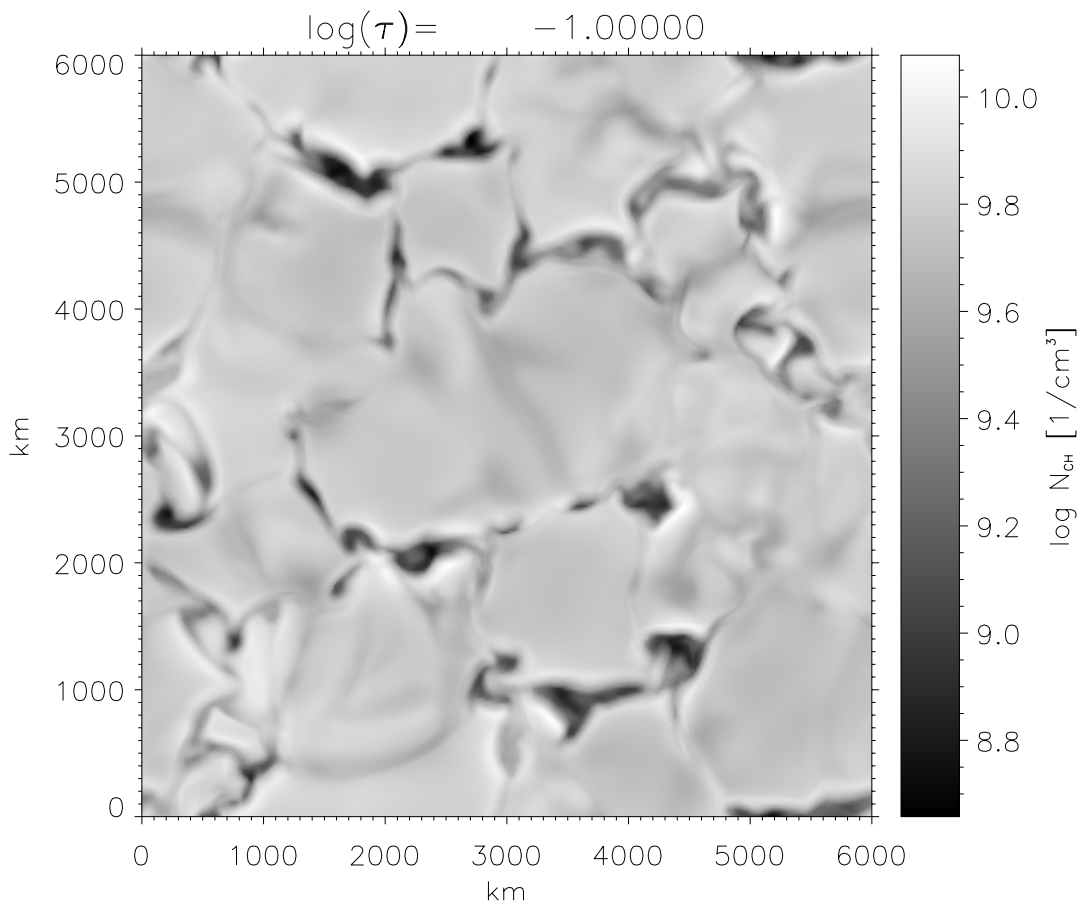


Figure 5.7: Number density of CH molecules at the level $\log \tau = -1.0$ (500 nm) for the 200-G run. The dark regions with low CH concentration correspond to strong magnetic field concentrations and are cospatial with the brightenings on the G-band image (left part of Fig. 5.3).

1998) on La Palma (Spain). The selected part of this image has the same physical size as the simulated domain and a similar area fraction of G-band bright points as the 200-G run. Fig. 5.14 shows the smoothed simulated image (left) and the observed image (right). Choosing 120 km for the FWHM of the Airy function (corresponding to the 45 cm aperture of the DOT telescope) and a FWHM of 1500 km for the atmosphere function we find that the smoothed simulated image matches the rms contrast of the observed image of about 7.4% for $b = 0.004$. The degradation of the contrast by a factor 3.4 is comparable to the correction factors obtained by Collados & Vazquez (1987) assuming a similar form of the PSF. In order to evaluate the consistency of our smoothing procedure we compare in Fig. 5.13 the G-band brightness distribution functions of simulated (dash-dotted line), observed (dashed line), and smoothed simulated (solid line) images. The latter two curves show a very good agreement although no further fitting procedure has been applied. Schüssler et al. (2003) have applied the same procedure to data from the new Swedish Solar Telescope (SST) on La Palma new SST and also obtained matching brightness distribution functions with similar parameter values.

Scatterplots of G-band intensity vs. continuum intensity at 432 nm for the simulated

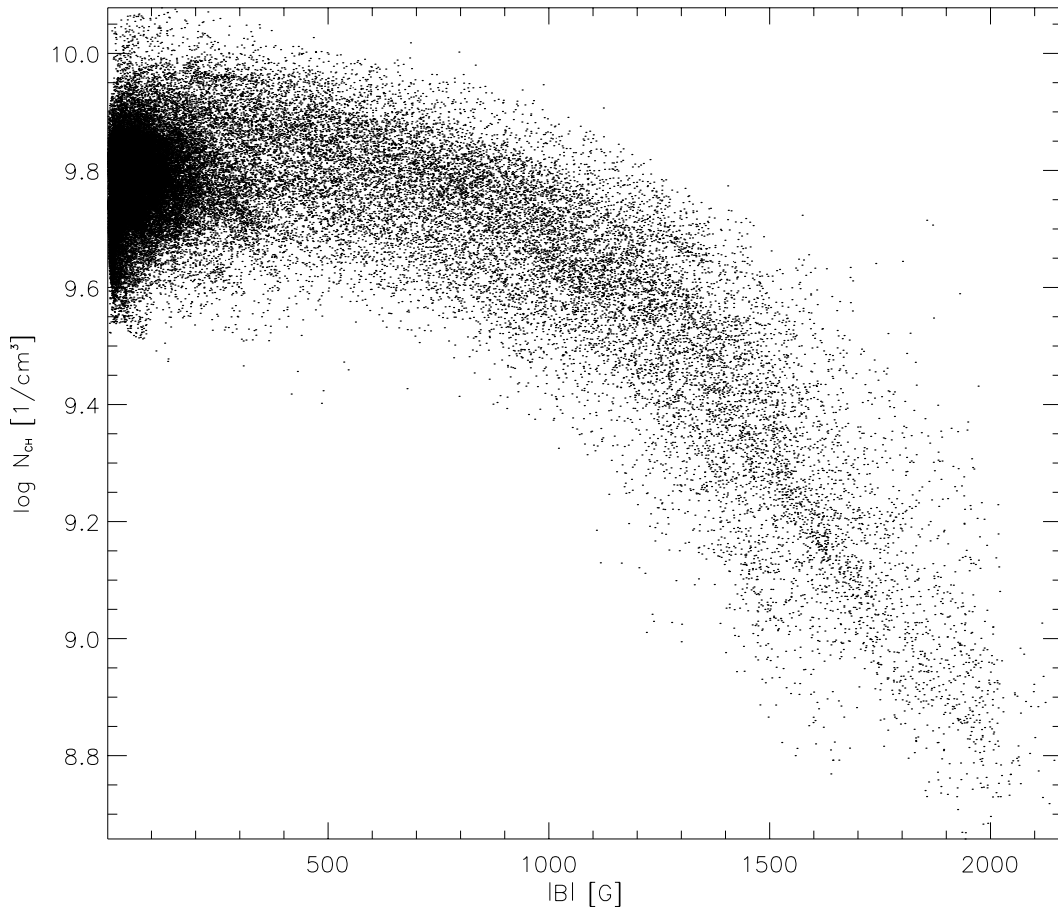


Figure 5.8: Scatter plot of the number density of CH molecules vs. magnetic field strength (both at $\log \tau = -1.0$ for 500 nm), calculated for the 200-G run.

and smoothed image (left) and for the observed image (right) are given in Fig. 5.15. The two populations of bright points, which we have already identified to represent strongly and weakly magnetized structures, respectively, are already visible (cf. Fig. 5.6). This confirms the magnetic nature of the intergranular G-band brightenings (see also Berger et al. (1998), Berger and Title (2001)).

5.5 Conclusions

The results presented in this chapter are based on realistic 3-D radiative MHD simulations with high horizontal grid resolution and on a detailed treatment of the G-band spectrum synthesis. By comparing realistic simulations with observations, we have shown that the G-band brightening of small magnetic flux concentrations in the solar photosphere is most probably due to the lateral heating and partial evacuation of the magnetic structures. The values of observed G-band contrast are quantitatively reproduced after smoothing the simulated image to mimic the image deterioration by telescope and atmosphere. There is a clear spatial correlation of the G-band brightenings and magnetic flux concentrations.

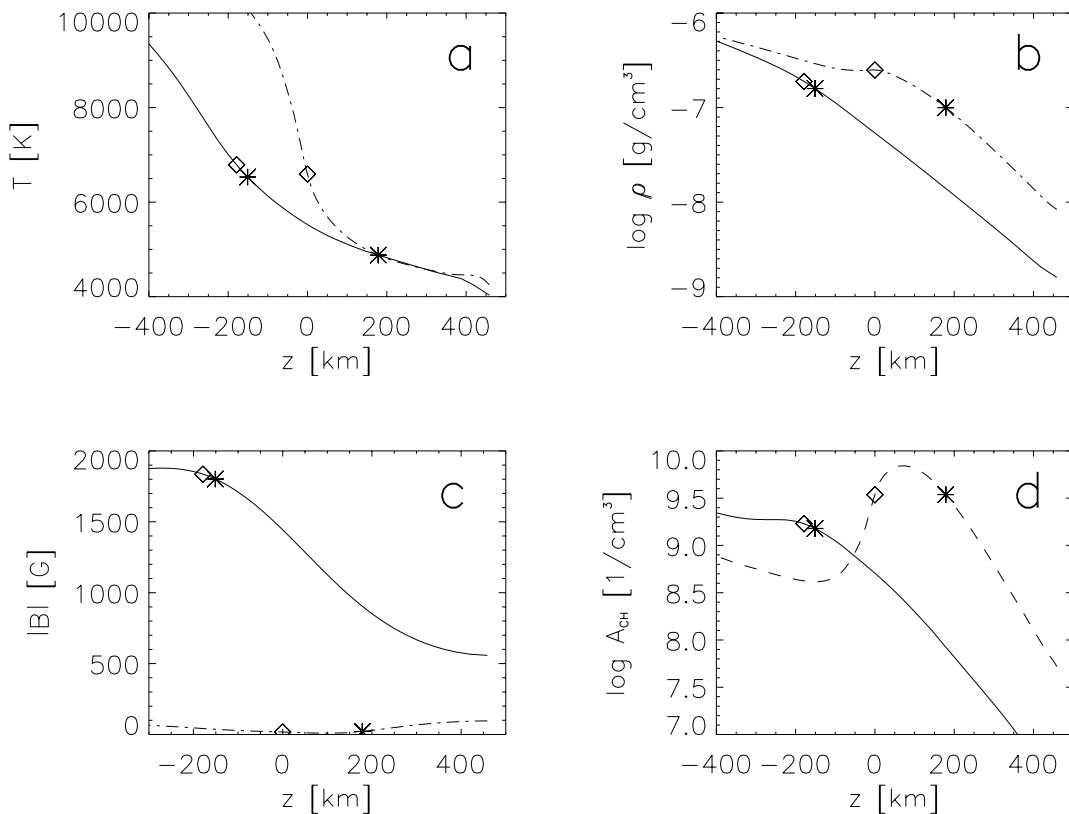


Figure 5.9: Temperature (a), density (b), magnetic field strength (c) and number density of CH molecules (d) as functions of geometrical depth for the average weakly magnetized atmosphere ($|B| < 50$ G; dot-dashed lines) and for the average atmosphere corresponding to magnetic bright points ($|B| > 1000$ G, $I_G/\langle I_G \rangle > 1.5$; solid lines). The asterisks on the curves indicate the optical depth levels $\tau = 3/2$ calculated for the center of the CH line at 430.43 nm. $z = 0$ corresponds to $\tau = 3/2$ (430.43 nm) level for the average weakly magnetized atmosphere. The continuum optical depth levels $\tau_{430} = 3/2$ for the dependences are marked by the squares. Owing to the lower CH abundance in the magnetic flux concentrations above $z \approx 0$, the formation region of the CH lines is shifted geometrically downward to a region with larger temperature and smaller temperature gradient than outside. Consequently, the CH lines are strongly weakened and the G-band spectral region becomes brighter.

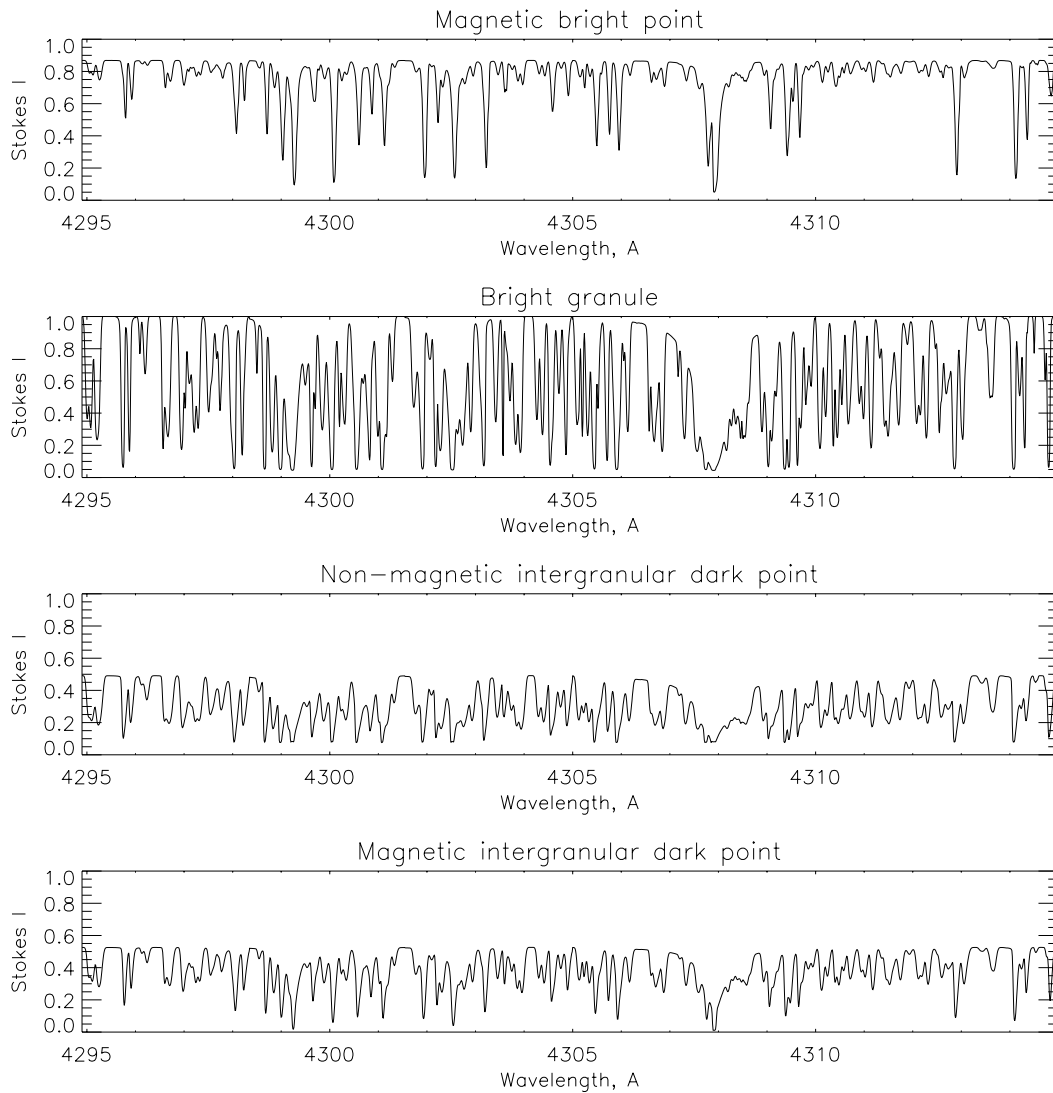


Figure 5.10: The Stokes I spectra of a magnetic bright point, a bright granule, a non-magnetic intergranular dark point and a magnetic dark point. The spectra are normalized to the average continuum intensity at 430.0 nm. The CH lines are drastically weakened in the magnetic bright point, the remaining strong lines being atomic lines. They are also somewhat weakened in the magnetic dark point.

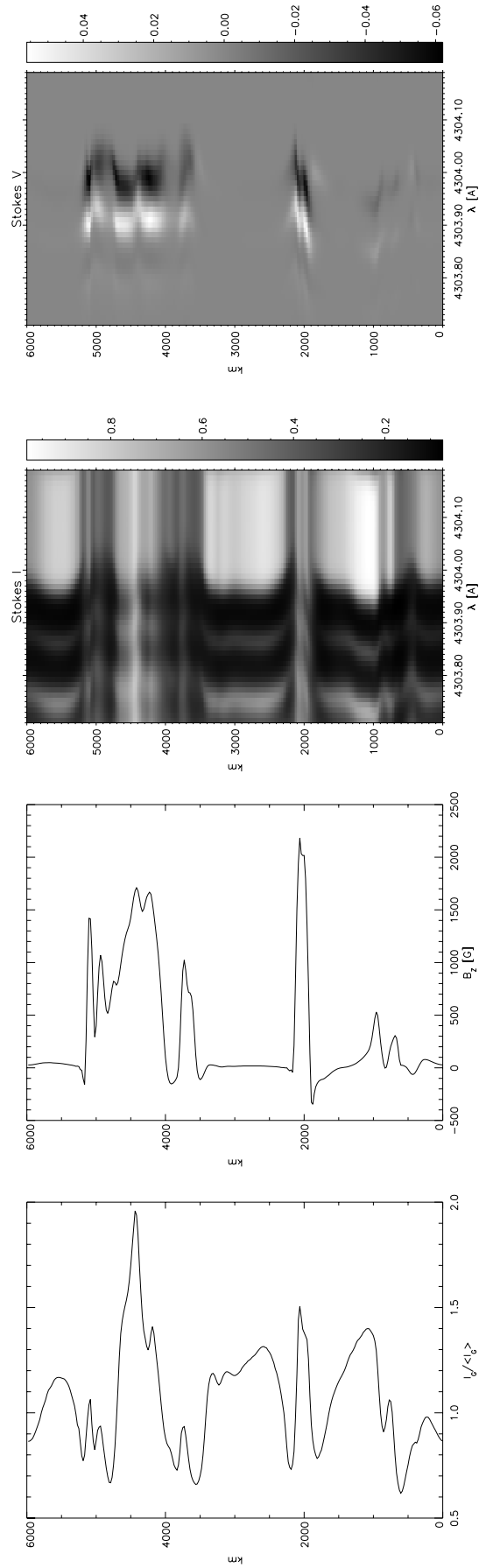


Figure 5.11: G-band intensity, vertical magnetic field strength, Stokes I and Stokes V parameters calculated for the slit located in horizontal direction at 2083 km. The images show Stokes V response and the weakening of CH lines at the regions where the magnetic field is strong.

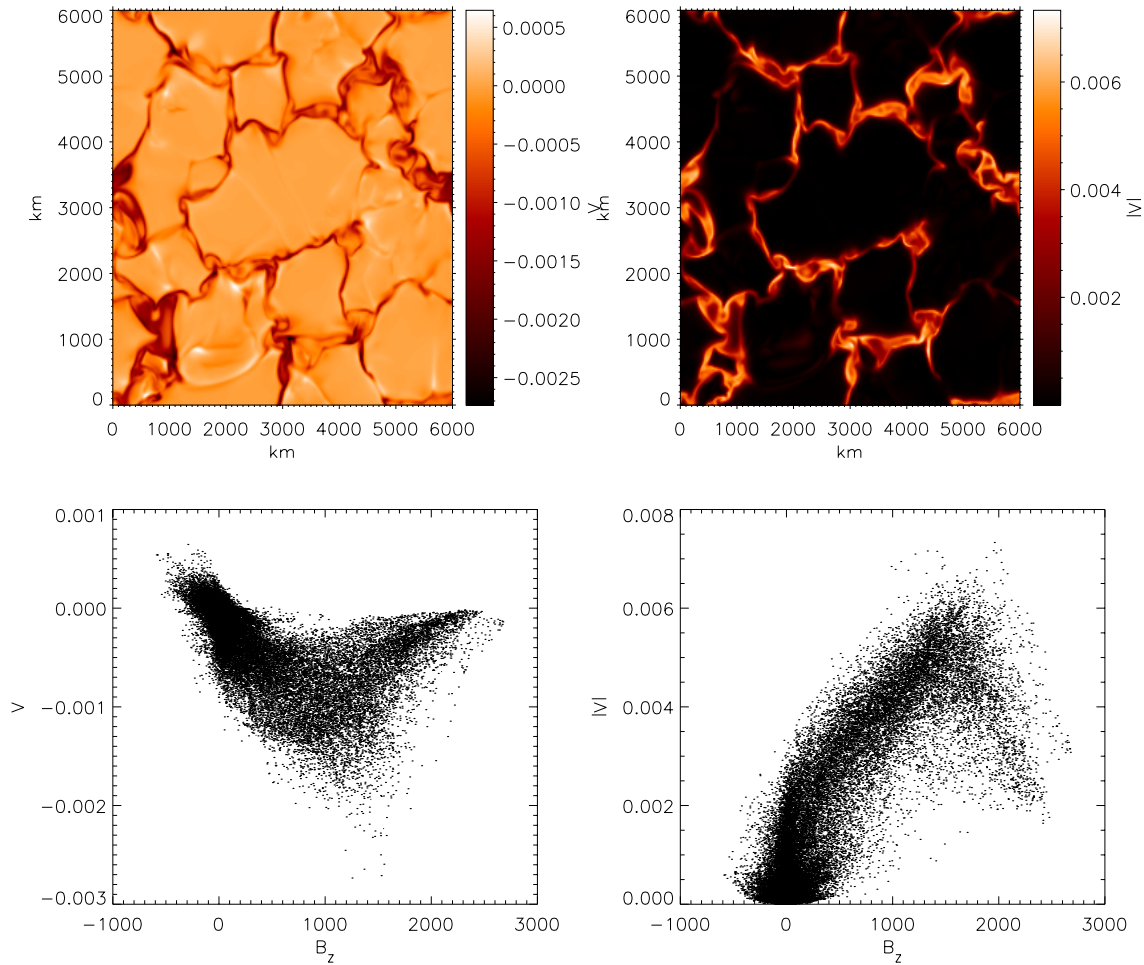


Figure 5.12: Images of the unnormalized area asymmetry and the total Stokes- V area and the scatter plots of these quantities vs. the vertical magnetic field strength, calculated for the Stokes- V profile of CH lines at 430.4 nm.

These brightenings are caused by a strong reduction in the number density of the CH molecule, and thus the weakening of the CH lines in the G-band. Granules also appear bright in the G-band. This is mainly due to continuum brightening. Very good agreement between the output of our simulations and the brightness distribution functions of observed images confirms the physical model of magnetic flux concentrations as laterally heated and evacuated structures.

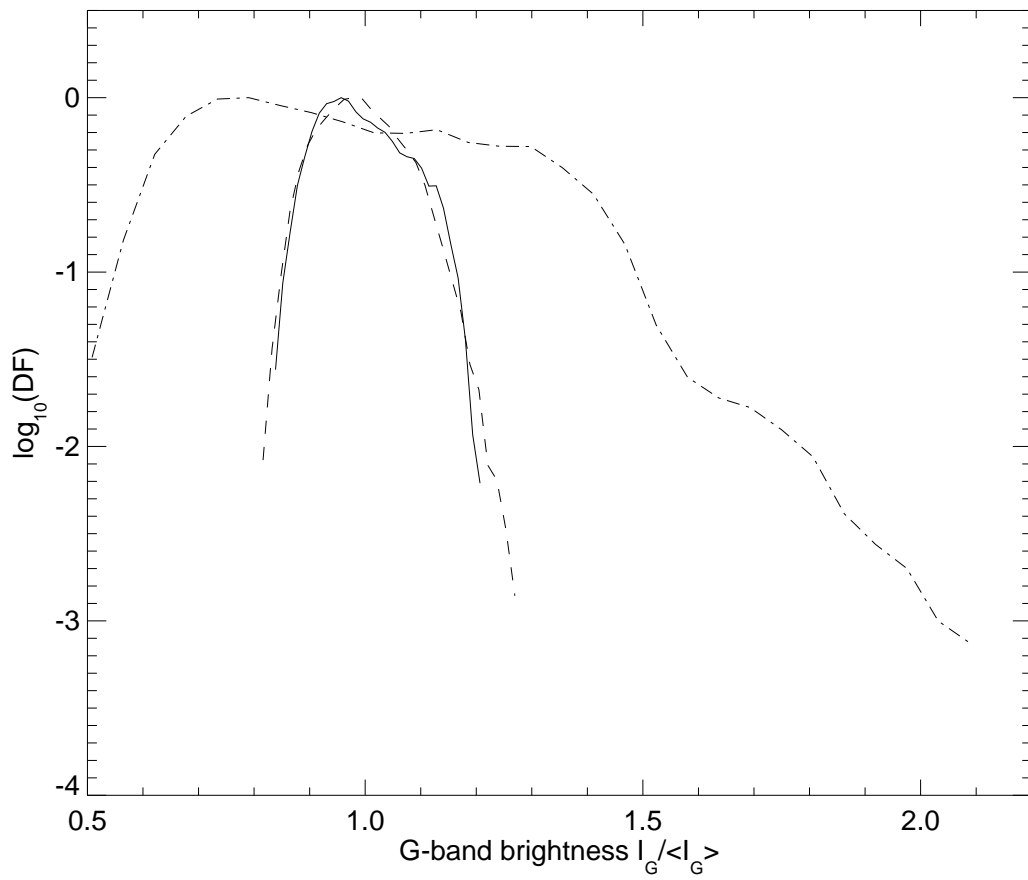


Figure 5.13: Distribution functions of G-band brightness for the simulated (dash-dotted line), observed (dashed line), and smoothed simulated (solid line) images.

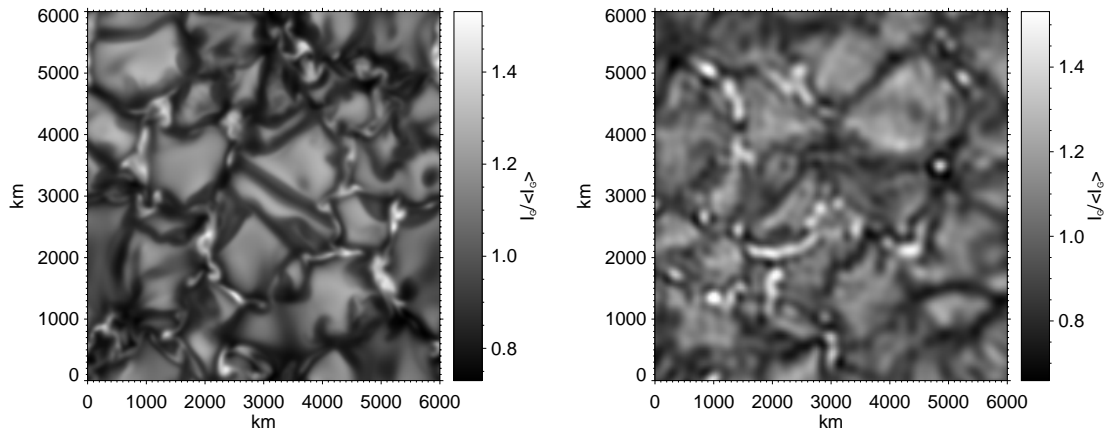


Figure 5.14: The simulated and observed G-band images. Left: synthetic G-band image of the simulated area after spatial smoothing by the function mimicking the diffraction by the telescope and the image degradation by the Earth's atmosphere. Right: observed G-band image with a similar area fraction of G-band bright points as in the simulation (subfield of an image taken with the Dutch Open Telescope on La Palma, courtesy: P. Sütterlin).

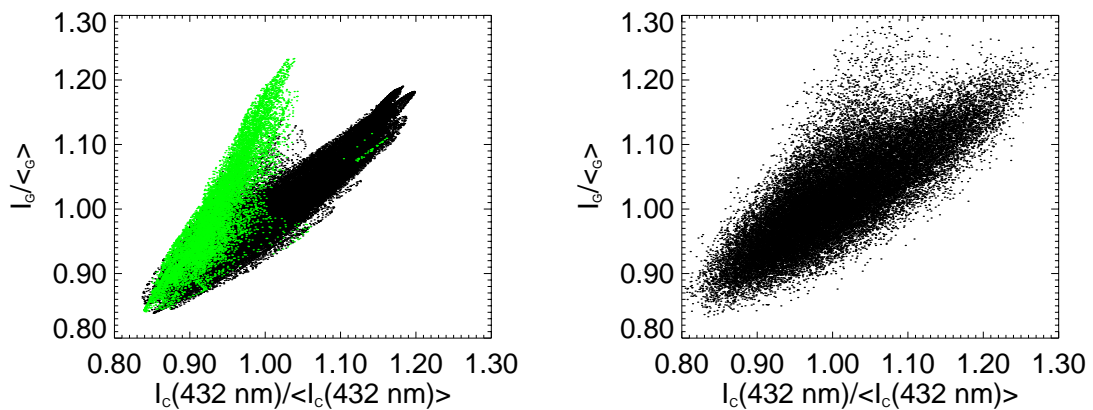


Figure 5.15: Scatter plots of normalized G-band vs continuum (432 nm) intensity (200-G run) for the synthetic (left) and observed (right) images. The scatter plots show the separation in two components for both observed and simulated images. Green dots on the scatter-plot for the simulated image correspond to the magnetic component ($B > 500\text{G}$) of the image.

A The G-Band lines table

In the Appendix A the tables of the lines, used for the calculation of the G-Band spectra, are shown.

The first table is the table of the CH lines. The general atomic parameters of the chemical elements, involved in the G-Band spectral range calculation, are shown in the second table. The third table is the table of the atomic lines in the G-Band spectral range. The description of the parameters is given in Chapter 3.

A.1 CH lines of G Band

Wavelength, Å	Branch	IU	IL	JL	VU	VL	FVV
4295.009	'Q'	1	1	17.5	0	0	0.387E-02
4295.085	'Q'	2	2	16.5	0	0	0.387E-02
4295.199	'Q'	2	2	15.5	0	0	0.387E-02
4295.245	'Q'	1	1	16.5	0	0	0.387E-02
4296.198	'R'	2	2	1.5	1	1	0.344E-02
4296.211	'R'	2	2	1.5	1	1	0.344E-02
4296.598	'R'	2	2	1.5	0	0	0.387E-02
4296.648	'R'	2	2	1.5	0	0	0.387E-02
4296.657	'Q'	2	2	23.5	1	1	0.344E-02
4296.676	'Q'	1	1	25.5	1	1	0.344E-02
4296.681	'Q'	1	1	23.5	1	1	0.344E-02
4296.683	'Q'	1	1	24.5	1	1	0.344E-02
4296.696	'Q'	2	2	22.5	1	1	0.344E-02
4296.707	'Q'	2	2	24.5	1	1	0.344E-02
4296.946	'Q'	1	1	16.5	0	0	0.387E-02
4296.960	'Q'	2	2	15.5	0	0	0.387E-02
4297.101	'Q'	2	2	21.5	1	1	0.344E-02
4297.139	'Q'	1	1	22.5	1	1	0.344E-02
4297.213	'Q'	2	2	14.5	0	0	0.387E-02
4297.295	'Q'	1	1	15.5	0	0	0.387E-02
4297.308	'Q'	2	1	2.5	1	1	0.344E-02

Continued on the next page...

A The G-Band lines table

Wavelength, Å	Branch	IU	IL	JL	VU	VL	FVV
4297.309	'Q'	2	1	2.5	1	1	0.344E-02
4297.502	'Q'	1	1	21.5	1	1	0.344E-02
4297.514	'R'	1	1	2.5	1	1	0.344E-02
4297.516	'R'	1	1	2.5	1	1	0.344E-02
4297.577	'Q'	2	2	20.5	1	1	0.344E-02
4297.749	'Q'	2	1	2.5	0	0	0.387E-02
4297.771	'Q'	2	1	2.5	0	0	0.387E-02
4297.976	'R'	1	1	2.5	0	0	0.387E-02
4297.999	'R'	1	1	2.5	0	0	0.387E-02
4298.198	'Q'	2	2	19.5	1	1	0.344E-02
4298.242	'Q'	1	1	20.5	1	1	0.344E-02
4298.814	'Q'	2	2	14.5	0	0	0.387E-02
4298.827	'Q'	1	1	15.5	0	0	0.387E-02
4298.950	'R'	2	2	3.5	2	2	0.281E-02
4298.976	'Q'	1	1	19.5	1	1	0.344E-02
4298.993	'Q'	2	2	18.5	1	1	0.344E-02
4299.146	'Q'	2	2	13.5	0	0	0.387E-02
4299.146	'R'	2	2	3.5	2	2	0.281E-02
4299.252	'Q'	1	1	14.5	0	0	0.387E-02
4299.496	'R'	2	2	0.5	1	1	0.344E-02
4299.507	'R'	2	2	0.5	1	1	0.344E-02
4299.559	'R'	1	1	4.5	2	2	0.281E-02
4299.657	'Q'	1	1	23.5	1	1	0.344E-02
4299.686	'R'	1	1	4.5	2	2	0.281E-02
4299.816	'Q'	2	2	22.5	1	1	0.344E-02
4299.845	'Q'	2	2	17.5	1	1	0.344E-02
4299.860	'Q'	1	1	24.5	1	1	0.344E-02
4299.860	'Q'	1	1	18.5	1	1	0.344E-02
4299.899	'Q'	1	1	22.5	1	1	0.344E-02
4299.982	'Q'	2	2	23.5	1	1	0.344E-02
4300.003	'Q'	2	2	21.5	1	1	0.344E-02
4300.075	'Q'	1	1	21.5	1	1	0.344E-02
4300.091	'Q'	1	1	25.5	1	1	0.344E-02
4300.269	'Q'	2	2	20.5	1	1	0.344E-02
4300.302	'Q'	2	2	24.5	1	1	0.344E-02
4300.317	'R'	2	2	0.5	0	0	0.387E-02
4300.324	'R'	2	2	0.5	0	0	0.387E-02
4300.570	'Q'	2	2	13.5	0	0	0.387E-02
4300.587	'Q'	1	1	14.5	0	0	0.387E-02
4300.633	'Q'	1	1	20.5	1	1	0.344E-02
4300.696	'Q'	2	2	19.5	1	1	0.344E-02

Continued on the next page...

Wavelength, Å	Branch	IU	IL	JL	VU	VL	FVV
4300.772	'Q'	2	2	16.5	1	1	0.344E-02
4300.813	'Q'	1	1	17.5	1	1	0.344E-02
4300.887	'Q'	1	1	26.5	1	1	0.344E-02
4300.996	'Q'	2	2	12.5	0	0	0.387E-02
4301.072	'Q'	2	2	25.5	1	1	0.344E-02
4301.127	'Q'	1	1	13.5	0	0	0.387E-02
4301.172	'Q'	1	1	19.5	1	1	0.344E-02
4301.296	'Q'	2	2	18.5	1	1	0.344E-02
4301.718	'Q'	2	2	15.5	1	1	0.344E-02
4301.758	'Q'	1	1	16.5	1	1	0.344E-02
4301.805	'Q'	1	1	27.5	1	1	0.344E-02
4301.853	'Q'	1	1	18.5	1	1	0.344E-02
4301.897	'Q'	2	2	17.5	1	1	0.344E-02
4302.053	'Q'	2	2	26.5	1	1	0.344E-02
4302.266	'Q'	2	2	12.5	0	0	0.387E-02
4302.297	'Q'	1	1	13.5	0	0	0.387E-02
4302.638	'Q'	1	1	17.5	1	1	0.344E-02
4302.647	'Q'	2	2	16.5	1	1	0.344E-02
4302.714	'Q'	2	2	14.5	1	1	0.344E-02
4302.745	'Q'	2	2	11.5	0	0	0.387E-02
4302.786	'Q'	2	1	1.5	1	1	0.344E-02
4302.795	'Q'	2	1	1.5	1	1	0.344E-02
4302.803	'Q'	1	1	15.5	1	1	0.344E-02
4302.908	'Q'	1	1	12.5	0	0	0.387E-02
4303.103	'R'	1	1	1.5	1	1	0.344E-02
4303.112	'R'	1	1	1.5	1	1	0.344E-02
4303.420	'Q'	1	1	16.5	1	1	0.344E-02
4303.420	'Q'	2	2	15.5	1	1	0.344E-02
4303.457	'Q'	1	1	28.5	1	1	0.344E-02
4303.642	'Q'	2	2	27.5	1	1	0.344E-02
4303.714	'Q'	2	2	13.5	1	1	0.344E-02
4303.718	'R'	2	2	2.5	2	2	0.281E-02
4303.809	'R'	2	2	2.5	2	2	0.281E-02
4303.812	'Q'	1	1	14.5	1	1	0.344E-02
4303.838	'Q'	2	2	11.5	0	0	0.387E-02
4303.925	'R'	1	1	1.5	0	0	0.387E-02
4303.929	'Q'	1	1	12.5	0	0	0.387E-02
4303.933	'R'	1	1	1.5	0	0	0.387E-02
4304.263	'Q'	2	2	14.5	1	1	0.344E-02
4304.276	'Q'	1	1	15.5	1	1	0.344E-02
4304.383	'Q'	2	2	10.5	0	0	0.387E-02

Continued on the next page...

A The G-Band lines table

Wavelength, Å	Branch	IU	IL	JL	VU	VL	FVV
4304.567	'R'	1	1	3.5	2	2	0.281E-02
4304.578	'Q'	1	1	11.5	0	0	0.387E-02
4304.602	'R'	1	1	3.5	2	2	0.281E-02
4304.722	'Q'	2	2	12.5	1	1	0.344E-02
4304.852	'Q'	1	1	13.5	1	1	0.344E-02
4304.911	'Q'	1	1	29.5	1	1	0.344E-02
4305.093	'Q'	1	1	14.5	1	1	0.344E-02
4305.095	'Q'	2	2	13.5	1	1	0.344E-02
4305.314	'Q'	2	2	10.5	0	0	0.387E-02
4305.432	'Q'	1	1	11.5	0	0	0.387E-02
4305.547	'Q'	2	2	28.5	1	1	0.344E-02
4305.703	'Q'	2	2	11.5	1	1	0.344E-02
4305.853	'Q'	1	1	12.5	1	1	0.344E-02
4305.911	'Q'	2	2	9.5	0	0	0.387E-02
4305.955	'Q'	2	2	12.5	1	1	0.344E-02
4305.968	'Q'	1	1	13.5	1	1	0.344E-02
4306.139	'Q'	1	1	10.5	0	0	0.387E-02
4306.643	'Q'	2	2	10.5	1	1	0.344E-02
4306.686	'Q'	2	2	9.5	0	0	0.387E-02
4306.747	'Q'	2	2	11.5	1	1	0.344E-02
4306.842	'Q'	1	1	11.5	1	1	0.344E-02
4306.844	'Q'	1	1	12.5	1	1	0.344E-02
4306.851	'Q'	1	1	10.5	0	0	0.387E-02
4307.308	'Q'	2	2	8.5	0	0	0.387E-02
4307.527	'Q'	2	2	9.5	1	1	0.344E-02
4307.543	'Q'	2	2	10.5	1	1	0.344E-02
4307.579	'Q'	1	1	9.5	0	0	0.387E-02
4307.675	'Q'	1	1	11.5	1	1	0.344E-02
4307.744	'Q'	1	1	10.5	1	1	0.344E-02
4307.952	'Q'	2	2	8.5	0	0	0.387E-02
4308.152	'Q'	1	1	30.5	1	1	0.344E-02
4308.175	'Q'	1	1	9.5	0	0	0.387E-02
4308.275	'Q'	2	2	9.5	1	1	0.344E-02
4308.358	'R'	2	2	1.5	2	2	0.281E-02
4308.360	'Q'	2	2	8.5	1	1	0.344E-02
4308.392	'Q'	2	2	29.5	1	1	0.344E-02
4308.433	'Q'	1	1	10.5	1	1	0.344E-02
4308.436	'R'	2	2	1.5	2	2	0.281E-02
4308.557	'Q'	2	2	7.5	0	0	0.387E-02
4308.631	'Q'	1	1	9.5	1	1	0.344E-02
4308.901	'Q'	1	1	8.5	0	0	0.387E-02

Continued on the next page...

Wavelength, Å	Branch	IU	IL	JL	VU	VL	FVV
4308.986	'Q'	2	2	8.5	1	1	0.344E-02
4309.094	'Q'	2	2	7.5	0	0	0.387E-02
4309.123	'Q'	2	2	7.5	1	1	0.344E-02
4309.194	'Q'	1	1	9.5	1	1	0.344E-02
4309.378	'Q'	1	1	8.5	0	0	0.387E-02
4309.452	'Q'	1	1	8.5	1	1	0.344E-02
4309.621	'R'	1	1	2.5	2	2	0.281E-02
4309.634	'R'	1	1	2.5	2	2	0.281E-02
4309.638	'Q'	2	2	7.5	1	1	0.344E-02
4309.701	'Q'	2	2	6.5	0	0	0.387E-02
4309.829	'Q'	2	2	6.5	1	1	0.344E-02
4309.913	'Q'	1	1	8.5	1	1	0.344E-02
4310.086	'Q'	1	1	7.5	0	0	0.387E-02
4310.108	'Q'	2	2	6.5	0	0	0.387E-02
4310.210	'Q'	1	1	7.5	1	1	0.344E-02
4310.216	'Q'	2	2	6.5	1	1	0.344E-02
4310.441	'Q'	2	2	5.5	1	1	0.344E-02
4310.456	'Q'	1	1	7.5	0	0	0.387E-02
4310.554	'Q'	1	1	7.5	1	1	0.344E-02
4310.759	'R'	1	2	5.5	0	0	0.387E-02
4310.80	'R'	1	2	5.5	1	1	0.344E-02
4310.679	'Q'	2	2	5.5	0	0	0.387E-02
4310.729	'Q'	2	2	5.5	1	1	0.344E-02
4310.896	'Q'	1	1	6.5	1	1	0.344E-02
4310.918	'Q'	2	2	4.5	1	1	0.344E-02
4310.991	'Q'	2	2	5.5	0	0	0.387E-02
4311.047	'R'	1	2	4.5	1	1	0.344E-02
4311.069	'P'	2	1	6.5	0	0	0.387E-02
4311.071	'R'	1	2	5.5	0	0	0.387E-02
4311.138	'Q'	2	2	4.5	1	1	0.344E-02
4311.149	'Q'	1	1	6.5	0	0	0.387E-02
4311.149	'R'	2	2	0.5	2	2	0.281E-02
4311.155	'Q'	1	1	6.5	1	1	0.344E-02
4311.160	'R'	2	2	0.5	2	2	0.281E-02
4311.266	'R'	1	2	4.5	1	1	0.344E-02
4311.326	'Q'	2	2	3.5	1	1	0.344E-02
4311.422	'Q'	1	1	6.5	0	0	0.387E-02
4311.471	'Q'	2	2	3.5	1	1	0.344E-02
4311.478	'Q'	1	1	31.5	1	1	0.344E-02
4311.486	'R'	1	2	3.5	1	1	0.344E-02
4311.500	'Q'	2	2	4.5	0	0	0.387E-02

Continued on the next page...

A The G-Band lines table

Wavelength, Å	Branch	IU	IL	JL	VU	VL	FVV
4311.508	'Q'	1	1	5.5	1	1	0.344E-02
4311.560	'Q'	2	2	2.5	1	1	0.344E-02
4311.575	'Q'	2	2	1.5	1	1	0.344E-02
4311.588	'Q'	2	2	1.5	1	1	0.344E-02
4311.612	'R'	1	2	4.5	0	0	0.387E-02
4311.631	'R'	1	2	3.5	1	1	0.344E-02
4311.685	'Q'	2	2	2.5	1	1	0.344E-02
4311.694	'Q'	1	1	5.5	1	1	0.344E-02
4311.727	'Q'	2	2	4.5	0	0	0.387E-02
4311.768	'R'	1	2	2.5	1	1	0.344E-02
4311.839	'R'	1	2	4.5	0	0	0.387E-02
4311.893	'R'	1	2	2.5	1	1	0.344E-02
4311.893	'R'	1	2	1.5	1	1	0.344E-02
4311.893	'P'	2	1	4.5	1	1	0.344E-02
4311.906	'R'	1	2	1.5	1	1	0.344E-02
4311.978	'P'	2	1	5.5	0	0	0.387E-02
4312.053	'Q'	1	1	4.5	1	1	0.344E-02
4312.090	'Q'	1	1	5.5	0	0	0.387E-02
4312.157	'Q'	2	2	3.5	0	0	0.387E-02
4312.177	'Q'	1	1	4.5	1	1	0.344E-02
4312.278	'Q'	1	1	5.5	0	0	0.387E-02
4312.296	'Q'	2	2	3.5	0	0	0.387E-02
4312.311	'R'	1	2	3.5	0	0	0.387E-02
4312.328	'P'	2	1	3.5	1	1	0.344E-02
4312.380	'P'	2	1	3.5	1	1	0.344E-02
4312.451	'R'	1	2	3.5	0	0	0.387E-02
4312.536	'Q'	1	1	3.5	1	1	0.344E-02
4312.588	'Q'	1	1	3.5	1	1	0.344E-02
4312.598	'Q'	2	2	2.5	0	0	0.387E-02
4312.680	'Q'	2	2	2.5	0	0	0.387E-02
4312.717	'Q'	2	2	1.5	0	0	0.387E-02
4312.767	'Q'	2	2	1.5	0	0	0.387E-02
4312.827	'R'	1	2	2.5	0	0	0.387E-02
4312.862	'P'	2	1	4.5	0	0	0.387E-02
4312.895	'Q'	1	1	4.5	0	0	0.387E-02
4312.909	'R'	1	2	2.5	0	0	0.387E-02
4313.011	'Q'	1	1	2.5	1	1	0.344E-02
4313.013	'Q'	1	1	2.5	1	1	0.344E-02
4313.016	'Q'	1	1	4.5	0	0	0.387E-02
4313.037	'R'	1	2	1.5	0	0	0.387E-02
4313.087	'R'	1	2	1.5	0	0	0.387E-02

Continued on the next page...

A.2 General atomic parameters of the elements involved in the G-Band calculations

Wavelength, Å	Branch	IU	IL	JL	VU	VL	FVV
4313.361	'P'	2	1	3.5	0	0	0.387E-02
4313.420	'P'	2	1	3.5	0	0	0.387E-02
4313.590	'Q'	1	1	3.5	0	0	0.387E-02
4313.649	'Q'	1	1	3.5	0	0	0.387E-02
4313.876	'P'	2	1	2.5	0	0	0.387E-02
4313.037	'R'	1	2	1.5	0	0	0.387E-02
4313.087	'R'	1	2	1.5	0	0	0.387E-02
4313.361	'P'	2	1	3.5	0	0	0.387E-02
4313.420	'P'	2	1	3.5	0	0	0.387E-02
4313.876	'P'	2	1	2.5	0	0	0.387E-02
4313.899	'P'	2	1	2.5	0	0	0.387E-02
4314.196	'Q'	1	1	2.5	0	0	0.387E-02
4314.219	'Q'	1	1	2.5	0	0	0.387E-02
4314.804	'R'	1	1	1.5	2	2	0.281E-02
4314.820	'R'	1	1	1.5	2	2	0.281E-02

A.2 General atomic parameters of the elements involved in the G-Band calculations

Element	Abundance	1st potential	2nd potential	Relative mass
Ti	4.99	6.8200	13.5756	47.90
Ni	6.21	18.16884	58.6934	58.6934
V	3.96	14.66	50.9415	50.9415
Fe	7.50	7.9024	16.1879	55.85
Cr	5.67	6.7667	16.4858	51.9961
Nd	1.46	5.5250	10.73	144.24
Ca	6.36	6.1132	11.8718	40.08
Sc	3.06	6.56144	12.79967	44.9559
Y	2.20	6.217	12.24	88.90585
Mn	5.45	7.4340	15.640	54.938

A.3 Atomic lines of G Band

Wavelength, Å	Atom	$\log(g^*f)$	χ_e	Lower term	Upper term
4295.731	CrI	-0.720	2.708102	(4P)4s a5P	a3P)sp v5P
4295.751	TiI	-0.450	0.812998	(4F)4s a5F	(4F)4p x5D
4295.881	NiI	-0.480	3.841263	(3F)sp z3G	s2F)5s g3F
4296.098	VI	0.410	2.13045	(3G)4s a4G	(3G)4p w4H
4296.572	FeI	-2.810	2.704533	(3P)4s b4P	(5D)4p z4F
4297.031	CrI	-1.030	2.708975	(4P)4s a5P	a3P)sp v5P
4297.496	FeI	-3.107	4.371645	(4F)4p z5G	s4D)4d g5G
4297.675	VI	0.290	2.122377	(3G)4s a4G	(3G)4p w4H
4297.744	CrI	0.250	3.75	(2I)4s a3I	(2I)4p z3K
4297.784	NdII	-0.780	0.380255	(3P)4s b4P	(5D)4p z4D
4298.028	VI	0.240	2.114688	(3G)4s a4G	(3G)4p w4H
4298.037	FeI	-1.370	3.047074	(2G)4s a1G	(3F)sp x3G
4298.201	FeI	-2.302	3.111171	(2P)4s c3P	(3G)sp v5F
4298.507	NiI	-1.388	3.841263	(3F)sp z3G	s2F)5s g3F
4298.664	TiI	-0.050	0.818196	(4F)4s a5F	(4F)4p x5D
4298.988	CaI	-0.412	1.8859	4s4p 3P	4p2 3P
4299.228	TiI	-0.006	1.7490	(4P)4s a5P	(4P)4p y5S
4299.234	FeI	-0.430	2.4256	(5D)sp z7D	s6D)5s e7D
4299.241	FeI	-1.750	3.2673	(2H)4s b3H	(2G)4p y3H
4299.628	FeI	-2.113	3.0178	s2 b3G	(3G)sp w5G
4299.633	TiI	-0.770	0.8259	(4F)4s a5F	(3F)sp w3D
4299.707	CrI	-0.930	2.8997	(6S)4p z7P	4s5s f7D
4300.049	TiII	-0.770	1.1802	d3 a4P	(3F)4p z4D
4300.205	FeI	-1.810	3.8819	(5D)sp z3F	(4F)4d e3H
4300.467	TiI	-0.704	2.1604	2D2)4s a3D	(4P)4p r3D
4300.498	CrI	-0.430	3.4351	s2 b3G	(3G)sp w3F
4300.556	TiI	0.170	0.8259	(4F)4s a5F	(4F)4p x5D
4300.825	FeI	-1.190	3.9844	(5D)sp z3F	(4F)4d f3F
4301.081	TiI	0.260	0.8361	(4F)4s a5F	(4F)4p x5D
4301.177	CrI	-0.190	3.4491	s2 b3G	(3G)sp w3F
4301.914	TiII	-1.160	1.1610	d3 a4P	(3F)4p z4D
4302.087	NiI	-2.321	3.480234	(3F)sp z5G	s4F)5s f3F
4302.185	FeI	-1.740	3.0471	(2G)4s a1G	(3F)sp x3G
4302.528	CaI	0.275	1.8991	4s4p 3P	4p2 3P
4302.692	FeI	-4.446	2.4536	s2 a3H	(3H)sp y5G
4303.049	FeI	-3.683	3.8838	(5D)sp z3D	(4F)4d e3H
4303.176	FeII	-2.490	2.7045	(3P)4s b4P	(5D)4p z4D

Continued on the next page...

Wavelength, Å	Atom	$\log(g^*f)$	χ_e	Upper term	Lower term
4303.571	NdII	0.140	0.000	(3P)4s b4P	(5D)4p z4D
4304.540	FeI	-2.010	2.9490	s2 b3G	(3H)sp z3H
4304.641	FeI	-3.898	4.0761	d8 c3F	(3G)sp 1F
4304.869	FeI	-2.083	3.3016	(2H)4s b3H	(2G)4p v3G
4305.134	FeI	-3.310	2.7277	(2G)4s a3G	(3P)sp 3D
4305.205	FeI	-2.070	3.5468	(2D)4s a1D	(2H)4p u3G
4305.451	FeI	-1.300	3.0175	(2P)4s c3P	(4P)4p y3S
4305.528	FeI	-1.975	4.3128	(4F)4p z5G	s4D)4d g5G
4305.528	FeI	-1.975	4.312761	(4F)4p z5G	s4D)4d g5G
4305.714	ScII	-1.220	0.595520	3d2 3F	3d4p 3D
4305.760	TiI	-1.071	2.236482	(2H)4s a3H	s4F)5p u3G
4305.910	TiI	0.350	0.8485	(4F)4s a5F	(4F)4p x5D
4306.057	FeI	-2.997	3.3967	(5D)sp z5F	s6D)4d e7P
4306.326	TiI	-1.392	3.186603	(3P)sp y5D	d2 4p2 h5D
4306.580	FeI	-2.218	3.4304	(5D)sp z5F	s6D)4d f5D
4306.692	FeI	-2.982	4.4156	(4F)4p z5G	s4D)4d g5G
4307.176	VI	-1.732	0.000	d3s2 a4F	(4F)sp z4F
4307.270	NiI	-1.113	4.153857	(3F)sp y3D	s4F)4d f3P
4307.619	FeI	-4.422	3.2517	(2D)4s a3D	(2G)4p w3F
4307.744	CaI	-0.256	1.8859	4s4p 3P	4p2 3P
4307.863	TiI	-1.290	1.165	d3 a4P	(3F)4p z4D
4307.902	FeI	-0.070	1.5575	(4F)4s a3F	(4F)4p z3G
4308.464	TiI	-1.078	1.0666	s2 a3P	(3P)sp y3P
4308.506	FeI	-3.317	2.4536	s2 a3H	(3H)sp z5I
4308.529	FeI	-4.120	2.2229	(4P)4s a5P	(5D)sp x5F
4309.031	FeI	-1.100	3.6346	s2 a1I	(2H)4p y3I
4309.369	FeI	-1.180	2.9490	s2 b3G	(3H)sp z3H
4309.455	FeI	-1.579	3.111171	(2P)4s c3P	a3P)sp v5P
4309.631	YII	-0.750	0.179765	d5s a3D	s5p z3P
4309.672	FeI	-4.967	2.9982	(5D)sp z7P	(4F)5s e5F
4309.790	FeI	-2.023	4.5847	(2F)4s d3F	(3F)sp r3G
4309.800	VI	-1.580	0.040107	d3s2 a4F	(4F)sp z4F
4310.066	FeI	-3.280	3.4304	(5D)sp z5F	s6D)4d e7P
4310.371	FeI	-1.500	3.9289	(5D)sp z3D	(4F)4d e3P
4310.542	FeI	-2.686	3.6355	s2 b3D	(2P)4p u3D
4310.656	CrI	-1.507	2.967626	s2 a3H	(3H)sp x5G
4311.646	TiI	-0.925	2.153700	2D2)4s a3D	(4P)4p r3D
4312.369	VII	-4.632	1.6728	d4 b3F	(4F)4p z5F
4312.473	CrI	-1.370	3.112999	s2 a3F	(3H)sp y3H
4312.551	MnI	-1.077	2.941044	(5D)4s a4D	(5D)4p y4P
4312.864	TiII	-1.160	1.180169	d3 a4P	(3F)4p z4D

Continued on the next page...

A The G-Band lines table

Wavelength, Å	Atom	$\log(g^*f)$	χ_e	Upper term	Lower term
4313.043	FeI	-3.258	2.758764	(2G)4s a3G	(3H)sp y3G
4313.889	VI	-1.313	1.853611	(3H)4s a4H	(3H)4p x2H
4313.527	NiI	-1.525	4.164930	(3F)sp z1G	s4F)4d i3F
4314.083	ScII	-0.100	0.618449	3d2 3F	3d4p 3D
4314.310	FeII	-3.477	2.675963	(3H)4s a4H	(5D)4p z4F
4314.364	NdII	0.150	1.528995	(3P)4s b4P	(5D)4p z4D
4314.506	NdII	-0.920	0.000	(3P)4s b4P	(5D)4p z4D
4314.730	TiI	-1.633	0.818196	(4F)4s a5F	(3F)sp w3D
4314.804	TiI	-0.416	0.836052	(4F)4s a5F	(3F)sp w3D
4314.975	TiI	-1.130	1.16102	d3 a4P	(3F)4p z4D
4314.979	FeII	-3.103	4.732076	(1D)4s c2D	(3P)4p y4P

Outlook

The results of the radiative diagnostics of the MHD simulations presented in this thesis establish a connection between the physical processes in the uppermost layers of the solar convection zone and photosphere and the observational polarimetric properties of the Sun. The results look very promising and suggest some further research topics, such as:

- Firstly, more detailed comparison of the simulated polarimetric data is necessary to provide in order to get better understanding of the physical processes in the simulated regions of the Sun.
- Radiative diagnostics of the simulations with a large range of average magnetic field strength, including strong magnetic field regimes (sunspot umbra) and initial magnetic field of mixed polarity. This will contribute to understand the dynamics of sunspots and magnetic features in the “quiet” Sun, where the fields of different strength and even opposite polarities may exist on small spatial scales (e.g. Sánchez Almeida et al. (2003)).
- Simulations and radiative diagnostics of the domains with larger horizontal dimensions can be used to study the origin of the mesogranular structure, which appears in simulations of (magneto-)convection.
- Radiative diagnostics of the MHD models with different μ angles can be used to study the center-to-limb variation in various spectral lines and continuum bands and to compare the results of the simulations with observational data.
- The radiative diagnostics in other spectral bands dominated by molecular lines (for example, the CN band at 388.0 nm) can be used to compare with various observational phenomena in these bands.

Bibliography

- Auer, L. H., Heasley, J. N., House, L. L., 1977, Non-LTE line formation in the presence of magnetic fields, *ApJ*, 216, 531
- Basu, S., Antia, H. M., 1997, Seismic measurement of the depth of the solar convection zone, *MNRAS*, 287, 189
- Berdyugina, S. V., Solanki, S. K., 2002, The molecular Zeeman effect and diagnostics of solar and stellar magnetic fields. I. Theoretical spectral patterns in the Zeeman regime, *A&A*, 385, 701
- Berdyugina, S. V., Solanki, S. K., Frutiger, C., 2003, The molecular Zeeman effect and diagnostics of solar and stellar magnetic fields. II. Synthetic Stokes profiles in the Zeeman regime, *A&A*, 412, 513
- Berger, T. E., Title, A. M., 1996, On the Dynamics of Small-Scale Solar Magnetic Elements, *ApJ*, 463, 365
- Berger, T. E., Title, A. M., 2001, On the Relation of G-Band Bright Points to the Photospheric Magnetic Field, *ApJ*, 553, 449
- Berger, T. E., Schrijver, C. J., Shine, R. A., Tarbell, T. D., Title, A. M., Scharmer, G., 1995, New Observations of Subarcsecond Photospheric Bright Points, *ApJ*, 454, 531
- Berger, T. E., Löfdahl, M. G., Shine, R. S., Title, A. M., 1998, Measurements of Solar Magnetic Element Motion from High-Resolution Filtergrams, *ApJ*, 495, 973
- Caunt, S. E., Korpi, M. J., 2001, A 3D MHD model of astrophysical flows: Algorithms, tests and parallelisation, *A&A*, 369, 706
- Collados, M., Vázquez, M., 1987, A new determination of the solar granulation contrast, *A&A*, 180, 223
- Condon, E. U., Shortley, G., 1951, *The Theory of Atomic Spectra*, Cambridge, England: Cambridge University Press, 1951
- De Pontieu, B., 2002, High-Resolution Observations of Small-Scale Emerging Flux in the Photosphere, *ApJ*, 569, 474
- Deinzer, W., Hensler, G., Schüssler, M., Weisshaar, E., 1984, Model calculations of magnetic flux tubes. I - Equations and method. II - Stationary results for solar magnetic elements, *A&A*, 139, 426

- Delbouille, L., Roland, G., Neven, L., 1973, Atlas photometrique DU spectre solaire de $[\lambda] 3000$ a $[\lambda] 10000$, Liege: Universite de Liege, Institut d'Astrophysique, 1973
- Domínguez Cerdeña, I., 2003, Evidence of mesogranulation from magnetograms of the Sun, *A&A*, 412, L65–L68
- Dunn, R. B., Zirker, J. B., 1973, The Solar Filigree, *Sol. Phys.*, 33, 281
- Gadun, A. S., Solanki, S. K., Sheminova, V. A., Ploner, S. R. O., 2001, A formation mechanism of magnetic elements in regions of mixed polarity, *Sol. Phys.*, 203, 1
- Gandorfer, A., 2002, The Second Solar Spectrum, Vol. 2: 3910Å to 4630Å, (Zürich: vdf), ISBN 3 7281 2855 4
- Grossmann-Doerth, U., Schüssler, M., Solanki, S. K., 1988, Unshifted, asymmetric Stokes V-profiles - Possible solution of a riddle, *A&A*, 206, L37
- Grossmann-Doerth, U., Schuessler, M., Solanki, S. K., 1989, Stokes V asymmetry and shift of spectral lines, *A&A*, 221, 338
- Grossmann-Doerth, U., Knölker, M., Schüssler, M., Solanki, S. K., 1994, The deep layers of solar magnetic elements, *A&A*, 285, 648
- Hale, G. E., 1908, On the Probable Existence of a Magnetic Field in Sun-Spots, *ApJ*, 28, 315
- Hammerschlag, R. H., Bettonvil, F. C. M., 1998, The Dutch Open Telescope at the Roque de los Muchachos Observatory, *New Astronomy Review*, 42, 485
- Herschel, W., 1801, Additional Observations Tending to Investigate the Symptoms of the Variable Emission of the Light and Heat of the Sun; With Trials to Set Aside Darkening Glasses, by Transmitting the Solar Rays through Liquids; And a Few Remarks to Remove Objections That Might Be Made against Some of the Arguments Contained in the Former Paper, *Philosophical Transactions Series I*, 91, 354
- Hirzberger, J., Kneer, F., 2000, High Resolution 2D-Spectroscopy of the Sun, *Hvar Observatory Bulletin*, 24, 89
- Illing, R. M. E., Landman, D. A., Mickey, D. L., 1975, Broad-band circular polarization of sunspots - Spectral dependence and theory, *A&A*, 41, 183
- Irwin, A. W., 1981, Polynomial partition function approximations of 344 atomic and molecular species, *ApJS*, 45, 621
- Kneer, F., Stolpe, F., 1996, High Resolution Observations of Small-Scale Magnetic Elements and Interpretation, *Sol. Phys.*, 164, 303
- Kneer, F., Hasan, S. S., Kalkofen, W., 1996, Spectral line radiation from solar small-scale magnetic flux tubes., *A&A*, 305, 660

- Knölker, M., Grossmann-Doerth, U., Schüssler, M., Weisshaar, E., 1991, Some developments in the theory of magnetic flux concentrations in the solar atmosphere, *Advances in Space Research*, 11, 285
- Koschinsky, M., Kneer, F., Hirzberger, J., 2001, Speckle spectro-polarimetry of solar magnetic structures, *A&A*, 365, 588
- Kunasz, P., Auer, L. H., 1988, Short characteristic integration of radiative transfer problems - Formal solution in two-dimensional slabs, *Journal of Quantitative Spectroscopy and Radiative Transfer*, 39, 67
- Landau, L., Lifshits, E., 1989, *Quantum Mechanics (Non-relativistic theory)*, Moscow Izdatelstvo Nauka Teoreticheskaja Fizika
- Landi Degl'Innocenti, E., 2003, The Zeeman effect: applications to solar physics, *Astronomische Nachrichten*, 324, 393
- Langhans, K., Schmidt, W., Tritschler, A., 2002, 2D-spectroscopic observations of G-band bright structures in the solar photosphere, *A&A*, 394, 1069
- Ludwig, H., 1992, Nichtgrauer Strahlungstransport in numerischen Simulationen stellarer Konvektion, "Ph.D. Thesis"
- Messiah, A., 1962, *Quantum mechanics*, Amsterdam: North-Holland Publication, 1961-1962
- Mihalas, D., 1978, *Stellar atmospheres /2nd edition/*, San Francisco, W. H. Freeman and Co., 1978. 650 p.
- Muller, R., 1985, The fine structure of the quiet sun, *Sol. Phys.*, 100, 237
- Muller, R., Roudier, T., 1984, Variability of the quiet photospheric network, *Sol. Phys.*, 94, 33
- Nesis, A., Hammer, R., Hanslmeier, A., Schleicher, H., Sigwarth, M., Staiger, J., 1996, Dynamics of the solar granulation. V. The intergranular space., *A&A*, 310, 973
- Nordlund, A., 1984, A Re-evaluation of the Granular Δ Irms, in *Small-Scale Dynamical Processes in Quiet Stellar Atmospheres*, p. 174
- Rast, M. P., Nordlund, A., Stein, R. F., Toomre, J., 1993, Ionization effects in three-dimensional solar granulation simulations, *ApJ*, 408, L53
- Rees, D. E., Durrant, C. J., Murphy, G. A., 1989, Stokes profile analysis and vector magnetic fields. II - Formal numerical solutions of the Stokes transfer equations, *ApJ*, 339, 1093
- Roberts, B., Webb, A. R., 1978, Vertical motions in an intense magnetic flux tube, *Sol. Phys.*, 56, 5
- Rüedi, I., Solanki, S. K., Rabin, D., 1992, Infrared lines as probes of solar magnetic features. IV - Discovery of a siphon flow, *A&A*, 261, L21

- Rutten, R. J., Hammerschlag, R. H., Sütterlin, P., Bettonvil, F. C. M., 2001, Proxy Magnetometry with the Dutch Open Telescope, in ASP Conf. Ser. 236: Advanced Solar Polarimetry – Theory, Observation, and Instrumentation, p. 25
- Sánchez Almeida, J., Asensio Ramos, A., Trujillo Bueno, J., Cernicharo, J., 2001, G-Band Spectral Synthesis in Solar Magnetic Concentrations, *ApJ*, 555, 978
- Sánchez Almeida, J., Domínguez Cerdeña, I., Kneer, F., 2003, Simultaneous Visible and Infrared Spectropolarimetry of a Solar Internetwork Region, *ApJ*, 597, L177
- Schadee, A., 1964, The formation of molecular lines in the solar spectrum, *Bulletin of the Astronomical institute of the Netherlands*, 17, 311
- Schmidt, W., Beck, C., Kentischer, T., Elmore, D., Lites, B., 2003, POLIS: A spectropolarimeter for the VTT and for GREGOR, *Astronomische Nachrichten*, 324, 300
- Shchukina, N., Trujillo Bueno, J., 2001, The Iron Line Formation Problem in Three-dimensional Hydrodynamic Models of Solar-like Photospheres, *ApJ*, 550, 970
- Sheeley, N. R., 1967, Observations of Small-Scale Solar Magnetic Fields, *Sol. Phys.*, 1, 171
- Sheeley, N. R., 1971, Using CN λ 3883 Spectroheliograms to Map Weak Photospheric Magnetic Fields, *Sol. Phys.*, 20, 19
- Shelyag, S., Solanki, S., Vögler, A., Schüssler, M., 2004, G-Band spectral synthesis and diagnostics of simulated solar magneto-convection, *A&A*
- Sheminova, V. A., 2003, The line Fe I λ 1564.8 nm and distribution of solar magnetic fields, *Kinematika i Fizika Nebesnykh Tel*, 19, 107
- Shimizu, T., 2002, Solar-B, *Advances in Space Research*, 29, 2009
- Solanki, S. K., 1987, The Photospheric Layers of Solar Magnetic Flux Tubes, Ph.D. Thesis
- Solanki, S. K., 1989, The origin and the diagnostic capabilities of the Stokes V asymmetry observed in solar faculae and the network, *A&A*, 224, 225
- Solanki, S. K., 1993, Smallscale Solar Magnetic Fields - an Overview, *Space Science Reviews*, 63, 1
- Solanki, S. K., Pahlke, K. D., 1988, Can stationary velocity fields explain the Stokes V asymmetry observed in solar magnetic elements?, *A&A*, 201, 143
- Solanki, S. K., Ruedi, I. K., Livingston, W., 1992, Infrared lines as probes of solar magnetic features. II - Diagnostic capabilities of Fe I λ 15648.5 Å and λ 15652.9 Å, *A&A*, 263, 312
- Solanki, S. K., Ruedi, I., Bianda, M., Steffen, M., 1996, On the detection of shocks in the solar granulation., *A&A*, 308, 623

- Solanki, S. K., Schüssler, M., Curdt, W., Lites, B. W., Martinez Pillet, V., Schmidt, W., Title, A. M., Sunrise Team, 2002, Sunrise: a 1-m balloon borne solar telescope, in ESA SP-505: SOLMAG 2002. Proceedings of the Magnetic Coupling of the Solar Atmosphere Euroconference, p. 27
- Solanki, S. K., Gandorfer, A. M., Schuessler, M., Curdt, W., Lites, B. W., Martinez-Pillet, V., Schmidt, W., Title, A. M., 2003, SUNRISE: a balloon-borne telescope for high resolution solar observations in the visible and UV, in Innovative Telescopes and Instrumentation for Solar Astrophysics. Edited by Stephen L. Keil, Sergey V. Avakyan . Proceedings of the SPIE, Volume 4853, pp. 129-139 (2003)., p. 129
- Spruit, H. C., 1976, Pressure equilibrium and energy balance of small photospheric flux-tubes, *Sol. Phys.*, 50, 269
- Spruit, H. C., 1977, Magnetic flux tubes and transport of heat in the convection zone of the Sun., Ph.D. Thesis
- Spruit, H. C., Roberts, B., 1983, Magnetic flux tubes on the sun, *Nature*, 304, 401
- Stein, R. F., Bercik, D., Nordlund, A., 2002, Solar convection and magneto-convection simulations, "Nuovo Cimento C Geophysics Space Physics C", 25, 513
- Steiner, O., Grossmann-Doerth, U., Knölker, M., Schüssler, M., 1998, Dynamical Interaction of Solar Magnetic Elements and Granular Convection: Results of a Numerical Simulation, *ApJ*, 495, 468
- Stenflo, J. O., 1973, Magnetic-Field Structure of the Photospheric Network, *Sol. Phys.*, 32, 41
- Stenflo, J. O., 1994, Solar magnetic fields: polarized radiation diagnostics, *Astrophysics and Space Science Library*, Dordrecht; Boston: Kluwer Academic Publishers, —c1994
- Stix, M., 2002, The sun: an introduction, *The sun : an introduction – 2nd ed.* /Michael Stix. Berlin : Springer, 2002. QB 521 .S75
- Tomczyk, S., Elmore, D. F., Lites, B. W., Dunn, R. B., Skumanich, A., Schuenke, J. A., Streander, K. V., Leach, T. W., Chambellan, C. W., Lacey, L. B., 1992, The Advanced Stokes Polarimeter: A New Instrument for Solar Magnetic Field Research, *Bulletin of the American Astronomical Society*, 24, 814
- Uitenbroek, H., Miller-Ricci, E., Ramos, A. A., Trujillo Bueno, J., 2004, The Zeeman effect in the g band., *ApJ*, 604, 960
- Unno, W., 1956, Line Formation of a Normal Zeeman Triplet, *PASJ*, 8, 108
- Vögler, A., Schüssler, M., 2003, Studying magneto-convection by numerical simulation, *Astronomische Nachrichten*, 324, 399
- van Ballegooijen, A. A., Nisenson, P., Noyes, R. W., Löfdahl, M. G., Stein, R. F., Nordlund, Å., Krishnakumar, V., 1998, Dynamics of Magnetic Flux Elements in the Solar Photosphere, *ApJ*, 509, 435

- Vögler, A., 2003, Three-dimensional simulations of magneto-convection in the solar photosphere, Ph.D. Thesis
- Vögler, A., Shelyag, S., Schüssler, M., Cattaneo, F., Emonet, T., Linde, T., 2003, IAU Symposium, eds. Piskunov, N.E., Weiss, W.W., Gray, D.F.
- Weiss, N. O., 1966, The expulsion of Magnetic Flux by Eddies., "Royal Society of London Proceedings Series A", 293, 310
- Wiehr, E., 1978, A Unique Magnetic Field Range for Nonspot Solar Magnetic Regions, *A&A*, 69, 279
- Zeeman, P., 1897, On the Influence of Magnetism on the Nature of the Light Emitted by a Substance., *ApJ*, 5, 332

Acknowledgements

The presented PhD thesis has been written in the Max Planck Institute for Aeronomy, Katlen-berg-Lindau. I thank the directors of the institute for offering me the possibility to study and work in the nice and creative environment of the institute. Financial support of the Max Planck Society is gratefully acknowledged.

Special thanks to my supervisors, Prof. M. Schüssler and Prof. S. K. Solanki, for offering me the topic which I have been working on, for their kind help and discussions during my PhD project. I thank my university supervisor, Prof. F. Kneer, for the possibility to defend my thesis at the University of Göttingen, for the seminars in the University Observatory and for helpful discussions. Thank you, my doctorfathers, for the beautiful science which you have introduced to me.

I would like to thank Dr. D. Schmitt, the coordinator of the International Max Planck Research School on Physical Processes in the Solar System and Beyond, for the organization of the school, a member of which I am, for taking care of us, students in Lindau, for the unbending wish to make all of the things even better than they are and for support during the preparation of my thesis.

I would like to thank all our Solar MHD group members (Prof. M. Schüssler, Dr. D. Schmitt, Dr. A. Vögler, Dr. R. Cameron, I. Baumann, M. Cheung, F. Kolesnikov, L. Matloch, M. Schrunner) for the time together, our weekly TGIF meetings and interesting and exciting discussions on physical and mathematical problems and puzzles.

I thank Dr. Alexander Vögler for the MuRAM MHD model snapshots which were kindly provided by him, for answering my questions concerning the model and for his sense of humour.

I am very thankful to the ukrainian-russian-belorussian group of the institute for being with me, for late night coffee, for creative and interesting discussions on just everything.

I thank the international company of all of the students of the Research School in Lindau for the time we spent together inside and outside the institute.

I thank Алёнушка for the sudden and nice appearance in my world and for being together with me independently of the distance between us.

Finally, I gratefully thank my parents for holding my hand with love and patience and for that special kind of physical curiosity, which they gave to me and which forces me to ask the questions “Why?” and “How?” and to search for the answers.

Lebenslauf

Name: Sergiy Shelyag

Geburt: am 27. 02. 1979 in Karachevka, die Ukraine

Eltern: Ivan Shelyag
Valentina Shelyag

Staatsbürgerschaft: ukrainisch

Schulbildung: 9/1985–6/1993 Grundschule (Karachevka)
9/1993–6/1995 Gymnasium N5 (Kharkiv)

Studium: 9/1995–7/2000 Physikstudium an der Radiophysikalischen Fakultät der Nationalen Universität Kharkiv, Abteilung für Weltraumphysik und Radioastronomie

9/1998–1/1999 Bachelorarbeit: “Gamma-ray bursts and the theory of strong explosions”

9/1999–7/2000 Diplomarbeit: “Evolution of clusters of galaxies in the merging model”

6/2000–7/2001 Wissenschaftlicher Mitarbeiter des Instituts für Radioastronomie der Nationalen Akademie der Wissenschaften der Ukraine, Kharkiv

8/2001–7/2004 Doktorarbeit an der Max-Planck-Institut für Aeronomie, Katlenburg-Lindau, und der Universitäts-Sternwarte, Göttingen